The Krypton String Test Cryostat: Characterizing Surface Charge-Induced Dead Layers on High Purity Germanium Detectors

Christian John Nave

A dissertation
submitted in partial fulfillment of the
requirements for the degree of

Doctor of Philosophy

University of Washington

2026

Reading Committee:

Jason Detwiler, Chair

Alejandro Garcia

Marilena Loverde

Program Authorized to Offer Degree:
Physics

University of Washington

Abstract

The Krypton String Test Cryostat: Characterizing Surface Charge-Induced Dead Layers on High Purity Germanium Detectors

Christian John Nave

Chair of the Supervisory Committee:
Jason Detwiler
Department of Physics

The LEGEND experiment is searching for neutrinoless double beta decay, a proposed nuclear decay that, if detected, can help explain some of the most fundamental questions in physics. LEGEND is using germanium detectors, enriched in the double beta-decaying isotope ^{76}Ge to search for this rare process. Background reduction is crucially important to rare event searches like LEGEND and understanding these germanium detectors is a necessary guard against misunderstood backgrounds. This work describes the findings of a germanium test-stand, the Krypton String Test Cryostat (KrSTC). KrSTC uses low energy (< 40 keV) photons and electrons to probe the passivated surface of these detectors. Analysis of the KrSTC data shows different low energy spectra depending on detector and cryostat conditions and suggests a dead layer model investigated through simulation work. This dead layer model, accounting for surface charge collecting on the passivated surface, can be a useful tool in understanding LEGEND backgrounds in the search for neutrinoless double beta decay.

Table of Contents

List of Figures

Figure Number Page

Acronyms/Shorthands

$2\nu\beta\beta$: two neutrino double beta decay

$0\nu\beta\beta$: neutrinoless double beta decay

A/E ($AVSE$): current/energy (current vs. energy)

ADC: analog to digital converter (also used in place of ADU, analog to digital units)

CAGE: Collimated Alphas, Gammas, and Electrons

CENPA: Center for Experimental Nuclear Physics and Astrophysics

CL: confidence level

DAQ: data acquisition

DCR: delayed charge recovery

DL: dead layer

DSP: digital signal processing

ELEPHANT EAR: surface charge-induced dead layer

GERDA: The GERmanium Detector Array

HPGE: High Purity Germanium (detectors)

HV: high voltage

INL: integrated non-linearity

KR: krypton (specifically $^{83\mathrm{m}}$Kr)

KRSTC: Krypton String Test Cryostat

LAR: liquid argon

LEGEND: Large Enriched Germanium Experiment for Neutrinoless Double Beta Decay

L200: LEGEND-200

L1000: LEGEND-1000

LNGS: Laboratori Nazionale del Gran Sasso

MJD: MAJORANA DEMONSTRATOR

NERSC: National Energy Research Scientific Computing Center

NME: nuclear matrix element

ORCA: Object-oriented Real-time Control and Acquisition

PAC: pressure at cooldown

PNNL: Pacific Northwest National Laboratory

PPC: *p*+ point contact (detectors)

PS: passivated surface

PSD: pulse shape discrimination

PZ: pole zero

SIPM: Silicon Photomultipliers

SN: supernova

$Q_{\beta\beta}$: Q-value of $0\nu\beta\beta$

T/E: triangle filter maximum/energy (like A/E)

UW: University of Washington

Acknowledgments

Oh brother. There really are too many people to acknowledge here that had a major part in this work and in my life the past 5+ years, but I'll still give it a whirl.

First, I'd like to thank my reading committee members—Jason Detwiler, Alejandro Garcia, and Marilena Loverde—and my other defense committee members: Eric Bellm and Steve Sharpe. They took time out of their very busy schedules to give me usuful feedback and assistance and I am thankful for that.

CENPA has been a truly amazing place to work these last few years. I sometimes feel guilty with how much fun I've had at this place. Thanks to Dave Hertzog for his leadership throughout my time at CENPA. It has been a tough year full of funding nonsense but it is comforting to know that the director of the lab cares so much about the people who make CENPA work. Thanks to all the CENPA faculty for always being willing to help with a physics problem or to chat about whatever else. The engineers at CENPA were an invaluable help to me during my time and my experiment certainly wouldn't have worked without them. Special thanks to Tim, David, and Nate for always treating my ignorance with kindness. To everyone else that's worked with me at CENPA, from the research scientists to the staff, to the postdocs and grad students and undergrads and anyone else, thank you for making CENPA such a special place.

I've been so lucky to work with so many amazing people in the LEGEND group over the years. To Clint, thank you for teaching me so so much when I first joined the group. You were incredibly patient, helpful, and a massive reason why I am where I am today. Getting to work with you early on opened my eyes to the fact that I might actually work with some really cool people in grad school. East St. Louis Toodle-oo is still a terrible Steely Dan song. To Louis, I am always amazed at your dedication and your competence in this job. You taught me more than I can express and were always happy to do it, or at least pretended really well that you were. I hope to have a fraction of your passion and aptitude for science. To Walter and Nafis, thank you both for your hard work on KrSTC. This project became a beast and I appreciate everything that you put into it. To all the postdocs, grad students, undergrads, and Claudios that worked in the LEGEND group while I was here, thanks for making this group so much fun, so interesting, and so welcoming to me. I'm so grateful to have worked with so many people that I genuinely liked. A special shout-out to Sam and Grace who were incredible friends to me and made work an absolute joy. I loved every second of you two making me scream from laughter at lunch. The people trying to work during that were probably less into it but they can grow up.

To my Philly friends, I have missed you all dearly. It's tough moving away from so many people you love, especially in the middle of a pandemic. But I never felt far from you all. You were my rock and every second we spent together whenever I visited home, during fantasy drafts, playing Madden, talking on Discord, screaming at each other because some moron doesn't think Us and Them by Pink Floyd is that good, every second was a blessing. And we won a Super Bowl together.

To my Seattle friends, I was terrified to move out here. Pretty immediately I was relieved when so many of my classmates were cool. I've built some really great friendships here and I'm so lucky to know so many funny, intelligent, and kind people. Climbing, trivia, game nights, rage cage twice, ping pong, open mics, I have so many amazing memories of my 5+ years here and will always remember these years fondly. I don't know how the coming years could get much better. You can only live in the Neighborhood of the Year 1986 for so long.

To my family, there have been times over these years where it's been really tough being so far away from you all. But I felt your love and support the whole way which got me through the tough times and made the great times that much better. Weddings, nieces and nephews, and two fantasy championships in the last three years have been a real treat. I wouldn't want to go through it with any other people.

Lastly, to Jason, there's no one I give more credit to for this thesis and for how much I've loved these last few years than you. You have cultivated an incredible culture for the LEGEND group. You are an amazingly smart person who always has the answer to a question. But more importantly, you were always willing to help me with whatever that question was, physics or otherwise. Your schedule constantly looked like a Rothko painting on steroids with not a single minute free, yet you were always making time to help with some coding question or to take the group out for drinks after work or to occasionally lose to me in ping pong. You have been so thoughtful and kind and understanding and I am beyond grateful to have worked with such a great person, let alone a great boss.

Thank you all for everything. I can never truly express my gratitude. Ok bye!!!

Dedication

To Fiona Catherine

"They say I got brains..."

— Brian Wilson

Chapter 1

Introduction

It is human nature to wonder about our origins in the universe. Simultaneously much and little is understood about how everything around us came to be. Physics provides much insight as to some of these great mysteries. One of the triumphs of physics has been the Big Bang Theory, a model of the initial expansion and forming of the universe we seek to understand today. However, this theory is not without its blind spots. One critical outstanding question of particle physics is: why do we exist? This is an admittedly glib way to discuss the matter-antimatter asymmetry in the universe. We live in a matter-dominated universe—a material world, so to speak. However, there is no agreement that there should be an excess of matter generated by the Big Bang that persists through the early universe. Neutrinos may be the key to unlocking this mystery.

Neutrinos are the least-well understood particles in our framework of particle physics, the Standard Model. They have masses that appear too small to make sense (and too small to measure) and they may be their own antiparticles. If the latter is true, there are theoretical motivations that explain the former and may help us solve this matter-antimatter asymmetry problem. A neutral right-handed singlet, with no charge of any kind in the Standard Model, could decay in the early universe and create more matter than antimatter, later "freezing in" this asymmetry. The addition of a so-called heavy right handed neutrino like this to the Standard Model would solve a multitude of problems with our current theoretical models of particle physics.

Neutrinos are notoriously difficult to study due to their charge neutrality and tiny mass. Determining whether neutrinos and their antiparticles are equivalent is certainly a challenge. However, there may exist a process known as neutrinoless double beta decay. If this decay is discovered, it would be the first example of a process violating the conservation of lepton number (and thus, lepton minus baryon number), conservation laws that appear in the Standard Model but are not required in the construction of the theory. It would also tell us that neutrinos are Majorana particles; that is to say simply, they are their own antiparticle. If this decay does occur, it occurs very rarely and requires a significant experimental program to discover.

This chapter discusses the history of our understanding (and lack of understanding) of neutrinos. Following this is an overview of one of the most important aspects of the neutrino, its mass, and how different prescriptions of the neutrino mass can lead towards a deeper understanding of many outstanding questions in physics. We then close with the relevant background information on neutrinoless double beta decay itself and how we can one day hope to detect it.

1.1 The History of the Neutrino

A quick outline of major discoveries in the history of particle and neutrino physics is a useful way to provide context for the rest of this thesis. We can start our story before the turn of the 20th century with J.J. Thomson and his discovery of the electron [1]. He found negatively charged particles over 1000 times lighter than the hydrogen atom. In 1911, Ernest Rutherford corrected Thomson's model of the nucleus and prescribed the atom a heavy nucleus through his famous gold foil experiment [2]. Rutherford was also instrumental in the discovery of radioactivity [3], along with Henri Becquerel [4], Pierre and Marie Curie [5], and Paul Villard [6]—among others—around the turn of the century. The three channels of radioactive decay discovered were:

- α-decay: emission of an α particle (helium nucleus) by an atomic nucleus
- β-decay: emission of a β particle (electron or positron) by an atomic nucleus
- γ-decay: emission of a γ particle (photon) by an atomic nucleus

There was an interesting difference between β-decay and other radioactivity. While α and γ-decays emitted a single particle with some characteristic energy, James Chadwick confirmed that β-decay produced a continuous energy spectrum in 1914 [7]. This hinted at the fact that there was another particle involved in this process. If β-decay was a simple two-body decay, the β particle should carry away all of the energy difference between the initial and final nuclear state in order to conserve energy. Along came Pauli who proposed that a light neutral particle was emitted along with the β particle that carried away the "missing" energy in the decay [8].

This proposal turned out to be fruitful. Enrico Fermi developed a theory of β-decay in 1933 [9] which laid much of the groundwork for the subsequent development of modern quantum field theory. Fermi explained Pauli's "neutrino" was a valid candidate to solve the β-decay issue, provided it was light, neutral, and extremely light. This led to processes such as neutron decay, described as: $n \to p + e^{-} + \overline{\nu}_e$. Additionally, other processes were allowed, such as inverse β-decay ($\overline{\nu}_e + p \to n + e^{+}$ and $\nu_e + n \to p + e^{-}$). Inverse beta decay was the process by which Cowen and Reines first detected neutrinos in 1956 [10]. Electron antineutrinos from a nuclear reactor interacted in water tanks with the protons in the hydrogen nuclei, producing neutrons and positrons. Positron annihilation produced prompt gamma rays whereas the neutrons captured on cadmium nuclei yielding delayed gammas, all of which were detected with liquid scintillator.

A number of experiments studying the nature of neutrinos followed. The Wu experiment, conducted by Chien-Shiung Wu in 1956, determined that parity was violated by weak interactions [11]. Doctor Wu[1] carried out this experiment utilizing ^{60}Co in a uniform magnetic field. This isotope of cobalt decays via β-decay to an excited nuclear state of ^{60}Ni which promptly emits two γ-rays. It was found that these polarized Co atoms preferentially emit the resulting β^{-} particle in a direction opposite to that of the nuclear spin, thus confirming the violation of parity by the weak interaction. This result was immediately confirmed by a group including Leon Lederman—their paper was published adjacent to Wu's work in the same physics journal [12].

Goldhaber, Grodzins, and Sunyar performed a beautiful experiment in 1957 to determine the helicity of the neutrino [13]. Helicity is the projection of the spin of a particle onto the direction of the particle's momentum and can be positive ("right-handed") or negative ("left-handed"). Goldhaber *et al.* took advantage of electron captures on ^{152m}Eu nuclei. This electron capture processes produces an electron neutrino and an excited nuclear state of ^{152}Sm which then emits a gamma to relax to its ground state (it can also undergo a two-level decay, but that is not considered here). ^{152m}Eu has angular momentum $J = 0$ as does ^{152}Sm, but ^{152}Sm*, the excited nuclear state, has $J = 1$. Due to conservation laws, the neutrino and recoiling ^{152}Sm* have opposing momentum

---

[1] Katy Lied (1975)

vectors but we don't a priori know the directions of the spins. This $^{152}\mathrm{Sm}^*$ nucleus recoils and its recoil energy is slightly Doppler broadened. The de-excitation of this nucleus has a life-time of $\sim$ 30 fs so the nucleus does not have enough time to "get rid" of this recoil energy. Then, when the gamma is emitted, it contains some of the helicity information of the nucleus (and thus, the neutrino). There is an alternating magnetic field that selects photons of some polarization, which then enter a resonant scatterer of ground-state $^{152}\mathrm{Sm}$ nuclei. Only the forward-emitted gammas from that nuclear de-excitation can excite the ground-state nuclei due to Doppler shifting. Some number of these ground state nuclei will be excited and emit photons which are detected by a NaI crystal. When all is said and done, the result of the experiment is an asymmetry between the different polarizations of the photons incident on the resonant scatterer. The value of this asymmetry tells us that neutrinos have negative (left-handed) helicity. A similar experiment was run in 1970 by Palathingal which found only right-handed antineutrinos [14].

Given these experimental results, Marshak and Sudarshan came up with the $V - A$ structure of the weak interaction [15] (in parallel with Feynman and Gell-Mann [16]). This vector minus axial-vector structure can be seen in Equation (1.1) where the current looks like:

$$j^\mu \propto \overline{\psi} \left(\gamma^\mu - \gamma^\mu \gamma^5\right) \phi \tag{1.1}$$

This forces parity to be maximally violating in the weak interaction, the only fundamental force to show this behavior. The weak interaction only interacts with left-handed particles (and right-handed antiparticles). Based on experiment we only see left-handed neutrinos and right-handed antineutrinos. So it was thought for a long time that there was no need for right-handed neutrinos in the Standard Model. Neutrinos were considered to be massless, since in that case their helicity and chirality would be equivalent and you would only ever have left-handed neutrinos and right-handed antineutrinos. Note that right-handed neutrinos are not forbidden in the Standard Model, as they can exist as a singlet state in the $\mathrm{SU}(3)\times\mathrm{SU}(2)_\mathrm{L}\times\mathrm{U}(1)$ gauge group.

Another important discovery was that of the muon neutrino in 1962 by Lederman, Schwartz, and Steinberger [17]. There was to be some way to explain that there was no muon decay of the form $\mu \rightarrow e + \gamma$. An explanation was that there was some sort of "muon-number" conservation law, but this did not explain the existence of decays like $\mu \rightarrow e + \nu + \overline{\nu}$. A work-around was to theorize that there were in fact two neutrinos, the electron neutrino and the muon neutrino, and that “electron number” minus “muon number” was a conserved quantity. The Lederman group at Brookhaven National Lab used their accelerator to generate large numbers of pions. These pions would decay, yielding muons and neutrinos. The pions and muons were stopped in steel but the neutrinos punched right through. Those neutrinos interacted (very rarely) with protons in aluminum nuclei in the 10 ton spark chamber to produce charged particles which resulted in discharges in the spark chamber. Most of these non-background charged particles passed right through the rest of the aluminum, suggesting they were muons and that the neutrinos that create them had some “muon-ness” to them. The DONUT collaboration discovered the third neutrino flavor, the tau neutrino, in 2000 [18].

A crucial experiment was headed by Raymond Davis and John Bahcall at the Homestake Gold Mine in Lead, South Dakota [19] [20]. This experiment, which ran for over twenty years, provided the first detection of neutrinos created in the sun via nuclear fusion reactions. The Homestake experiment used solar electron neutrino captures on ^{37}Cl nuclei to yield ^{37}Ar nuclei which were subsequently counted. Davis sought to match Bahcall’s calculations but found about $\frac{1}{3}$ of the expected argon. This lead to a number of other experiments to study this discrepancy, penned the “solar neutrino problem.”

One possible explanation for Davis’s findings, with the assumption that the experiment was performed correctly, was that the neutrinos were somehow changing flavors (e, μ, and τ, corresponding to the heavier leptons) as they propagated from the sun to the detector. Bruno Pontecorvo postulated neutrino flavor oscillations in the late 1950s—this theory also suggested that neutrinos were not massless as originally thought [21] [22]. His theory was later parametrized in the form of the PMNS (Pontecorvo-Maki-Nakagawa-Sakata) matrix, introduced in 1962 [23]. In this theory, there are both flavor and mass eigenstates such that flavor eigenstates can be written as a superposition of mass eigenstates (and vice versa). The PMNS matrix relates the flavor and mass eigenstates.

Experiments such as Kamiokande in Japan and the Irvine-Michigan-Brookhaven detector (IMB) in the United States proved important in studying this neutrino oscillation theory. In 1987, both detectors found, for the first and only time in history, neutrinos emitted from a core collapse supernova, dubbed SN1987A [24] [25] [26]. There was a timing difference in the detection of these individual neutrinos which furthered the massive neutrino idea but only about ten neutrinos were detected so these low statistics would not allow for conclusions to be drawn. It wasn't until 1998 that Super-Kamiokande showed evidence of atmospheric neutrino oscillation [27]. In 2001 the Sudbury Neutrino Observatory (SNO) published its evidence that confirmed solar neutrino oscillations [28] [29]. Other experiments found more proof of oscillations—like KamLAND with reactor neutrinos [30] [31] [32]—meaning the Standard Model of particle physics is not a complete description, particularly for neutrinos. The most crucial difference between the Standard Model and our current understanding of neutrinos is the nonzero neutrino mass.

1.2 Neutrino Mass

The aforementioned PMNS matrix parameterizes the relationship between neutrino mass eigenstates and flavor eigenstates in an equation that can be written as follows:

$$\begin{pmatrix} \nu_e \\ \nu_\mu \\ \nu_\tau \end{pmatrix} = \begin{pmatrix} U_{e1} & U_{e2} & U_{e3} \\ U_{\mu 1} & U_{\mu 2} & U_{\mu 3} \\ U_{\tau 1} & U_{\tau 2} & U_{\tau 3} \end{pmatrix} \begin{pmatrix} \nu_1 \\ \nu_2 \\ \nu_3 \end{pmatrix} \tag{1.2}$$

We can similarly invert the unitary PMNS matrix and rewrite the mass eigenstates as a superposition of flavor eigenstates if we so desire. In the simplified case of 2-state neutrino mixing, the above equation becomes

$$\begin{pmatrix} \nu_e \\ \nu_\mu \end{pmatrix} = \begin{pmatrix} \cos\theta & \sin\theta \\ -\sin\theta & \cos\theta \end{pmatrix} \begin{pmatrix} \nu_1 \\ \nu_2 \end{pmatrix} \tag{1.3}$$

where we have a straightforward 2-dimensional rotation matrix. In 3-state mixing, the parameterization becomes more complex. Our PMNS matrix $\mathcal{U}_{\text{PMNS}}$ in this case is

$$\mathcal{U}_{\text{PMNS}} = \begin{pmatrix} c_{12}c_{13} & s_{12}c_{13} & s_{13}e^{-i\delta} \\ -s_{12}c_{23} - c_{12}s_{23}s_{13}e^{i\delta} & c_{12}c_{23} - s_{12}s_{23}s_{13}e^{i\delta} & s_{23}c_{13} \\ s_{12}s_{23} - c_{12}c_{23}s_{13}e^{i\delta} & -c_{12}s_{23} - s_{12}c_{23}s_{13}e^{i\delta} & c_{23}c_{13} \end{pmatrix} \begin{pmatrix} e^{i\alpha_1/2} & 0 & 0 \\ 0 & e^{i\alpha_2/2} & 0 \\ 0 & 0 & 1 \end{pmatrix} \tag{1.4}$$

where the standard four free parameters are θ_{ij} (mixing angles for which s_{ij} and $c_{ij} \equiv \sin\theta_{ij}$ and $\cos\theta_{ij}$ respectively, for $i \neq j = (1, 2, 3)$) and δ which is nonzero if neutrino oscillations violates

CP symmetry, still an open question. The phase factors α_1 and α_2 are only meaningful if we have Majorana neutrinos—more on that soon. The current best estimates of these parameters from neutrino oscillation experiments are shown in Table 1.1.

	Normal Ordering (NO)	Inverted Ordering (IO)
$\sin^2\theta_{12}$	0.307 ± 0.012	0.307 ± 0.012
$\sin^2\theta_{23}$	$0.534^{+0.015}_{-0.019}$	0.537 ± 0.020
$\sin^2\theta_{13}$	$(2.16 \pm 0.06) \times 10^{-2}$	$(2.16 \pm 0.06) \times 10^{-2}$
δ_{CP}/π rad	$1.21^{+0.19}_{-0.22}$	$1.21^{+0.19}_{-0.22}$
$\frac{\Delta m^2_{21}}{10^{-5}\text{eV}^2}$	7.50 ± 0.19	7.50 ± 0.19
$\frac{\Delta m^2_{32}}{10^{-3}\text{eV}^2}$	2.451 ± 0.026	-2.527 ± 0.034

Table 1.1: Current estimates of 3ν oscillation parameters taken from global analysis of experimental data. Parameters shown for normal ordering ($\Delta m^2_{32} > 0$) and for inverted ordering ($\Delta m^2_{32} < 0$). From the Particle Data Group [33]

We see two Δm^2_{ij} parameters in Table 1.1. These parameters represent the mass differences between the neutrino mass eigenstates ($\Delta m^2_{ij} = m^2_i - m^2_j$). The sign for Δm^2_{32} is noticeably different between the so-called "Normal Ordering" and "Inverted Ordering" columns. These two columns refer to the fact that it is not yet known whether m_3 is larger than or smaller than m_2. Normal ordering (NO) is the scheme in which $m_1 \leq m_2 \leq m_3$ and inverted ordering proposes $m_3 \leq m_1 \leq m_2$. These two schemes are depicted in Figure 1.1. Neither scheme has been meaningfully favored by experimental results but the picture will hopefully become clearer with next-generation experiments investigating more parameter space.

How do these neutrinos actually acquire this mass? If we assume that this process is the same as in the case of leptons and quarks, the neutrino should interact with the Higgs field to acquire its mass. The Lagrangian describing this interaction is

$$\mathcal{L} = \frac{1}{2}\left[i\overline{\psi}\partial\!\!\!/_\mu\psi - i(\partial\!\!\!/_\mu\overline{\psi})\psi\right] - m\overline{\psi}\psi \tag{1.5}$$

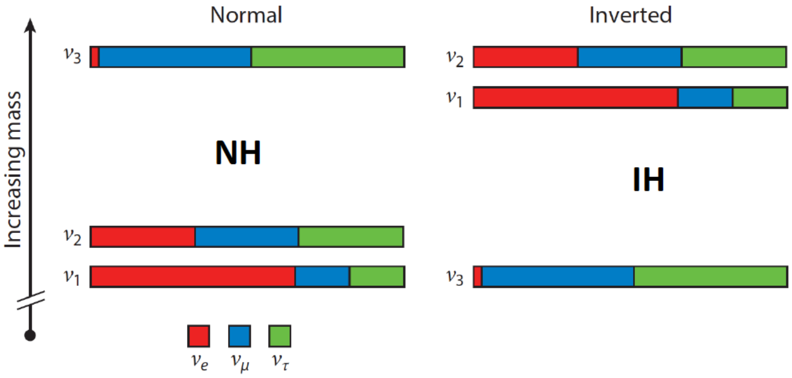

Figure 1.1: Two neutrino mass orderings are possible within current experimental expectations: Normal Hierarchy (left) and Inverted Hierarchy (right). Figure from [34]

We can be more specific with this mass term (the so-called "Dirac mass" term).

$$\mathcal{L}_{\text{mass}} = -m\left(\overline{\psi}_L \psi_R + \overline{\psi}_R \psi_L\right) \tag{1.6}$$

This mass would be generated in a similar manner to the other fermion masses, through a Yukawa coupling between the fermion fields and the Higgs field. This Yukawa coupling is

$$g_\nu = \sqrt{2}\left(\frac{m_\nu}{v}\right) \tag{1.7}$$

with v being the vacuum expectation value of the Higgs field ($v = \left(\sqrt{2}G_F\right)^{-1/2} \simeq 246$ GeV [35] and m_ν being the effective electron neutrino mass. The upper limit on the neutrino mass was set by the KATRIN experiment at $m_\nu < 0.45$ eV [36]. This leads to a Yukawa coupling of $g_\nu \lesssim 10^{-12}$, an unnatural number given its distance from the couplings of the neutrino's fermionic counterparts. There is a question as to why the neutrino mass is so many orders of magnitude smaller than other fermions if the neutrino gets a Dirac mass the same way as other leptons (see Figure 1.2).

One popular solution to this open question is the seesaw mechanism, introduced by Yanagida and many others [37] [38] [39] [40]. We start with the Majorana condition:

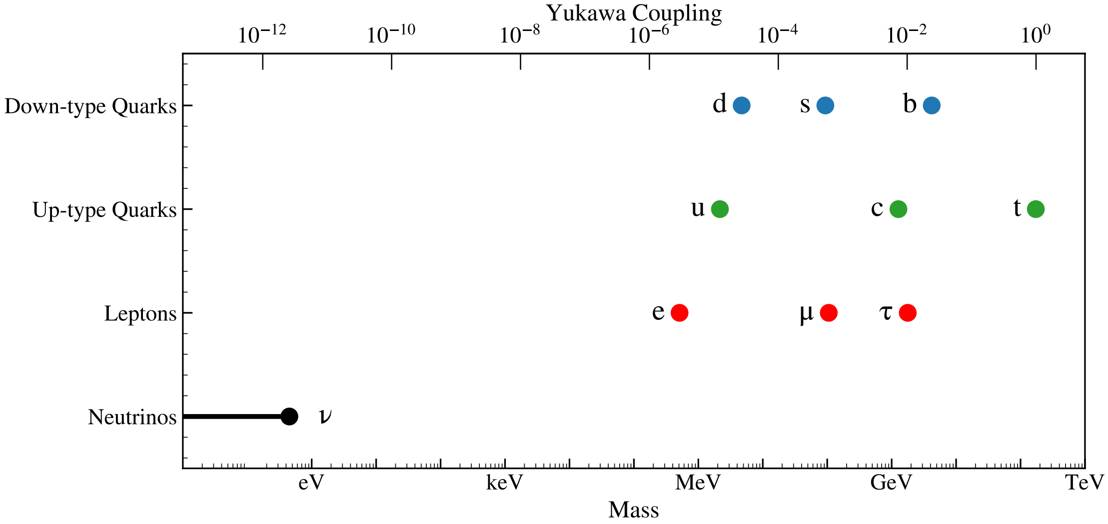

Figure 1.2: Depiction of the estimated small neutrino mass relative to the other fermions. The seesaw mechanism accounts for this difference by addition of a heavy right-handed Majorana neutrino to the Standard Model. Mass values taken from Particle Data Group [33]

$$\nu^C = \nu \tag{1.8}$$

or, in words, the charge conjugate of a neutrino is itself. The neutrino has no charge and the charge-conjugate of a left-chiral field is a right-chiral field, so this chirality encodes some key information about the neutrino. Now, if we add a right-handed neutrino and enforce the Majorana condition, we can get a "Majorana mass term" in our Lagrangian. We can also include a Dirac mass term and a left-handed Majorana mass term, so our Lagrangian will look like:

$$\mathcal{L}_{\text{mass}} = -m_D\left[\overline{\nu_R}\nu_L + \overline{\nu_L}\nu_R\right] - m_R\left[\overline{\nu_R}\left(\nu_R\right)^C + h.c.\right] - m_L\left[\overline{\nu_L}\left(\nu_L\right)^C + h.c.\right] \tag{1.9}$$

We can write this in matrix form which starts to become more illustrative:

$$\mathcal{L}_{\text{mass}} = \begin{pmatrix} \overline{\nu_L} & \overline{\left(\nu_R\right)^C} \end{pmatrix} \begin{pmatrix} m_L & m_D \\ m_D & m_R \end{pmatrix} \begin{pmatrix} \left(\nu_L\right)^C \\ \nu_R \end{pmatrix} + h.c. \tag{1.10}$$

We take m_L to be zero because such a term violates the gauge symmetry of electroweak theory. Thus, our mass matrix is of the form

$$\mathcal{M} = \begin{pmatrix} 0 & m_D \\ m_D & m_R \end{pmatrix} \tag{1.11}$$

where m_R is a heavy Majorana mass scale and m_D is a typical Dirac mass scale. We find the mass eigenvalues of this matrix to be $\lambda = \frac{1}{2}\left(m_R \pm \sqrt{m_R^2 + 4m_D^2}\right)$. In the limit of $m_R \gg m_D$, one of the eigenvalues is $\lambda_+ \approx m_R$ and the other is $\lambda_- \approx -\frac{m_D^2}{m_R}$. Note that while there is an unphysical minus sign in front of this mass eigenvalue, we can reverse that sign by taking advantage of the phase factor picked up from the Majorana condition (more information in [41]).

We see here the relevance of the term "seesaw." As this Majorana mass scale, m_R, increases, the heavy mass eigenstate λ_+ increases and the light mass eigenstate λ_- decreases (assuming the Yukawa coupling of neutrino fields to the Higgs field is of a similar strength as it is for other fields; a natural choice). m_R must be generated from some physics beyond the Standard Model, and the next energy scale at which we expect new physics to appear is the GUT scale. At this energy scale, the coupling constants of the strong force, weak force, and electromagnetic force are expected to converge to a single value. It is natural that this scale mass should appear at the GUT scale ($m_R \sim 10^{16}$ GeV) to produce a Dirac mass below 1 eV. The simplest model that automatically includes this right-handed neutrino is the SO(10) GUT model.

The mechanism discussed above is only one formation of the seesaw mechanism—Type 1. This is the simplest version of the seesaw mechanism which helps explain a number of phenomena (the comparatively tiny neutrino masses, the absence of visible right-handed neutrinos, and leptogenesis, to be discussed in the next section). This is also an extension of the Standard Model and is a compelling theory due in part to its simplicity.

1.3 Leptogenesis

A major unsolved problem in physics involves the matter-antimatter asymmetry of the universe. It is thought that in the first moments of the universe, equal parts matter and antimatter were created. How, then, do we live in a matter-dominated universe today? If the assumption that there was an initial symmetry between baryonic and antibaryonic matter is true, there must be some process by which baryonic matter became the “preferred” matter of the universe.

In 1967, Sakharov proposed three necessary conditions for a process to generate this baryon asymmetry [42]: 1) there exists a process that violates baryon number conservation, 2) both C and CP symmetry are violated in said process, and 3) the process must occur out of thermal equilibrium. Such a process that fulfills these conditions is known as “baryogenesis.”

One compelling model for baryogenesis was introduced by Fukugita and Yanagida in 1986 with their “baryogenesis through leptogenesis” theory, or “leptogenesis” for short [43]. This proposal—in which a heavy right handed Majorana neutrino decays to an antilepton (or lepton) and a Higgs—meets all three of Sakharov’s conditions. Through sphaleron processes an antilepton asymmetry generated can be converted to a baryon asymmetry. The introduced heavy right-handed neutrinos (of seesaw mechanism fame) have a Yukawa coupling to the Higgs and doublet-leptons. Since the weak interaction already maximally violates C symmetry and CP symmetry is violated by the complex phases in the Yukawa coupling, you can get more anti-leptons than leptons. These heavy neutrinos decouple much earlier than Standard Model particles so they will quickly begin to decay in the early universe. Once the universe cools below their mass scale, you avoid crossing symmetry creating more of these heavy neutrinos and you “freeze-out” this asymmetry.

This universal baryon asymmetry is often parameterized through the estimated ratio of the number density of baryons minus antibaryons to the number density of photons in the universe,

$$\frac{\eta_b - \eta_{\overline{b}}}{\eta_\gamma} \approx \frac{\eta_b}{\eta_\gamma} \approx 6.0 \times 10^{-10} \tag{1.12}$$

The baryon number density is found either through the ΛCDM model and cosmic microwave background (CMB) measurements or through inference from Big Bang Nucleosynthesis of the primordial abundance of deuterium [44] [45] [46]. Interestingly enough, Fukugita and Yanagida’s baryogenesis through leptogenesis model predicts a resulting baryon asymmetry near the observed asymmetry.

Outside of baryogenesis through leptogenesis, neutrinos still play an important part in our understanding of the early universe. At early times when the rate of expansion of the universe was slower than that of the rate of weak interactions, neutrinos stayed in thermal equilibrium with other particles. When the weak interaction rate was eclipsed by the universe’s rate of expansion, neutrinos decoupled from these protons, neutrons, and electrons. This decoupling occurred at a temperature of $\sim$ 1 MeV. Neutrinos at the time of decoupling formed what is known as the cosmic neutrino background (CνB) which should still be present today, much like the CMB. This background, however, contains extremely low energy neutrinos and is unlikely to be measured in the near future with current neutrino detection techniques. Other effects that neutrinos have on cosmology that can help in neutrino mass measurements are effects on Big Bang nucleosynthesis and the relative abundances of elements, the CMB, and the large scale structure of the late universe.

Neutrinos are clearly a great testbed for a number of unsolved problems in physics. The problem we started with in this thesis is the matter-antimatter asymmetry and as was described, a well-motivated explanation for this phenomenon is leptogenesis. Another fascinating problem deals with the scale of the neutrino mass, for which we described the seesaw mechanism. Both of these theories predict Majorana neutrinos, which should mediate neutrinoless double beta decay.

1.4 Neutrinoless Double Beta Decay

In particular isotopes with an even number of both protons and neutrons, beta decay is energetically forbidden. The final nuclear state of the nucleus with one more proton may have a higher binding energy than the initial nuclear state and thus, single beta decay would violate energy conservation. However, if the nucleus with two more protons has a lower (and thus more favorable) binding energy due to spin-coupling, there can be two "simultaneous" beta decays, known as double beta decay. There are a number of naturally occurring isotopes that fall into this category and can (detectably) undergo double beta decay, of which ^{76}Ge is one. The decay is ${}^{A}_{Z}\mathrm{X} \rightarrow^{A}_{Z+2} \mathrm{Y} + 2e^{-} + 2\overline{\nu}_e$, where two neutrons in the nucleus change to two protons, and two electrons and two electron antineutrinos are emitted to conserve charge and lepton number.

The energy of the emitted electrons in double beta decay, much like standard beta decay, can be determined using Fermi's golden rule. The energy spectrum of these beta particles will be continuous up to the Q value of the associated decay because the neutrinos will carry away some fraction of the available energy.

There could exist a decay mode such that the two antineutrinos are not emitted in the decay, which we refer to as neutrinoless double beta decay ($0\nu\beta\beta$). In this decay, the neutrinos are no longer carrying away some of the energy produced in the decay so the electron energies will sum to the Q value.

This $0\nu\beta\beta$ decay mode can be mediated by neutrinos with a Majorana mass. This is particularly interesting because a discovery of this decay mode mediated in this way proves the existence of Majorana neutrinos and relates back to many of the outstanding questions discussed previously in this thesis. However, $0\nu\beta\beta$ can be mediated by other processes even if the Majorana mass of the neutrino is negligible or if the neutrino is a purely Dirac particle.

There are more reasons than uncovering the nature of the neutrino to search for $0\nu\beta\beta$. One of those motivations is based in our current Standard Model's symmetries. The gauge group that describes the Standard Model is $\mathrm{SU(3)}\times\mathrm{SU(2)_L}\times\mathrm{U(1)}$. An interesting result is that there are "accidental symmetries" stemming from the classical Lagrangian density. Baryon number B, lepton number L, and individual flavor lepton numbers L_e, L_μ, and L_τ are all found to be conserved in the theory without that conservation being enforced a priori. These symmetries, however, are anomalous symmetries which is to say that they can be violated by quantum fluctuations. The non-anomalous global symmetries that appear in the full Standard Model theory are $B - L$ and linear combinations of $L_i - L_j$, with i, j being the three lepton flavors. Certainly, $L_i - L_j$ cannot be a conserved quantity due to neutrino oscillations. Thus, $B - L$ is the only remaining accidental symmetry that has not been observed to be violated. $B - L$ is clearly inseparable from baryogenesis and leptogenesis and the discovery of $0\nu\beta\beta$ would be the nail in the coffin of this final accidental symmetry. It would be of great interest if all four of these accidental symmetries were violated—specifically by neutrino mass. It would also be interesting if there is something special about $B - L$ that allows it to maintain its conservation status. Regardless, $0\nu\beta\beta$ is a great probe for this.

There are multiple models as to how $0\nu\beta\beta$ could occur. The simplest of them all is via light neutrino exchange, in which one nucleon absorbs the neutrino emitted by the other. The Feynman diagram for this process is shown in Figure 1.3.

In this light-neutrino exchange treatment, we have a decay rate of

$$\Gamma^{0\nu}_{1/2} = G_{0\nu}\ g_A^4\ |M_{0\nu}|^2\ \ |m_{\beta\beta}|^2 \tag{1.13}$$

where $G_{0\nu}$ is the phase factor, g_A^4 is the axial-vector coupling constant, $|M_{0\nu}|$ is the nuclear

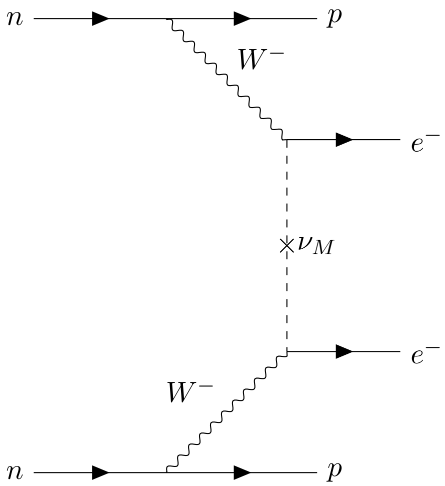

Figure 1.3: Feynman diagram for $0\nu\beta\beta$ in the case that it is mediated by light neutrino exchange

matrix element, and $m_{\beta\beta}$ is the effective Majorana neutrino mass.

The phase factor $G_{0\nu}$ (typically of order $\mathcal{O}(10^{-14}\text{yr}^{-1})$ [47] [48] comes into the calculation via an integral over available phase space of the interacting particles' momenta and energies through Fermi's golden rule. This phase factor determines the likelihood of the decay to occur based solely on the kinematics of the system.

The axial-vector coupling constant $g_A = -1.2753$ [33] connects the weak interaction to the nucleons in the decay. $0\nu\beta\beta$ is dominated by Gamow-Teller transitions (although there are Fermi, scalar, and tensor contributions), so the g_A term is often factored out of the equation. This value is very well-known but is thought to be susceptible to a "quenching effect" (discussed below).

The nuclear matrix element (NME) accounts for the amplitude of the transition from the initial (N, Z) nuclear state to the final (possibly excited) $(N, Z + 2)$ state and is a combination of long and short-range matrix elements in the light neutrino exchange case. These terms depend on the distance between decaying nucleons, and thus, the distance of the exchanged virtual neutrinos. This affects how $0\nu\beta\beta$ is mediated.

Lastly, the effective Majorana mass, $m_{\beta\beta}$, is a way to define the sum of the contributions of the neutrino mass eigenstates scaled by their flavor mixing amplitudes, given by the PMNS matrix.

There is also a term dependent on the Majorana phases α_i. Specifically,

$$m_{\beta\beta} = \left| \sum_{i=1}^{3} \left| U_{ei}^2 \right| e^{i\alpha_i} m_i \right| \tag{1.14}$$

The U_{ei} term shows up at the electroweak vertices in the Feynman diagram and the m_i term shows up at the mass term insertion in the virtual neutrino. We often think of the $m_{\beta\beta}$ parameter space when talking about $0\nu\beta\beta$ limits. The allowed parameter space for $m_{\beta\beta}$ as a function of different unknown parameters is shown in Figure 1.4.

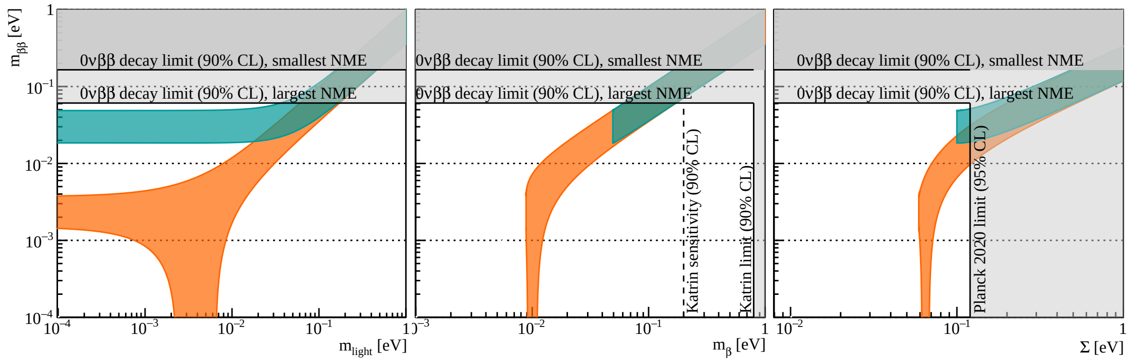

Figure 1.4: Maximally allowed parameter space for $m_{\beta\beta}$ as a function of the lightest neutrino mass (m_{light}), the electron neutrino mass (m_β), and the sum of the neutrino masses (Σ). The orange and teal regions show the allowed parameter space assuming normal and inverted ordering, respectively. The gray-shaded regions are regions of parameter space already excluded by $0\nu\beta\beta$ experiments, direct mass measurements, and cosmological observations (and is slightly out of date). Plot from [49].

While the effective Majorana mass is a value to be found experimentally, there are other sources of uncertainty in the theoretical calculation of the $0\nu\beta\beta$ half-life at around factors of 2-3. A large amount of that uncertainty comes from the calculation of relevant NMEs. NME calculations can be carried out through a variety of methods, including the many body methods (nuclear shell model (NSM), quasiparticle random-phase approximation method (QRPA), interacting boson model (IBM), energy-density functional theory (EDF)) and "ab initio" methods. There are disagreements even between the same methods due to the complexity of this calculation. Work is ongoing to extend these ab initio methods to larger nuclei. A number of light neutrino exchange NME calculations for ^{76}Ge are shown in Figure 1.5, as well as the first theoretical uncertainties with proper statistical interpretations applied to these ab initio NME calculations.

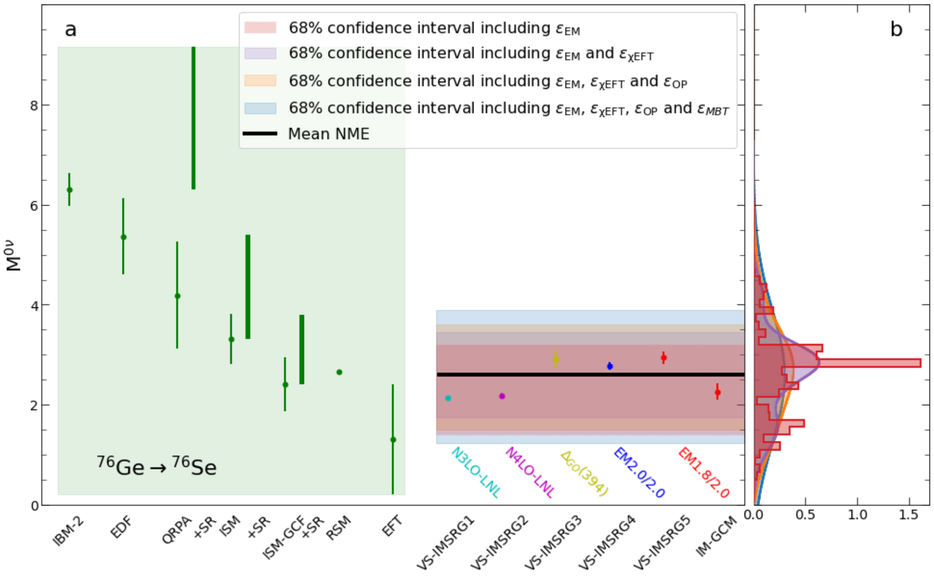

Figure 1.5: Comparison of $0\nu\beta\beta$ NME calculations in ^{76}Ge from many-body nuclear models and ab initio methods, from [50].

Similarly, there is some uncertainty due to so-called "g_A quenching." The axial coupling g_A plays a role in the decay rate calculations of standard Gamow-Teller β decays. These rates were historically overestimated in calculations for larger nuclei and thus a "fudge factor" of ~ 0.7 was applied to match the calculated and measured decay rates. This suppression is now attributed to the truncation of the Hilbert space in nuclear shell model calculations—there are also smaller quark-level effects. Now the NMEs must be estimated with that quenching physics and updated. Despite all this uncertainty and dependence on nuclear models and the Majorana neutrino mechanism, discovery of $0\nu\beta\beta$ is certain to clear up a number of questions about all the physics described above.

In an embedded calorimetry experiment—one in which the source and detector are one and the same—a $0\nu\beta\beta$ signal is expected to occur with energy at the Q-value of the decay, $Q_{\beta\beta} = 2039$ keV. Therefore, there are a number of techniques to suppress backgrounds that mimic $0\nu\beta\beta$ signals. In addition, intense care must be taken to reduce backgrounds as much as possible when building the experiment. This includes using clean materials, conducting the experiment under overburden, and so on. Experiments searching for $0\nu\beta\beta$ essentially boil down to counting experiments near $Q_{\beta\beta}$. Ultimately, these experiments are making compromises to maximize $0\nu\beta\beta$ counts and minimize backgrounds. Analysis cuts can help remove backgrounds, but at the expense of lower signal efficiency. The aim is to have such a low background rate that only a few $0\nu\beta\beta$ counts will be sufficient to claim a discovery.

The discovery sensitivity for a $0\nu\beta\beta$ search represents the number of signal counts needed for an experiment to have a 50% chance of claiming a discovery above background at the 3σ (99.73%) confidence level (CL). This confidence level is lower than that of other particle physics searches (typically 5σ) for a few reasons. The $0\nu\beta\beta$ signal is expected at only one energy; the "look-elsewhere" effect is not applicable. From calibrations most experiments have a clear template for how the signal should appear in their detector. Additionally, if one experiment detects $0\nu\beta\beta$ at $> 3\sigma$—provided there is a robust $0\nu\beta\beta$ program at that point in the future—the parameter space will be limited for other experiments to eventually detect it. Plus, once you discover it at 3σ, you can ideally just run for longer to get to 5σ. The community will require two isotops with a $> 3\sigma$ signal to claim discovery.

While the discovery sensitivity refers to a number of signal counts, experiments that do not make a discovery will often also present result as an exclusion sensitivity. An experiment's median exclusion sensitivity is the median 90% CL half-life upper limit that an experiment is expected to achieve in the absence of a signal.

These metrics are inherently related to the number of $0\nu\beta\beta$ events we detect in an experiment, given by:

$$N_{0\nu\beta\beta} = \ln(2)\left(\frac{N_A M t \epsilon}{m_{\mathrm{iso}} T^{1/2}_{0\nu}}\right) \tag{1.15}$$

In Equation (1.15), N_A is Avogadro's number, M is the mass of the decaying isotope, t is the dead-time-corrected run-time of the experiment, ϵ is the signal detection efficiency, m_{iso} is the molar mass of the decaying isotope, and $T_{0\nu}^{1/2}$ is the half-life of the decay. The discovery and exclusion sensitivities are shown in terms of signal counts as a function of background counts in Figure 1.6.

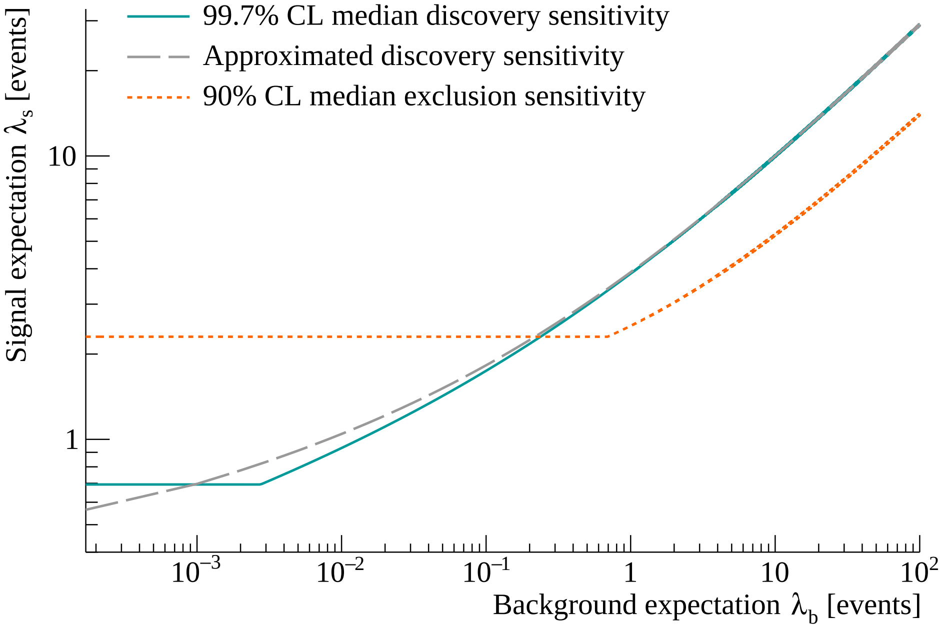

Figure 1.6: Median discovery sensitivity and exclusion sensitivity, in terms of signal counts, as a function of background counts. Also shown is an approximation of the discovery sensitivity from [51]. Plot from [49].

An important aspect of current and future $0\nu\beta\beta$ experiments is their sensitivity to discovery of the decay and the probeable parameter space (as it relates to neutrino masses). $0\nu\beta\beta$, if it does occur, is an exceedingly slow process. The current leading experimental half-life limits (in addition to the corresponding $m_{\beta\beta}$ values) are shown in Table 1.2. The leading limit in ^{76}Ge is $T_{1/2} > 1.9 \times 10^{26}$ yr (at 90% CL) from the combined limit of LEGEND-200, MAJORANA DEMONSTRATOR, and GERDA [52]. Other relevant limits set are shown in Table 1.2.

Experiment	Isotope	$Q_{\beta\beta}$ (keV)	$T_{1/2}$ (yr)	$m_{\beta\beta}$ (meV)
LEGEND-200 [52]	^{76}Ge	2039	1.9×10^{26}	75-200
KamLAND-Zen 800 [53]	^{136}Xe	2458	3.8×10^{26}	28-122
CUORE [54]	^{130}Te	2528	3.2×10^{25}	75-350
CUPID-0 [55]	^{82}Se	2998	4.6×10^{24}	263-545
AMoRE-I [56]	^{100}Mo	3034	2.9×10^{24}	210-610

Table 1.2: Leading experimental limits on $0\nu\beta\beta$ half-life and the corresponding limits on $m_{\beta\beta}$ for 5 of the main $0\nu\beta\beta$ isotopes. Next-generation experiments seek to increase these half-life limits by at least 1-2 orders of magnitude to probe the inverted mass hierarchy region.

Chapter 2

LEGEND Overview and Germanium Detectors

The Large Enriched Germanium Experiment for Neutrinoless-$\beta\beta$ Decay (LEGEND) is searching for neutrinoless-double beta decay ($0\nu\beta\beta$) in ^{76}Ge. The current iteration of the experiment is LEGEND-200 located at the Laboratori Nazionali del Gran Sasso (LNGS) in the Abruzzo region of Italy. The ultimate goal of this phase of the experiment is to deploy 200 kg of high purity germanium (HPGe) detectors enriched in ^{76}Ge into a liquid argon active veto; 142.5 kg of Ge were deployed for the first data-taking period [52]. LEGEND-1000 is the proposed second phase, ton-scale experiment consisting of 1000 kg of HPGe detectors [57]. The LEGEND collaboration was formed via the merger of two previously existing ^{76}Ge $0\nu\beta\beta$ experiments: Majorana Demonstrator (located in the Sanford Underground Research Facility in Lead, South Dakota and GERDA, located in the same cryostat as LEGEND-200 at LNGS.

2.1 LEGEND-200 Overview and Status

LEGEND-200 consists of strings of germanium detectors enriched in ^{76}Ge deployed in an active liquid argon veto. Surrounding the liquid argon cryostat is a muon veto water tank. The experiment also has considerable overburden given its location under the Gran Sasso mountain. The analog signals from the germanium detectors (discussed in Section 2.3.2 are read out synchronously with the liquid argon signals, digitized, and processed for analysis. The low-level analysis is similar to the analysis discussed in Section 4.4, with data cleaning, energy calibration, digital signal processing optimizations, and analysis cuts.

LEGEND-200 is (as of the writing of this thesis) taking data to add to its current data-set, detailed in our first results [52]. The half-life limit from that result is set at $T^{0\nu}_{1/2} > 1.9 \times 10^{26}$ yr at 90% confidence level (CL) with a limit on the effective Majorana mass of $m_{\beta\beta} < 75 - 200$ meV.

The background index for this publication is $0.5^{+0.3}_{-0.2}$ cts/(keV ton yr) with 11 counts after cuts in the 240 keV analysis window over an exposure of 61.0 kg yr. This illustrates the necessity of understanding and reducing/rejecting any backgrounds in this region of interest near $Q_{\beta\beta}$ to improve LEGEND's sensitivity. Only a few counts are needed to claim a discovery given a quasi-background-free experiment. The energy spectrum of the first LEGEND-200 dataset is shown in Figure 2.1.

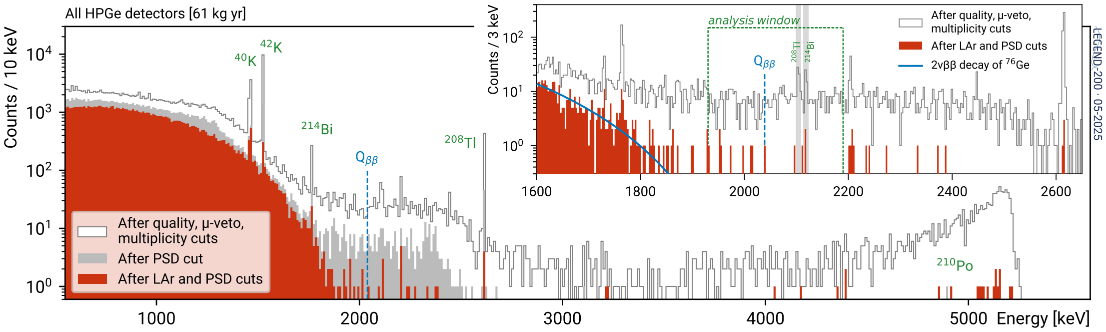

Figure 2.1: First physics result from LEGEND-200, with analysis cuts on the full energy spectrum and on the region of interest. From [52]

2.2 LEGEND-1000

LEGEND-1000 aims to improve upon the already strong foundation of LEGEND-200 through developed Ge detector technologies, more efficient active shielding, cleaner materials, and upgraded electronics. The goal of LEGEND-1000 is to deploy 1000 kg of HPGe detectors and run for 10 years of livetime (or reach an exposure of 10 ton yr). With a background index goal of $< 1 \times 10^{-5}$ cts/(keV kg yr) LEGEND-1000 seeks a 99.7% CL discovery sensitivity greater than 10^{28} years. This corresponds to a limit on the effective Majorana mass of $m_{\beta\beta} > 9-21$ meV, potentially covering the inverted-ordering neutrino mass scale.

One of the key innovations proposed for LEGEND-1000 relative to LEGEND-200 is the sole use of the inverted coaxial detector geometry (see Section 2.3.3 for more details). This should reduce background due to the higher mass per crystal and the performant energy resolution of these detectors. The low-mass front-end electronics will move to a CMOS ASIC design, providing more radiopure materials near detectors. There are plans to utilize underground argon for the liquid argon veto to reduce ^{39}Ar and ^{42}K backgrounds, as discussed in Section 2.4.1. Other analysis, data acquisition, and hardware developments are being considered as well.

2.3 Germanium Detectors

LEGEND relies on the simultaneous operation of many HPGe detectors. ^{76}Ge is known to undergo double beta decay ($2\nu\beta\beta$) with half-life $T^{2\nu}_{1/2} = (2.022 \pm 0.018_{\text{stat}} \pm 0.038_{\text{sys}}) \times 10^{21}$ yr [58]. One challenge of a $0\nu\beta\beta$ search is having the energy resolution to separate the $2\nu\beta\beta$spectrum from any potential counts in the $0\nu\beta\beta$ peak at $Q_{\beta\beta} = 2039.06$ keV. ^{76}Ge is a competitive isotope in the $0\nu\beta\beta$ search partially due to excellent energy resolution, reaching a FWHM of 0.12% at $Q_{\beta\beta}$ in the Majorana Demonstrator [59], a world-leading result. Other benefits of using ^{76}Ge are the decades of knowledge from prior germanium experiments and the “source = detector” configuration which minimizes inactive mass in the experiment, just to mention a few here.

2.3.1 Basic Semiconductor Physics

When cooled down to near liquid nitrogen temperatures (~ 77 K), germanium behaves as a semiconductor material—technically, germanium is a semiconductor at room temperature, but thermal noise promotes too many electrons to the conduction band. This semiconductor behavior allows germanium to successfully “detect” ionizing radiation. Incident radiation (in our case, α, β, and γ particles) will interact with the germanium crystal and ionize electrons in the valence band. Provided there is enough energy exchanged (on average, 2.96 eV at 77 K [60]), these valence electrons can traverse the band gap (shown in Figure 2.2) and populate the conduction band. Electrons in the conduction band are no longer bound to the crystal and are free to drift under the influence of some external electric field. Similarly, we can think of the new absence of that valence electron as its own quasi-particle hole. Holes and electrons are thus created in pairs, with the number of charge carrier pairs created proportional to the energy deposited by the initial radiation.

The HPGe detectors deployed in LEGEND are *p*-type detectors, which is to say they are grown

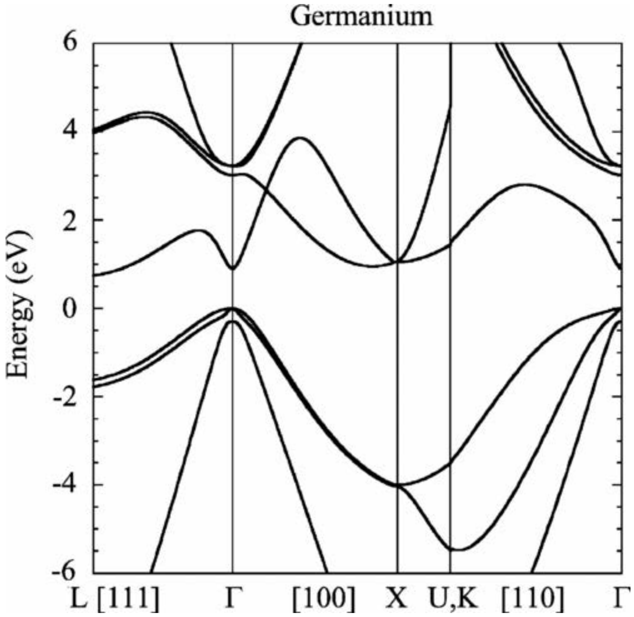

Figure 2.2: Calculation of the Ge bandgap at T = 0 K from [61].

with some impurity profile with an excess amount of electron acceptors and thus, holes. Similarly, a semiconductor can be n-type with excess electron donors. If we connect our p-type germanium with a Li-diffused $n+$ region, we create a p—n junction. This p—n junction creates an interface between two regions of the detector with excess holes and electrons, respectively. These free charge carriers will interact and annihilate with each other, leaving behind a net negative charge on the p-type side and a net positive charge on the n-type side. This region of now non-zero electric field is known as the *depletion region* that points towards towards the p-type region, and specifically towards our $p+$ contact, usually implanted with boron. This depletion region grows from the larger $n+$ contact as we apply a positive bias voltage to that contact and ground the smaller $p+$ contact. At the *depletion voltage* of the detector, the entire volume is depleted and has a non-zero electric field. This electric field has two contributions: the field generated by the impurity profile and the field generated by the applied bias voltage. The impurity profile is a somewhat tunable parameter during the growing of these crystals and is tuned to create clean signals in the detector. Diagrams showing the formation of the p—n junction, detector depletion, and electric field contributions are shown in Figure 2.3.

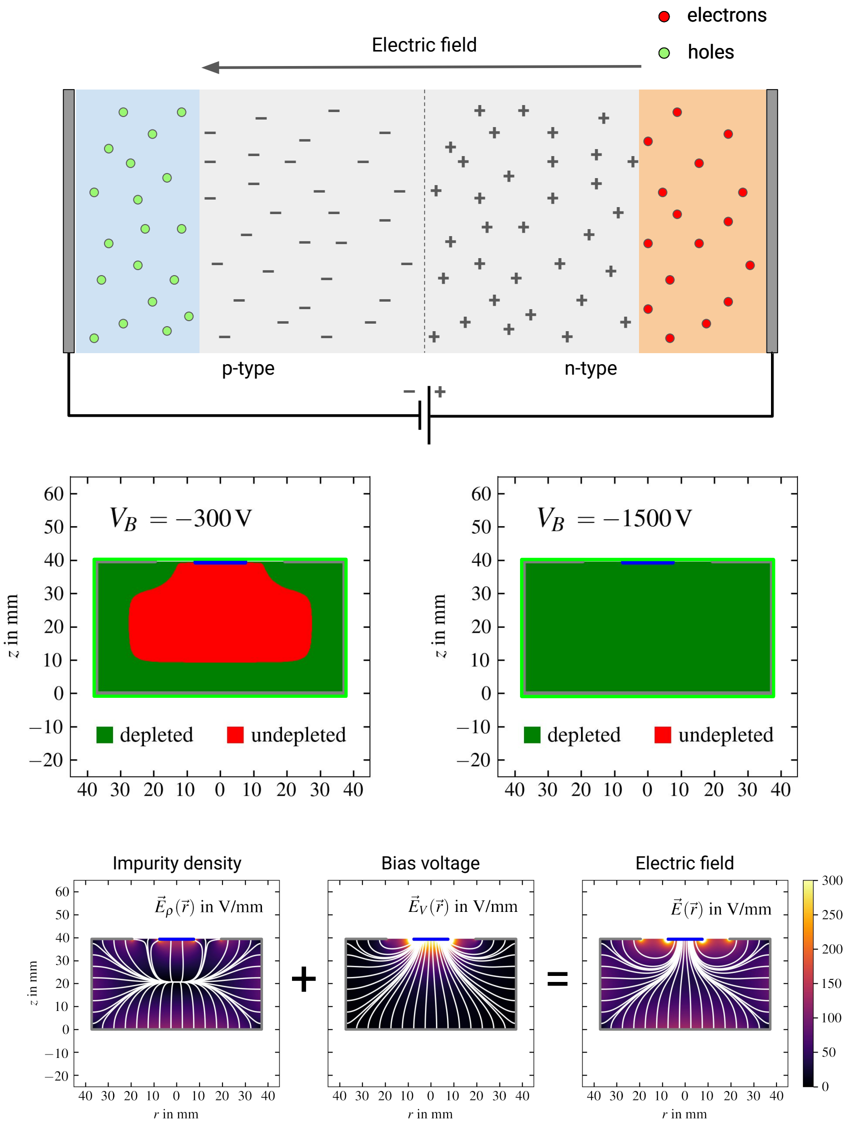

Figure 2.3: (*top*) p—n junction formation in a p-type germanium detector. (*middle*) Depletion region of a germanium detector during biasing. (*bottom*) Electric field contributions from detector impurity profile and bias voltage. *Images courtesy of Felix Hagemann.*

The detector now behaves like a reverse-biased diode such that current will not flow through the germanium. The only current (aside from unwanted leakage current, reduced by blocking contacts) that flows is from the drift of charge carriers which serves as our signal.

2.3.2 The Shockley-Ramo Theorem

The generation of signals due to drifting charge carriers is governed by the Shockley-Ramo theorem [62] [63]. These signals (in LEGEND and KrSTC) are collected by an electrode placed in good electrical contact with the boron-doped $p+$ point contact, which itself is connected to a feedback capacitor and a feedback resistor. This capacitor collects the charge from the electrode and that charge is bled off by the resistor on a time scale much less than the event rate. This RC circuit gives our waveforms their characteristic exponential decay.

One might naively think that when a number of charge carriers are created in an ionizing energy deposition, the signal results from those individual holes and electrons being “captured” at the contacts. This would result in a time-delayed, discretized signal and not smooth waveforms as we observe. Rather, the signal starts the instant the charge carriers begin to drift under the influence of the electric field. These charges drifting through the crystal induce a current on the readout electrode due to changing electrostatic flux lines ending on said electrode. For convenience, we can define a *weighting field* $\vec{E}_0$ and a *weighting potential* φ_0. These concepts differ from the true electric field and electric potential. We set the voltage of our readout electrode to 1 V and of all other electrodes to 0 V and solve the Laplace equation $\nabla^2\varphi_0 = 0$ with those boundary conditions. This defines the weighting potential, and the weighting field is simply the negative gradient of the weighting potential. We have turned our electrostatics problem into a purely geometric problem here which makes calculating signals for segmented detectors significantly easier. An example weighting potential for a PPC detector is shown in Figure 2.4. One important feature is that the weighting potential for these detectors changes rapidly near the $p+$ point contact, so the signals in LEGEND are said to be “hole-dominated” as the holes induce the most signal when they traverse this high $\Delta\varphi_0$ region.

Once we determine our weighting potential and field, we can calculate the current induced on our readout electrode with Equation (2.1):

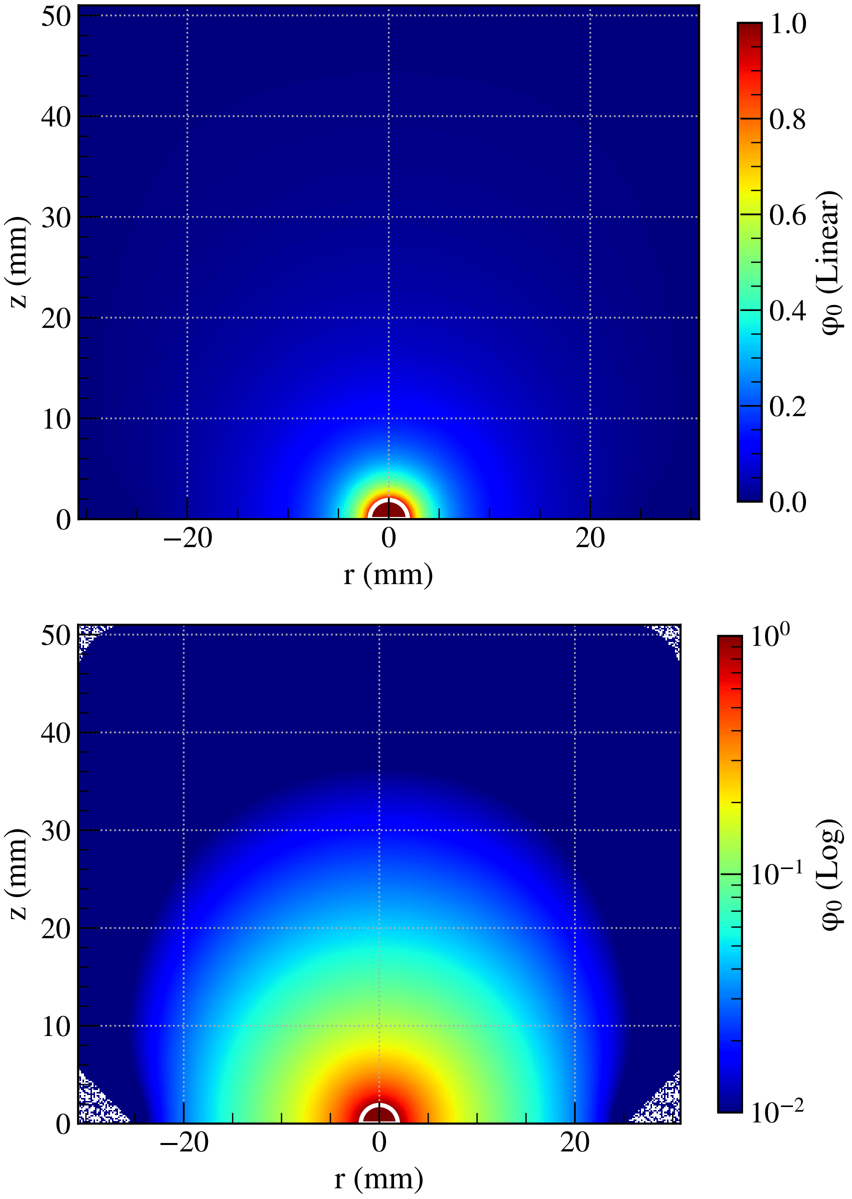

Figure 2.4: Weighting potentials of a PPC germanium detector in (*top*) linear and (*bottom*) log z scales, with $p+$ contact shown in white. Simulation run with siggen [64].

$$i = q_{\text{drift}} \left(\vec{v}_{\text{drift}} \cdot \vec{E}_0 \right) \tag{2.1}$$

We can also consider the total charge induced by drifting charges by integrating over time, as in Equation (2.2):

$$Q = q_{\text{drift}} \Delta\varphi_0 \tag{2.2}$$

The charge induced on our readout electrode (and thus, our feedback capacitor) is proportional to the sign of the drifting charge carrier and the change in weighting potential that it “experiences” across its drift path. Positively charged holes will drift towards the $p+$ contact and experience an increase in weighting potential. Negatively charged electrons will drift towards the $n+$ surface and experience a decrease in weighting potential, thus also contributing positively to the total charge. The sum of these hole and electron components give us our expected waveform. The drifting charges are subject to both the electric field and the charge mobility tensor, as shown in Equation (2.3).

$$\vec{v_i} = \mu_i \vec{E} \tag{2.3}$$

where $\vec{v_i}$ is the electron/hole velocity, μ_i is the mobility tensor, and $\vec{E}$ is the electric field.

The calculation of charge carrier drift paths through the germanium crystal is not as straightforward as a simple electric field calculation. For one, holes and electrons have different mobilities. These mobilities are temperature and field dependent; at liquid nitrogen temperatures the mobilities are comparable. In the low-field regime ($|\mathbf{E}| \lesssim 50$ V/mm) the charge carriers behave ohmically with a linear relationship between velocity and field magnitude—in this regime, holes are very slightly faster. In the intermediate field regime ($|\mathbf{E}| \sim 50$–300 V/mm) the charge carriers show a quadratic deviation from this ohmic behavior—here electron velocity overtakes hole velocity. Finally, in the high field regime ($|\mathbf{E}| \gtrsim 300$ V/mm), the carriers reach a saturation velocity [65].

The crystal axes of the germanium further complicate things. Atomic germanium forms a face-centered diamond-cubic geometry, as seen in Figure 2.5

This geometry has 3 unique crystallographic directions represented by the Miller indices [100], [110], and [111]. These axes are not orthogonal to one another. Charge carriers have different mobilities depending on the orientation of their velocity vector to the crystal axes. The difference

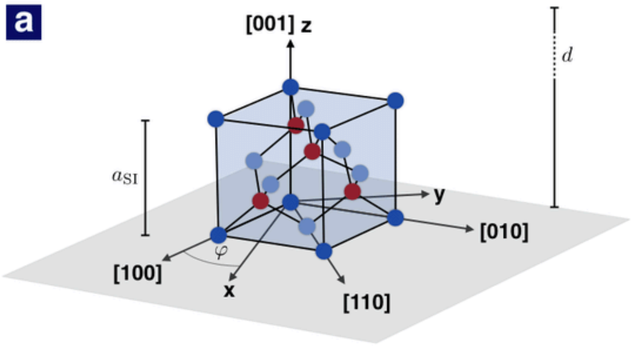

Figure 2.5: face-centered diamond cubic crystal structure geometry of germanium, from [66].

in mobility for holes and electrons are shown in Figure 2.6. The germanium detectors in LEGEND are grown such that the [100] direction with the highest mobility is always aligned axially pointing through the $p+$ point contact and towards the $n+$ region.

There are other factors that can affect the charge collection in our detectors. Some of those considerations are: size of a charge cloud, self-repulsion of that cloud, thermal diffusion under influence of an electric field, low-field regions (like the $n+$ region), undepleted regions in the detector, charge-trapping, and, as will be focused on in Chapter 5, surface charge distortion of the electric field.

2.3.3 Detector Geometries

There are a number of different HPGe detector geometries used in LEGEND-200. Those geometries are shown in Figure 2.7.

Coaxial detectors are a long-used and well-understood detector configuration, but with larger detector capacitances and poorer pulse shape discrimination qualities than other detector geometries. Inverted coaxial (IC) detectors were developed by detector manufactures with the help of the LEGEND collaboration to create a version of a large coaxial detector with much smaller p+ contacts and additional features to improve energy resolution and increase pulse shape discrimination efficacy. The GERDA collaboration mostly utilized broad energy germanium (BEGe) detectors which have sharp energy resolution performance. However, these BEGes are lower mass detectors

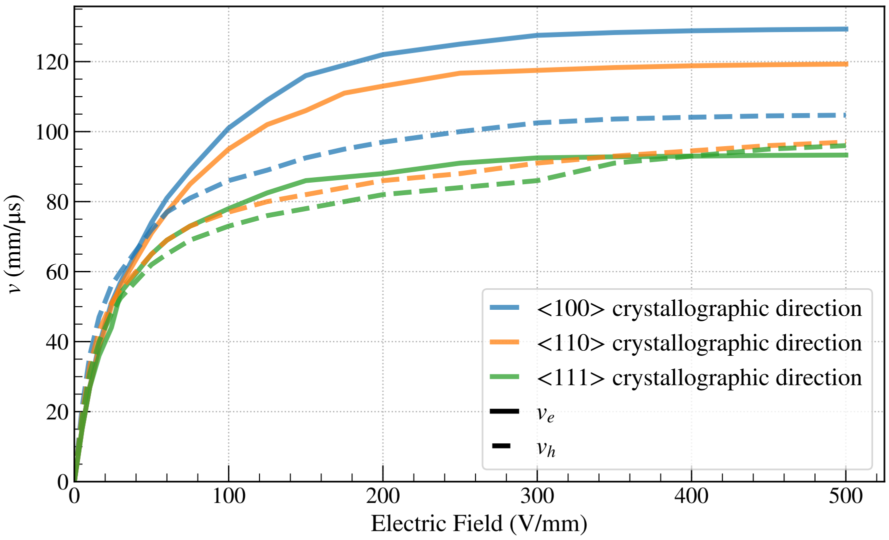

Figure 2.6: Charge carrier velocities in germanium vs. electric field strength at 77 K in different crystal axis directions. Solid lines are electron velocities, dashed lines are hole velocities. Mobility model from [65]

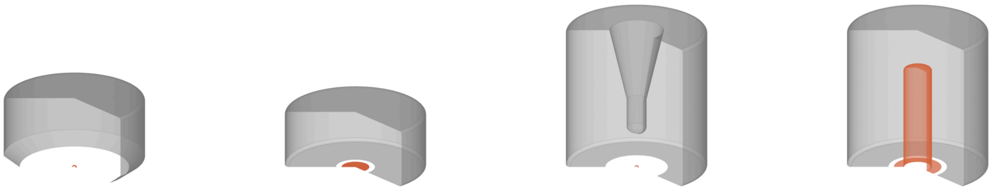

Figure 2.7: Different HPGe detector geometries deployed in the LEGEND experiment. From left: PPC, BEGe, ICPC, Coax. *Image credit to David Hervas.*

and thus require more instrumentation per unit mass. This adds unwanted backgrounds to the experiment. MAJORANA DEMONSTRATOR used mostly $p+$ point contact (PPC) detectors which will be the focus of this thesis.

These detectors have very low capacitance. This, coupled with low-noise front-end electronics [67] allowed Majorana Demonstrator to achieve a world-leading energy resolution of 0.12% FWHM at $Q_{\beta\beta} = 2039$ keV [59]. A more detailed view of a PPC detector is shown in Figure 2.8.

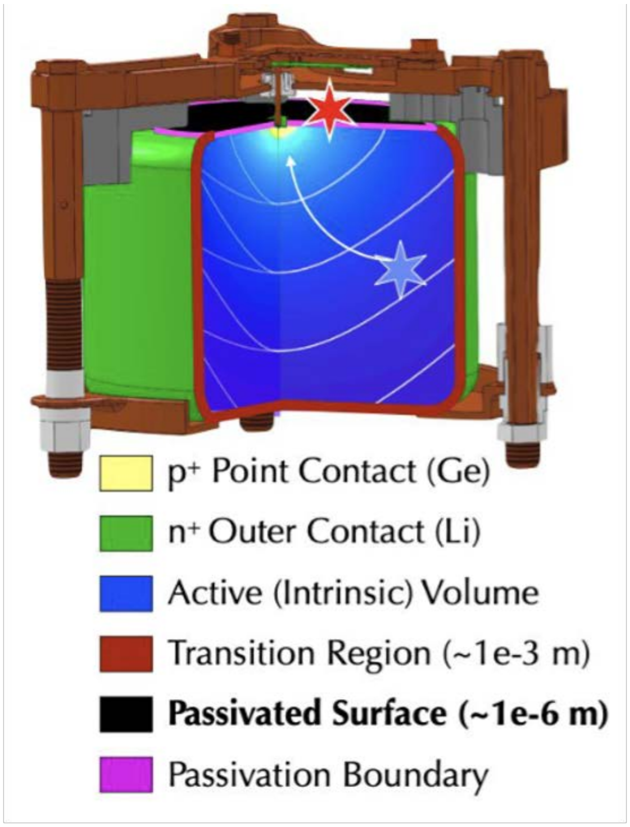

Figure 2.8: $p+$ point contact (PPC) detector geometry. Note the location of the point contact, the $n+$ contact, the transition region bordering the $n+$ contact, and the passivated surface. *Image credit: Clint Wiseman.*

The PPC detector boasts a small, $\mathcal{O}$(mm)-sized $p+$ point contact which limits detector capacitance and thus improves energy resolution. PPCs have a large $n+$ surface to which we apply bias voltage. In between these two surfaces sits the *passivated surface*. This passivated surface consists of a thin layer of insulating amorphous germanium (aGe), partially to stand off the potential difference between contacts and partially to limit surface charge buildup near the point contact. There is still expected to be charge buildup on this surface and the dead layer associated with this aGe is unknown but expected to be small. Section 5.2 will discuss this further.

2.4 Backgrounds

Limiting background events is of critical importance to LEGEND. As we will discuss in Section 2.1, the half-lives we are sensitive to are long and we aim to operate in the quasi-background-free regime. There are a number of sources of backgrounds and mitigation methods we can discuss.

2.4.1 Sources of Background

LEGEND-200 and LEGEND-1000 share most of their major sources of background. The major backgrounds of concern for LEGEND-1000 are radioactivity from the ^{238}U and ^{232}Th decay chains and "surface alphas" from ^{222}Rn. Radon gas is found in larger amounts underground and this ^{222}Rn can stick to detector surfaces and emit alphas directly into detectors. This decay chain emits a number of high energy (≥ 5 MeV) alphas which can be energy degraded near detector surfaces. Specifically, alphas penetrate $\gtrsim 10$ μm at these energies, not deep enough to punch through the ~ 1 mm-thick $n+$ transition region in PPCs, so they must be depositing their energy near the passivated surface and/or point contact. If there is some energy degradation in this region, surface alphas can show up near $Q_{\beta\beta}$ rather than at their full energy, generating a tricky background. A similar background is from ^{42}K β decays, but those βs penetrate much deeper into the detector and are not expected to be affected by any energy degradation near the passivated surface.

An interesting background to consider is ^{39}Ar. This is a long lived β-emitter with a Q-value of 565 keV [68]. While this is not in the region of interest of $0\nu\beta\beta$ it does provide a potential issue. Both ^{39}Ar and ^{42}Ar (the parent of ^{42}K) are present in atmospheric argon, the current source of argon for LEGEND-200, due to cosmogenic activation. LEGEND-1000 requires even larger amounts of argon and so these radioisotopes will be even more abundant. ^{39}Ar is already a major background at low energies for LEGEND-200 and a source of liquid argon coincidence cut inefficiency, and adding more of this isotope further hurts LEGEND's low energy program as well as dwarfs the liquid argon SiPM trigger rate. For this reason, LEGEND-1000 is looking to source underground argon which the DarkSide collaboration found to be significantly reduced in ^{39}Ar [69]. The background budget for LEGEND-1000 is shown in Figure 2.9.

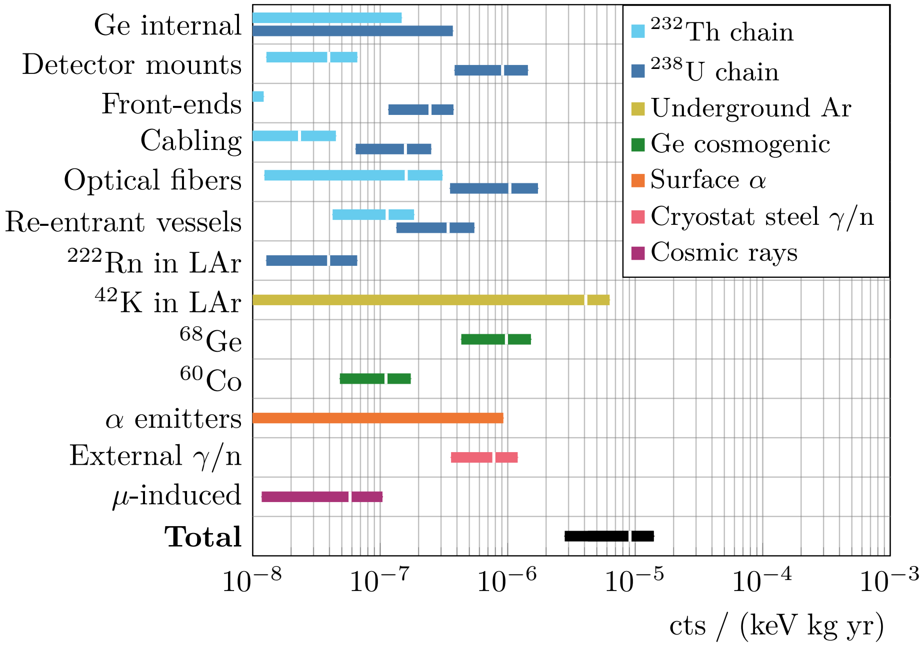

Figure 2.9: Background budget projections for LEGEND-1000. Of particular interest in this thesis is the contribution from α emitters. Plot from [57].

2.4.2 Background Reduction Methods

LEGEND combines four complementary strategies for background reduction and rejection. The first approach is passive shielding. LEGEND-200 is located (and LEGEND-1000 will be located) under 3650 m.w.e. of overburden at LNGS under Gran Sasso mountain [70]. This much overburden protects the experiment from large rates of cosmic rays which can not only yield background signals themselves (or from their progeny), but can also generate cosmogenically activated isotopes in materials near or in the detectors. Other passive shielding also blocks gammas and neutrons from the rock cavern and experimental infrastructure. LEGEND-200 sits in the same cryostat as did GERDA (with upgraded liquid argon instrumentation), offering prior knowledge regarding operations.

The second approach is active shielding. The LEGEND cryostat sits in a later water tank outfitted with photomultiplier tubes (PMTs) serving as a muon veto system to veto any external high energy muons that make it through the mountain to the experiment. Inside of this water tank is the liquid argon (LAr) cryostat. The germanium detectors are immersed in LAr which scintillates when exposed to ionizing radiation—it also cools the detectors to an operating temperature of ~ 87 K. This LAr cryostat is equipped with a number of silicon photomultipliers (SiPMs). In the event of some external radiation moving through the LAr to a HPGe detector, these SiPMs will detect the LAr scintillation light in time coincidence with the germanium signal and can veto them. In order to increase the light collection uniformity throughout the array, LEGEND uses wavelength-shifting fibers to shift the argon scintillation light to a frequency visible by the SiPMs.

The third approach is ultra clean materials. Any significant radioactivity in or on hardware near germanium detectors can ruin LEGEND's background index and sensitivity. To this end we use underground electroformed copper [71]. Also used are custom-made low-mass front-end electronics and other low-mass materials to limit the material near detectors and thus limit potential nearby radioactivity. Cleaning procedures for carefully-made materials placed in the cryostat are crucially important to keep backgrounds down. Even germanium detectors are never flown on planes but are shipped via boat when needed to limit exposure to cosmic rays.

The fourth approach is pulse shape discrimination. The Shockley-Ramo theorem tells us that for detectors with non-linear weighting potentials, you can get unique waveform shapes depending on the location(s) of energy deposition(s). One example of the uniqueness of waveform shapes is the difference between single-site and multi-site events.

Single-site events are good proxies for how $0\nu\beta\beta$ events should look. The βs emitted in $0\nu\beta\beta$ are expected to deposit their energies within a small range near the decay site, $\mathcal{O}(1\text{ mm})$. The βs should also deposit their energies on timescales much shorter than the drift time of the resulting charge carriers. This means that $0\nu\beta\beta$ should give a smooth, clean waveform without any kinks. This is a good example of a single-site event with localized energy deposition and a resulting smooth waveform. In contrast to $0\nu\beta\beta$, a photon can Compton scatter in the detector, depositing its energy in multiple sites. These deposition sites can be separated by $\mathcal{O}(1\text{ cm})$ in our detectors. This results in multiple distinct charge clouds that can arrive in the region of rapidly varying weighting potential at different times, resulting in a clear kink in the waveform. An example of this and other waveform shapes is shown in Figure 2.10.

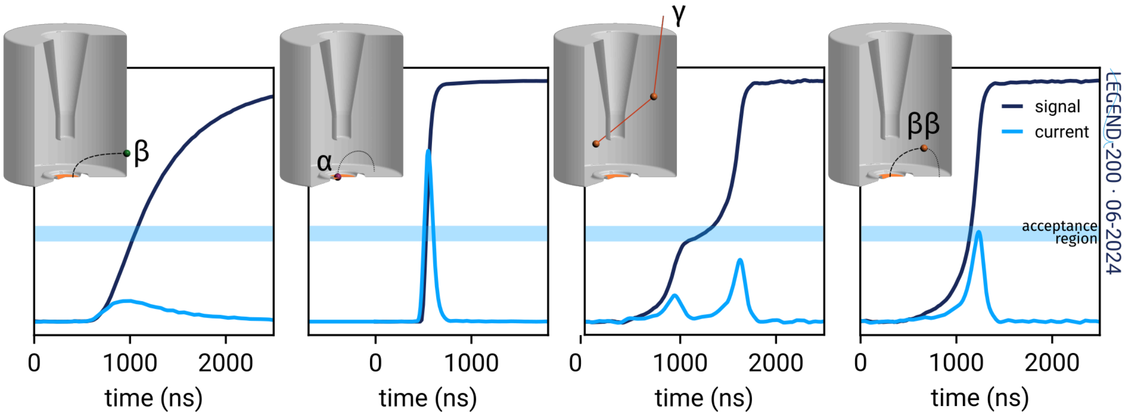

Figure 2.10: Germanium charge and current waveforms for different event types. Notice the capability of a cut on the current waveform tagging non-$0\nu\beta\beta$-like events. *Image credit:Luigi Pertoldi and George Marshall.*

Another distinction between different waveforms is in the rate of change of the waveform at the beginning and end of its drift time. This dynamic is also driven by the location of the energy deposition. For example, an energy deposition in the $n+$ region is subject to slower charge drift due to weaker electric fields [72]. Events that occur far from the $p+$ point contact will also have slower initial rises. Events with depositions very near the point contact will have fast initial rises and will be slower near the maximum of the waveform. These features are also shown in Figure 2.10.

There are many effective pulse shape discrimination (PSD) tools that allow us to tag events with meaningful waveform characteristics. Many of theses PSD parameters were extensively considered by Majorana Demonstrator and GERDA and even well before those experiments. One key PSD parameter to note here is A/E.

A/E is a very effective discriminator for multiple different types of background signals. We often plot our waveforms as the charge induced over time. The derivative of this would be the current of the signal. We take A to be the maximum value of this current (averaged over some number of waveform samples). This maximum current value scaled by the event's energy gives us useful information about the type of event. Again referring to Figure 2.10, we can see how much the current pulse can differ from a hypothetic $0\nu\beta\beta$ event if it is a surface or multi-site event. We can set a low A/E cut to remove slower surface and multi-site events and a high A/E cut to remove faster near $p+$ events like alphas. A plot of A/E vs. energy for the first LEGEND dataset is shown in Figure 2.11.

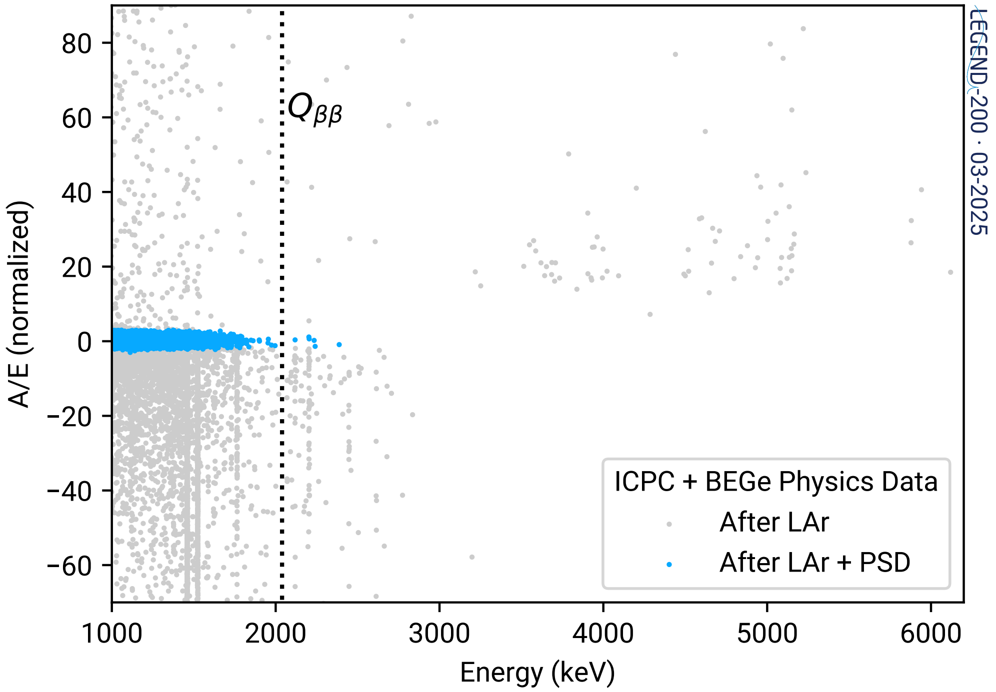

Figure 2.11: A/E distribution from LEGEND-200 physics data after LAr cut and before/after A/E cut. Many events have high or low A/E that will not look like $0\nu\beta\beta$. *Image credit to LEGEND Collaboration.*

Surface backgrounds are a unique source of background in the LEGEND analysis. Charge collection near detector surfaces is known to exhibit some energy-degrading behavior. This could be due to charge build-up on detector and nearby surfaces and will affect not only charge collection but also pulse shape discrimination efficacy. We will study this extensively in Sections 4 and 5. First, in Section 3, we will consider an interesting set of potential signals in L1000 from astrophysical neutrinos.

Chapter 3

Astrophysical Neutrinos

Neutrinos from astrophysical sources make up a significant portion of the neutrinos incident on the Earth's surface. These astrophysical neutrinos can interact with isotopes present in LEGEND—specifically, germanium and argon—and produce background signals in LEGEND-1000 data. Some of these astrophysical neutrino sources are potential background signals in L1000, and some of them are interesting physics signals. These signals will be studied in detail here.

There are four major external neutrino interactions in LEGEND that have been considered: neutrino-electron elastic scattering, inverse beta decay, charged current neutrino-nucleus scattering, and coherent elastic neutrino-nucleus scattering.

3.1 External Neutrino Interactions

3.1.1 Neutrino-Electron Elastic Scattering

Neutrino-electron elastic scattering (νeES) is described by the Weinberg-Salam theory of electroweak interactions and can proceed via the neutral current (NC) and charged current (CC) channels. The differential cross section for this process [73] is written in Equation (3.1)

$$\frac{d\sigma}{dT_e} = \frac{G_F^2 m_e}{2\pi}\left[(g_V + g_A)^2 + (g_V - g_A)^2\left(1 - \frac{T_e}{E_\nu}\right)^2 + \left(g_A^2 - g_V^2\right)\left(\frac{m_e T_e}{E_\nu^2}\right)\right], \tag{3.1}$$

where $\frac{d\sigma}{dT_e}$ is a function of the incident neutrino energy (E_ν) and the recoil energy of the scattered electron (T_e) as well as the vector and axial-vector coupling constants g_V and g_A. There are two main radiative corrections to this cross section stemming from QED and electroweak theory but they are not considered here—this is a sub-3% correction to the cross section for low-energy (5-10 MeV) neutrinos [41]. This νeES interaction is of relevance to larger-scale $0\nu\beta\beta$ experiments as it can become an important source of background, particularly near the $Q_{\beta\beta}$ value for some isotopes.

We can determine the resulting electron recoil spectrum from νeES following Equation (3.2)

$$\frac{dN}{dT_e} = N_e \int \varepsilon(T_e) \left(\frac{d\sigma(E_\nu)}{dT_e}\right) \left[P_{\mathrm{surv}}(E_\nu)\frac{d\Phi_\nu}{dE_\nu}\right] dE_\nu, \tag{3.2}$$

where N_e, $\varepsilon(T_e)$, $P_{\mathrm{surv}}(E_\nu)$, and $\frac{d\Phi_\nu}{dE_\nu}$ represent the electron density of the source isotope, the energy-dependent efficiency of the detector (assumed to be a constant 100% throughout this analysis), the oscillatory survival probability of the emitted neutrino, and the differential neutrino flux, respectively. These electronic recoils will lead to ionization in LEGEND's germanium detectors, liquid argon (LAr) veto system, and muon veto water tank.

3.1.2 Inverse Beta Decay

Inverse beta decay (IBD) is a charged current interaction in which an electron antineutrino scatters off a proton, producing a neutron and a positron. In this interaction, $\overline{\nu_e} + p \to n + e^+$, signals can be generated from a prompt annihilation of the emitted positron and a delayed capture of the emitted neutron. The cross section is simplified when only considering the vector and axial vector components and is a reasonable approximation up to energies of $\sim$ 10 MeV. We write the cross section in Equation (3.3) as

$$\sigma = \frac{G_F^2 p_e E_e}{\pi} \left|V_{ud}\right|^2 \left(g_V^2 + 3g_A^2\right) \tag{3.3}$$

where G_F, $p_e(E_e)$, and V_{ud} are the Fermi constant, the momentum (total energy) of the outgoing electron, and the up-down quark transition amplitude from the CKM matrix (taken from [35]). In this study, we consider IBD events from electron antineutrinos interacting in the 980 m^3 muon veto water tank.

3.1.3 Charged Current Neutrino-Nucleus Scattering

The process of charged current neutrino-nucleus scattering (νNCC) produces more complicated signals in germanium and argon as compared to νeES and IBD and is the preferred method to detect low-energy ($E_\nu \lesssim 50$ MeV) electron neutrinos due to its typically larger cross section [74]. These reactions, $\nu_e + {}^{\mathrm{A}}_{\mathrm{Z}}\mathrm{X} \to {}^{\mathrm{A}}_{\mathrm{Z+1}}\mathrm{Y} + e^-$ and $\overline{\nu}_e + {}^{\mathrm{A}}_{\mathrm{Z}}\mathrm{X} \to {}^{\mathrm{A}}_{\mathrm{Z-1}}\mathrm{Y} + e^+$, have the potential to produce a number of interesting physics events that, if properly tagged in analyses, could provide useful information about neutrinos interacting in the LEGEND experiment. This allows LEGEND to study νNCC scatters on both ^{76}Ge and ^{40}Ar nuclei due to the emitted β particles as well as any prompt relaxation gammas from transitions to excited nuclear states. Additionally, β decays of resulting unstable nuclei such as ^{76}As and ^{40}K are possible, as is spallation of nuclear fragments from higher energy neutrinos. These will primarily be neutrons which can capture on nuclei and produce taggable signals in data [75].

The cross section of these νNCC processes stems from Fermi's theory of beta decay and can be written in Equation (3.4) as

$$\sigma_k = \frac{G_F^2 \cos^2\theta_W}{\pi} p_e E_e F(Z \pm 1, E_e) \left[B(F)_k + \left(\frac{g_A}{g_V} \right)^2 B(GT)_k \right], \tag{3.4}$$

where θ_W, $F(Z \pm 1, E_e)$, and $B(F)_k(B(GT)_k)$ are the Weinberg angle, the Fermi function of the ${}^{\mathrm{A}}_{\mathrm{Z}\pm1}$Y nucleus, and the Fermi (Gamow-Teller) strength function for the transition to the k^{th} excited state of the ${}^{\mathrm{A}}_{\mathrm{Z}\pm1}$Y nucleus. For this study the Fermi function was calculated according to the methods shown in [76] and the Fermi and Gamow-Teller strength functions for ^{76}Ge were taken from [77] and [78] (which provides theoretical strength functions calculated via deformed proton-neutron QRPA from the continuum region of excited ^{76}As states) and for ^{40}Ar from [79] and [80], via the MARLEY simulation package [81] [82]. Analysis of antineutrino scatters was not performed due to the lack of relevant nuclear structure data for relevant isotopes, but these antimatter rates are expected to be comparable to their matter counterparts. The total event rate expected in LEGEND-1000 for neutrino captures on an isotope with mass m can then be found using Equation(3.5)

$$R = \left(\frac{\varepsilon}{m} \right) \sum_k \int \sigma_k \left(P_{\mathrm{surv}}(E_\nu) \frac{d\Phi_\nu}{dE_\nu} \right) dE_\nu, \tag{3.5}$$

where we integrate the (oscillated) neutrino flux weighted by the total cross section over all neutrino energies and then sum over all possible excited nuclear states.

The neutrino-induced νNCC interaction $\nu_e + {}^{76}_{32}\mathrm{Ge} \rightarrow {}^{76}_{33}\mathrm{As} + e^-$ produces an ^{76}As nucleus and an electron, analogous to the electron produced in inverse beta decay (IBD). The angular momenta and parity of the ground state of ^{76}Ge is $J^\pi = 0^+$ and of ^{76}As is $J^\pi = 2^-$. This makes the transition from ^{76}Ge to ^{76}As a first-forbidden Gamow-Teller transition which we can consider to have a negligible transition rate. Thus, we need only consider the interactions that bring ^{76}As to an excited nuclear state.

We expect a number of signatures from this interaction in LEGEND; these signals are summarized below:

- IBD electrons will be emitted due to the interaction
- ^{76}As will be left in an excited nuclear state after the interaction
  - If the energy of the neutrino is sufficiently larger than the neutron separation energy for ^{76}As ($S_n = 7.33$ MeV), ^{76}As may lose a neutron and become ^{75}As, a stable isotope; this ejected neutron can capture in the detector and produce γs and βs which has been studied in GERDA [75]. Higher-energy neutrinos can also cause spallation of protons and heavier nuclei.
  - If the above process does not occur, ^{76}As will emit prompt gamma rays while it de-excites to the ground state. Following this, ^{76}As will beta decay with a half-life of 1.09 days to either an excited state (giving more prompt gammas) or ground state of ^{76}Se, which is stable.

The long half-life of the ^{76}As beta decay makes it more difficult to determine these events as stemming from solar neutrino captures but this determination may be possible through the use of a time correlation analysis [83].

3.1.4 Coherent Elastic Neutrino-Nucleus Scattering

The interaction with the largest cross section among the three studied here is coherent elastic neutrino-nucleus scattering (CEνNS). CEνNS was first detected by the COHERENT experiment [84] and serves as a useful detection channel for low background, low energy-threshold experiments subject to high flux neutrino sources. The differential cross section of this neutral current process can be approximated in Equation (3.6) as

$$\frac{d\sigma}{dT_N} = \frac{G_F^2 M_N}{4\pi}\left(1 - \frac{M_N T_N}{2E_\nu^2}\right) Q_W^2 F_W^2(Q), \tag{3.6}$$

where T_N, M_N, E_ν, Q_W, F_W, and Q are the nuclear recoil energy, nuclear mass, initial neutrino energy, weak nuclear charge, weak form factor, and momentum transfer, respectively. The weak form factor for ^{76}Ge used in this analysis comes from theoretical calculations in [85] and for ^{40}Ar in [86]. This differential cross section can be folded in with the neutrino flux in a similar manner to the νeNS calculation above, with one exception. There is a quenching factor associated with converting nuclear recoil equivalent energies to the readout energy of LEGEND, electron equivalent energies. Quenching factors were taken from the literature for ^{76}Ge [87] and ^{40}Ar [88] and are extensions of the work done by Lindhard [89] and Mei [90].

The low energy nuclear recoils that serve as the signature for the CEνNS interaction can ionize in germanium detectors and the LAr veto system and give us physics signals provided there are events above the data acquisition energy threshold. This CEνNS analysis quotes two germanium experiment energy thresholds: the CDEX dark matter experiment energy threshold of $E_{\text{thres}} = 0.16$ keV [91] and the MAJORANA DEMONSTRATOR energy threshold of $E_{\text{thres}} = 1$ keV [92]. The energy threshold of L200 (as of the writing of this thesis) is ~ 50 keV, but efforts are underway to push it below 10 keV. The goal is to go lower in energy threshold in L1000.

Each of these external neutrino interactions can tell us about some incident neutrino flux given high enough fluxes. In this study we investigate three astrophysical neutrino sources: solar neutrinos, supernova neutrinos, and presupernova neutrinos.

3.2 Sources of Astrophysical Neutrinos and LEGEND's Projected Sensitivity

We can perform calculations to estimate LEGEND's signal rate from astrophysical neutrino interactions. As a comparison point, we use a preliminary low energy background model for LEGEND-1000 [93]. This background model assumes the use of underground argon to reduce backgrounds from ^{39}Ar. The background in the low energy region is still dominated by ^{39}Ar, as well as tritium and the $2\nu\beta\beta$ spectrum.

All calculations in this section assume 100% detector efficiencies. This is a big assumption and will change based on detector, event energy, interaction type, deposition location, etc. This assuption allows for easier comparisons between rates.

3.2.1 Solar Neutrinos

Solar neutrinos, generated in the sun through various fusion processes, are the most common neutrinos incident on the surface of the Earth, and a potential background signal for L1000. The expected solar neutrino flux spectra incident on Earth [94] are shown in Figure 3.1.

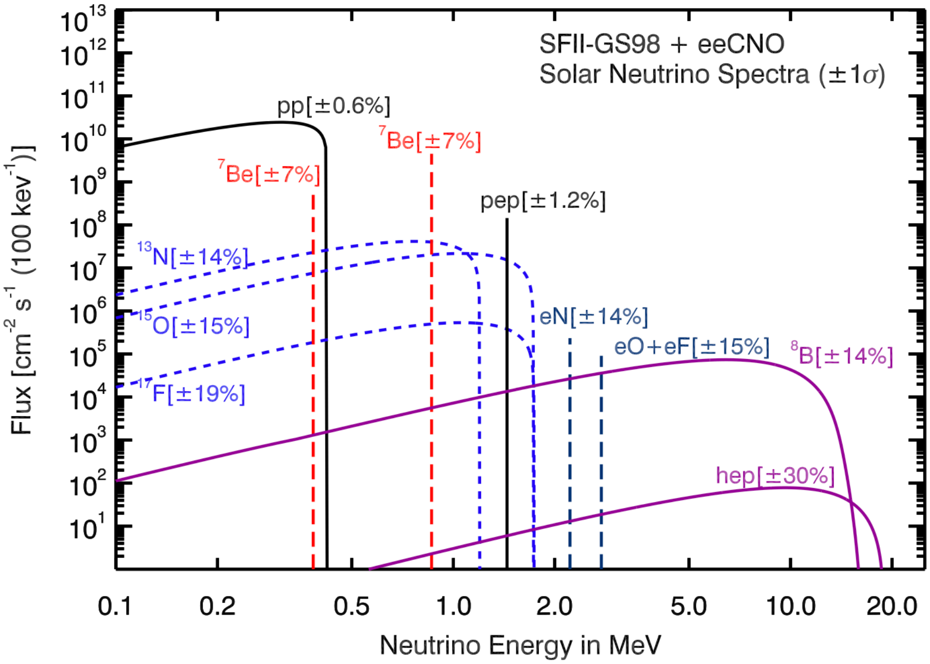

Figure 3.1: Emitted solar neutrino flux spectra as predicted by the Standard Solar Model. Figure taken from [94].

The largest contribution to this flux comes from the proton-proton chain at low energies and ^{8}B interactions at higher energies. Interactions with *pp* neutrinos can serve as a low energy background and incident ^{8}B neutrinos give background signals across the energy spectrum, of which the region around $Q_{\beta\beta} = 2039$ keV is of particular interest to LEGEND. These fluxes are scaled by the survival probability—taking into account MSW matter effects [95, 96]—and necessary constants.

Given these solar neutrino fluxes from Figure 3.1 we can determine the expected spectra of νeES and CEνNS interactions with ^{76}Ge and ^{40}Ar, shown in Figure 3.2, along with the expected total event rate of νNCC interactions.

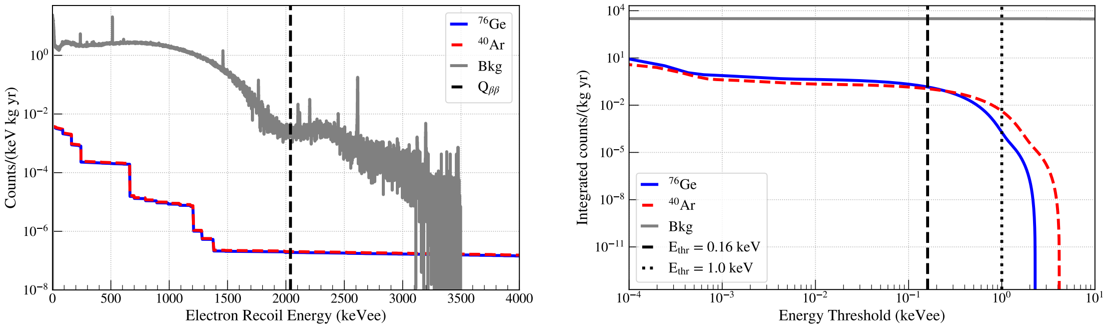

Figure 3.2: Left: Electron recoil spectrum of solar neutrino-electron elastic scattering events on ^{76}Ge and ^{40}Ar compared to estimated Ge background. Right: Energy-integrated nuclear recoil rate of coherent elastic solar neutrino-nucleus scattering on ^{76}Ge and ^{40}Ar as a function of energy threshold.

We see similar electron recoil spectra from neutrinos scattering off ^{76}Ge and ^{40}Ar electrons with an excess of low energy events (primarily from $p-p$ neutrinos) and a background rate in the ^{76}Ge region of interest (ROI) of $\sim 2 \times 10^{-7}$ cts/(keV kg yr), about 2% of the projected rate in LEGEND-1000, $\sim 1 \times 10^{-5}$ cts/(keV kg yr). The signal in the ROI is largely dominated by ^{8}B neutrinos. These electronic recoils will be a subdominant background across a large portion of the energy spectrum.

Nuclear recoils from solar neutrinos incident on ^{76}Ge and ^{40}Ar nuclei via the CEνNS channel will provide a larger signal as compared to νeES—particularly in the low energy region—but still suppressed compared to other backgrounds. Integrating above the CDEX energy threshold of 0.16 keV, we expect a rate of 0.143 cts/(kg yr) in ^{76}Ge and 0.112 cts/(kg yr) in ^{40}Ar. Integrating above the Majorana energy threshold of 1 keV, we find event rates of 1.93×10^{-4} cts/(kg yr) and 4.24×10^{-3} cts/(kg yr) for Ge and Ar, respectively.

In addition to electron and nuclear recoils, we have calculated the total event rate across all energies from solar neutrino νNCC. These events are dominated by ^{8}B neutrinos. Previous calculations [97] [98] for targe isotope ^{76}Ge match our calculated event rate of $R \approx 1.5$ events/(ton-year) for Gamow-Teller transitions to excited states with energy $E_x < 5$ MeV and Fermi transitions to the isobaric analog state (IAS) ^{75}As, comparable to the total event rate of νeES from ^{8}B neutrinos. Including higher excitation levels in the analysis brings this event rate to $R \approx 2.0$ events/(ton-year). For target isotope ^{40}Ar we calculate an expected rate of 2.3 cts/(ton yr), confirmed by MARLEY simulations. These rates are completely negligible across the entire energy range of LEGEND (although we do expect a number of interesting physics signals from each event). Other experiments (for instance, large natural xenon time projection chambers like XLZD) are much more susceptible to solar neutrino backgrounds.

3.2.2 Supernova Neutrinos

Supernova neutrinos (SN), neutrinos emitted during a core-collapse supernova of a massive star, have only been directly detected once before, from the type II supernova SN1987A [99, 100, 101]. In the years following, neutrino detectors have become significantly more sensitive to these large neutrino bursts from cosmic events and even more sensitive detectors are in the construction stages [102]. LEGEND-1000 is well-positioned among ton-scale experiments to detect neutrinos emitted from astrophysical sources like core-collapse supernovae. This is an interesting physics signal and not a background signal—a potential background signal from the Diffuse Supernova Neutrino Background (DSNB) is negligible and not considered here.

Among the stellar candidates close enough to Earth to detect these SN is Betelgeuse, a red supergiant with a mass of $\sim 17\ M_\odot$ and a distance of ~ 170 pc from the Earth. This analysis utilizes simulated SN flux data from Nakazato *et. al* [103], evaluated for a star with mass $m = 20\ M_\odot$ at a distance $d = 200$ pc from Earth. This flux, integrated over the 20 seconds following core-collapse, is shown in Figure 3.3. The spectra of expected νeES and CEνNS events from SN are shown in Figure 3.4.

The electron recoil spectra shown in Figure 3.4 gives a total event rate of ~ 25 cts/(ton burst) for both ^{76}Ge and ^{40}Ar. Crucially, this is an event rate integrated over 20 seconds, and thus could provide a statistically significant signal, particularly above an energy of approximately 1 MeV.

CEνNS interactions from incident SN are expected to have rates high enough to detect in LEGEND-1000. Across the full energy spectrum, we calculate total event rates (in units of cts/(kg

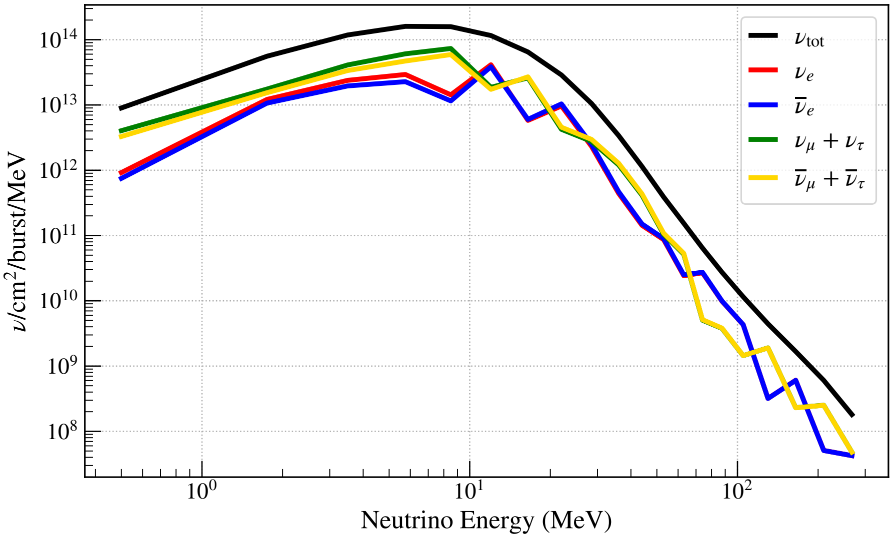

Figure 3.3: Neutrino flux simulations of a supernova with progenitor of mass $20M_\odot$ at a distance of 200 pc from Earth, taken from [103].

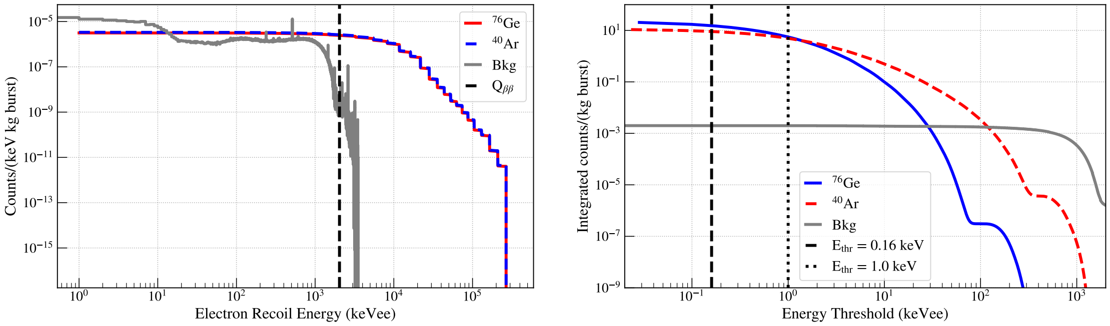

Figure 3.4: Left: Electron recoil spectrum of supernova neutrino-electron elastic scattering events on ^{76}Ge and ^{40}Ar. Right: Energy-integrated nuclear recoil rate of coherent elastic supernova neutrino-nucleus scattering on ^{76}Ge and ^{40}Ar as a function of energy threshold.

burst) and Hz) of 20.39 cts/(kg burst) = 1020 Hz, and 10.76 cts/(kg burst) = 538 Hz for Ge and Ar, respectively. Integrating above the CDEX (Majorana) threshold gives us 14.9 (8.59) cts/(kg burst) = 743 (430) Hz and 8.59 (4.92) cts/(kg burst) = 430 (246) Hz for Ge and Ar, respectively. These numbers assume 100% detection efficiency and are thus expected to be overestimates, but are still significant enough to be considered detectable (the expected rate of events in any one Ge detector in L1000 is < 0.01 Hz). SN CEνNS events will not only provide a statistically significant number of events above LEGEND-1000's expected background events, but it may also cause an increase in the average waveform baseline values due to such an increase of ionization events in germanium detectors.

We also expect a high number of charged current events from SN. LEGEND-1000 will be very sensitive to IBD events in the ~ 1 kton water tank, with event rates of $\sim 5 \times 10^6$ cts/(kton burst) $\sim 2.5 \times 10^6$ Hz, assuming perfect detection efficiency and all events above muon veto PMT thresholds. The LEGEND-200 water tank trigger rate is a few tens of mHz so a simple scaling suggests we expect on the order of 1 event/burst in the L1000 water tank above threshold in a steady state. We certainly do not expect 100% detection efficiency and all SN events to be above threshold but this very large event rate suggests that LEGEND-1000 could be sensitive to supernovae much farther than Betelgeuse, potentially out to a distance of ~ 10 kpc (200 cts/burst = 10 Hz). This will require special work on the readout for the water tank such that this high an event rate would not crash our data acquisition. We expect charged current events in ^{76}Ge and ^{40}Ar as well through the νNCC interaction, with rates of 438 cts/(ton burst) and 274 cts/(ton burst), respectively. This calculation does not include forbidden decays and thus is likely an underestimate of the true rate, again assuming perfect efficiency.

3.2.3 Presupernova Neutrinos

As massive stars evolve towards their imminent collapse, they will produce neutrinos from various processes interior to the star. These presupernova neutrinos (preSN) may serve as a "warning sign" for an impending supernova explosion and can provide valuable information about stars entering the end of their life cycles. For this analysis (in which we consider a star of mass $15M_\odot$ at a distance of 200 pc from Earth), we use preSN fluxes at seven different time points, hours before core-collapse, as calculated by Patton et. al [104]. Those fluxes are shown in Figure 3.5. The resulting preSN νeES and CEνNS spectra are shown in Figure 3.6.

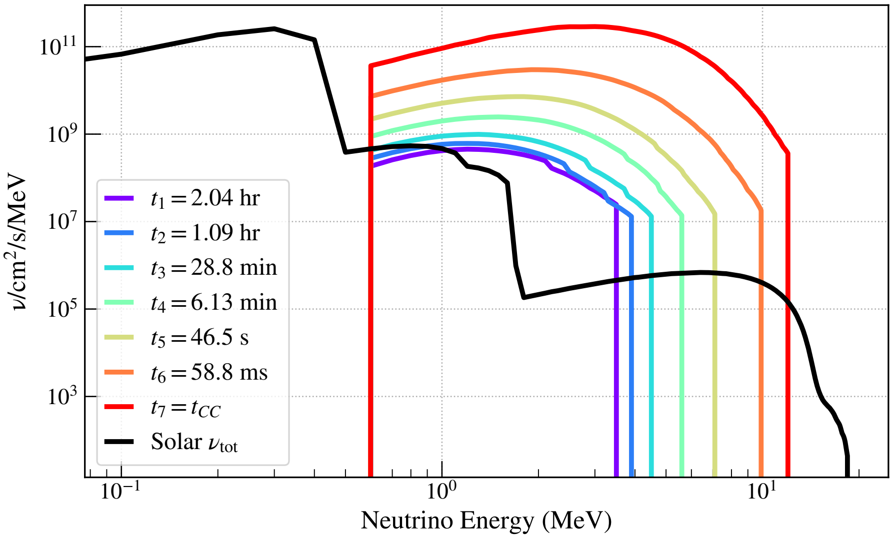

Figure 3.5: Neutrino flux simulations in the hours before a supernova with progenitor of mass $15M_\odot$ at a distance of 200 pc from Earth, taken from [104]. Flux is evaluated at: $t_1 = 2.04$ hrs, $t_2 = 1.09$ hrs, $t_3 = 28.8$ min, $t_4 = 6.13$ min, $t_5 = 46.5$ s, $t_6 = 58.8$ ms, and $t_7 = 0$s. The hard cutoff at lower energies is not physical but from a lack of data.

The preSN νeES electron recoil rates across the energy spectra are expected to be subdominant to other sources of background and are thus not an effective method to detect presupernova neutrinos, unless conditions are optimized to measure high energy events in LEGEND.

The CEνNS integrated nuclear recoil spectra shows counts above our simulated background rate seconds and milliseconds before a supernova, but at energies mostly below 1 keV. For $t_7 = t_{\rm CC}$, the time of core collapse, we expect 1520 cts/(kg yr) and 2025 cts/(kg yr) from scatters above the CDEX energy threshold off ^{76}Ge and ^{40}Ar, respectively. If the LEGEND-1000 energy threshold can be brought closer to this 160 eV threshold, detection of these preSN may be possible, but would be too soon before a supernova event to signal the explosion. Above the MAJORANA energy threshold,

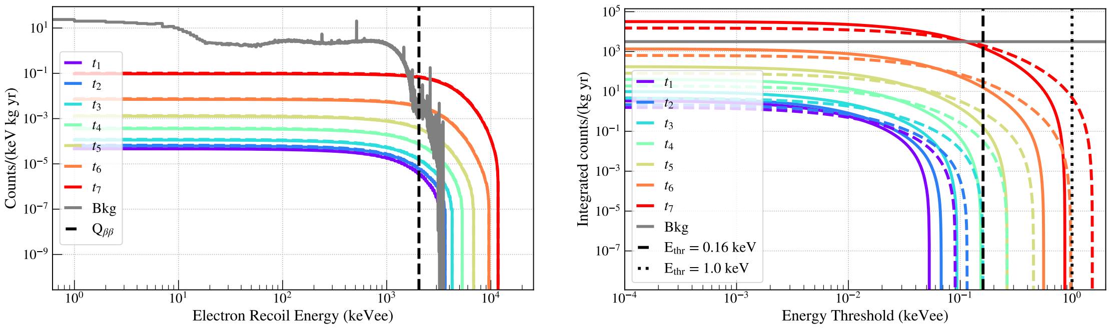

Figure 3.6: Left: Electron recoil spectra of presupernova neutrino-electron elastic scattering events on ^{76}Ge and ^{40}Ar. Right: Energy-integrated nuclear recoil rate of coherent elastic presupernova neutrino-nucleus scattering on ^{76}Ge and ^{40}Ar as a function of energy threshold.

we expect no events in germanium and 4.84 cts/(kg yr) in argon. IBD is also a potential preSN detection channel, with an event rate of ~ 0.24 Hz at the time of core collapse. This will likely be too weak of a signal to detect in real time when considering detection efficiency and threshold but these events could produce a higher event rate than the estimated 0.06 Hz "background" rate in the water tank. Lowering the muon veto threshold will have an impact and can be studied further.

Overall, this study indicates that LEGEND-1000 has the sensitivity to detect neutrinos emitted from a supernova at a sufficiently close distance. These neutrinos could be detected from all four interactions studied; neutrino-electron elastic scattering, inverse beta decay, charged current neutrino-nucleus scattering, and coherent elastic neutrino-nucleus scattering. This ability to detect in all four channels and with multiple different isotopes/materials places LEGEND in a unique position among potential supernova neutrino detectors. These event rates may also be high enough to do interesting analyses of the nature of these neutrinos, such as studying matter effects of neutrino oscillations and a theorized neutrino-antineutrino asymmetry [105].

Presupernova neutrinos will also produce signals in LEGEND-1000's germanium detectors, liquid argon veto system, and muon veto water tank, but without an energy threshold approaching the lowest achieved among direct dark matter detection experiments such as CDEX, it is unlikely that these neutrinos will provide enough counts to study in further detail. With that being said, LEGEND-1000 is well positioned to look for these events among ton-scale experiments due to its multiple interacting isotopes and large water tank.

Chapter 4

KrSTC Data

The Krypton String Test Cryostat (KrSTC) aims to study low energy photon and electron energy degradation in PPC detectors.

4.1 Motivation

As discussed in [106], the MAJORANA DEMONSTRATOR (MJD) sees background alpha particles in a wide energy range. This is seen in the final MAJORANA DEMONSTRATOR energy spectrum, shown in Figure 4.1

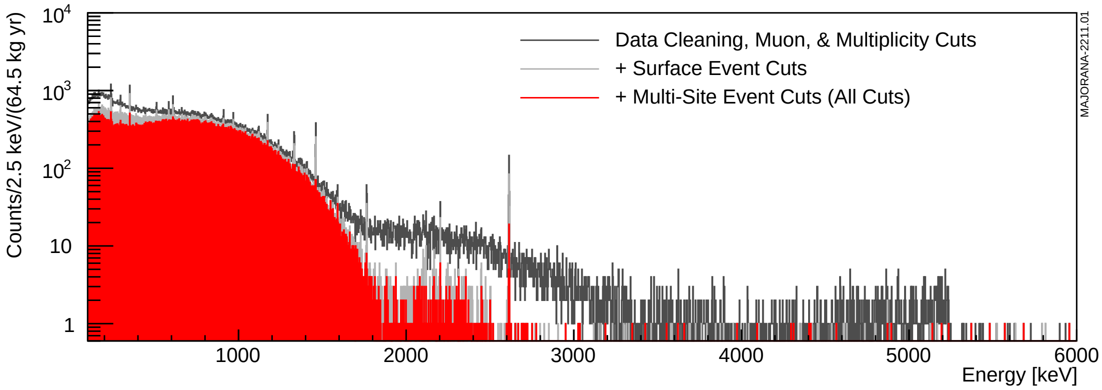

Figure 4.1: MAJORANA DEMONSTRATOR final full energy spectrum from [59]. Surface event and multi-site events cut many presumed alphas at high energy, but some remain at low energy near $Q_{\beta\beta}$.

These alphas are hypothesized to come from ^{210}Po decays, with the ^{210}Po coming from the ^{238}U decay chain—specifically, it is thought that there is ^{222}Rn plate-out on plastic surfaces near the

HPGe detectors. Those plastic surfaces are spacers at the $n+$/passivated surface interface and a contact pin bushing in the $p+$ point contact. In the MAJORANA DEMONSTRATOR spectrum before cuts, there are some counts up to 5.3 MeV [107], which is consistent with these ^{210}Po alphas. Some alphas are also seen to be degraded in energy, with a roughly Gaussian distribution centered near $Q_{\beta\beta}$. Luckily, these backgrounds can be tagged and removed quite efficiently with pulse shape discrimination techniques.

The primary analysis cut developed to deal with these so-called "surface alphas" is known as delayed charge recovery, or DCR [108] [106]. Alphas are expected to be fully stopped and energy degraded in the $\mathcal{O}(1\text{ mm})$-thick $n+$ transition region (these alphas penetrate $\sim 20\ \mu$m in germanium, see Figure 4.2). Thus, surface alphas are thought to be localized to the passivated surface and $p+$ point contact regions. Ionizing radiation depositing energy very near to this passivated surface is believed to be energy degraded due to a reduction in charge mobility along the amorphous germanium passivated surface. The model for this degradation involves surface charge collecting on the large insulating passivated surface of a PPC detector. After ionization, if holes (electrons) drift towards a negative (positive) surface charge, they can get briefly trapped at the surface and re-released on waveform digitization timescales. This shows up as a slightly positive slope on a pole-zero-corrected waveform. This slope is the eponymous DCR, as this delayed charge is recovered towards the end of the event. An illustration of DCR in alpha waveforms is shown in Figure 4.3

DCR will cut degraded alphas (as the mechanism it targets is this charge re-release at the passivated surface). This we can see in Figure 4.4. DCR starts cutting significant events slightly below the 5.3 MeV alpha line as those alphas start to be degraded, with hundreds of keV of energy lost in the tail of the waveform. We expect alphas that are not energy degraded to be very near the $p+$ point contact since they cannot penetrate the $n+$ transition region. Therefore we also apply an $AvsE$ cut (similar to A/E discussed in Section 2.4.2). If we look at Figure 4.4, we see that a high $AvsE$ cut (which would tag a quick-rising event) cuts a lot of events in the 2-3 MeV energy range. Confusingly, this high $AvsE$ cut does not tag these undegraded alphas like we expect. It is possible that such a high energy event creates a charge cloud large enough and subject to enough diffusion, self-repulsion, distortion, etc. that the quick risetime information is smeared out and not successfully tagged, but this behavior is not well understood.

All of this physics arises due to the small penetration depths of these alpha particles. In that

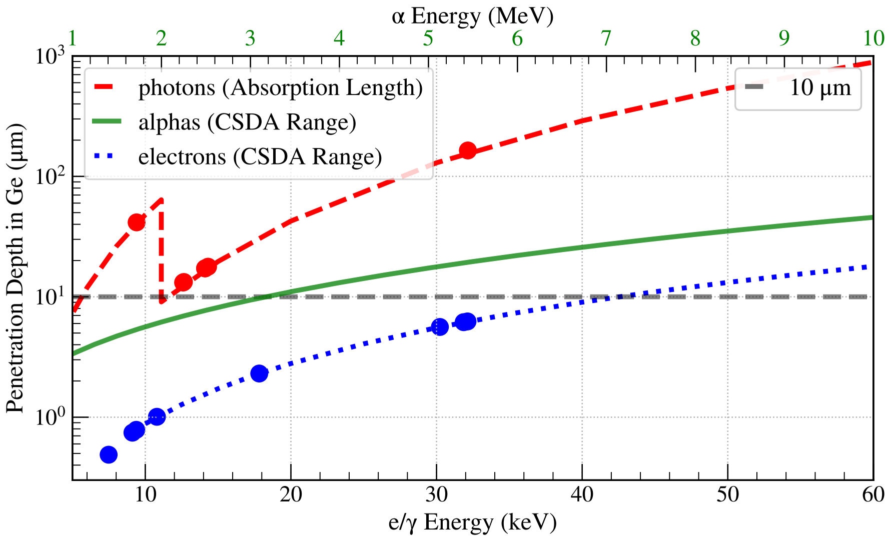

Figure 4.2: Penetration depths of low energy electrons and photons and high energy alphas. Specific points on plot represent $^{83\text{m}}$Kr decay products. Data from XCOM [109], ESTAR [110], and ASTAR [111].

vein, we also expect low-energy photons and electrons to be susceptible to this energy degradation. If we look at the MAJORANA DEMONSTRATOR low-energy spectrum in Figure 4.5, we see evidence of this.

Both the enriched and natural detectors clearly see this 46.5 keV γ line from ^{210}Pb (which also comes from the ^{222}Rn decay chain, with an intensity of 4.25% and an absorption length in germanium of 452 μm. This is unsurprising, as this photon should punch through any dead layer in a way that an alpha could not. Similarly, we see no peaks associated with the 42.5 keV and 30.2 keV conversion electrons from ^{210}Pb, as their CSDA ranges are 10.0 μm and 5.6 μm, respectively. In the natural detector spectrum, we don't have much else to learn below $\sim$ 19 keV as tritium beta decays start to dominate. However, the enriched detectors show significantly less tritium contamination. A gamma line—technically multiple overlapping lines—from the cosmogenically activated ^{68}Ge appears at $\sim$ 10.3 keV in the enriched spectrum but sits atop a much smaller tritium spectrum. A

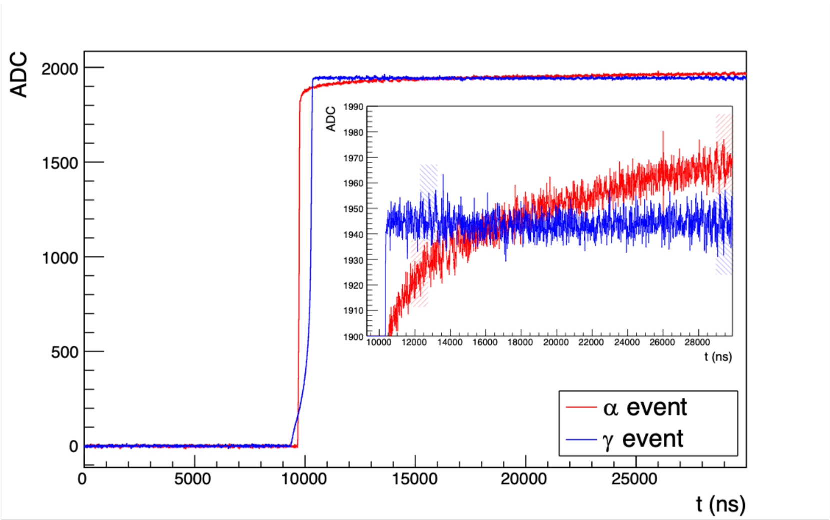

Figure 4.3: Delayed charge recovery (DCR) of an alpha event vs. a bulk gamma event from [112]

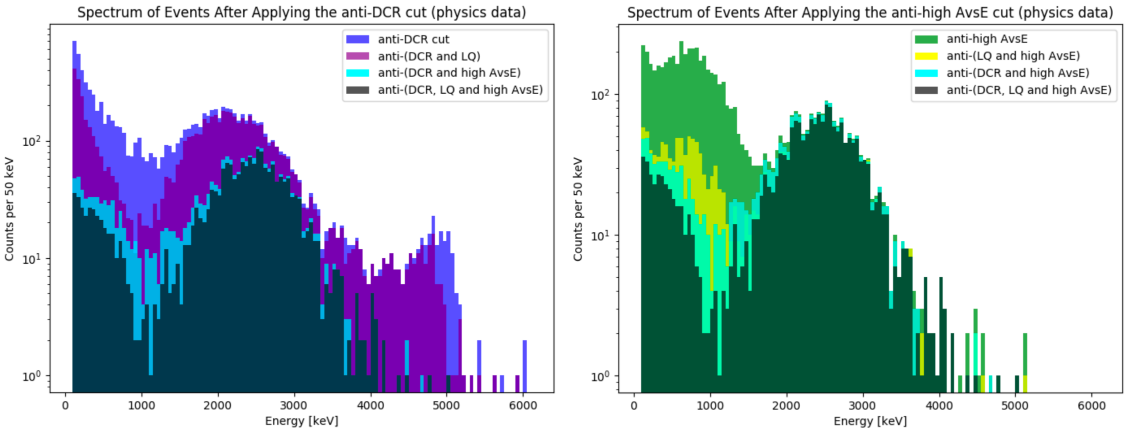

Figure 4.4: DCR (left) and *AvsE* (right) cuts on Majorana Demonstrator data from [106].

peak search from [92] shows no evidence of a 10.8 keV γ, which is another decay product of ^{210}Pb. This gamma has an intensity of 22.7% and an absorption depth of $\sim$ 59.6 μm, much larger than that of the alphas—the CSDA range of the 5.3 MeV alphas is 18.7 μm—or low-energy electrons, yet it appears to be energy degraded. The goal of KrSTC is to study the nature of this partially

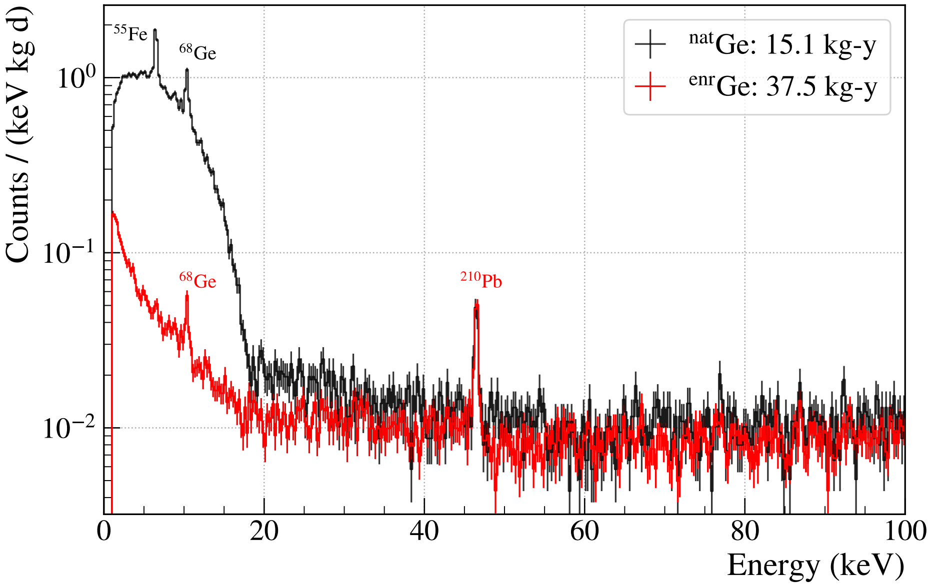

Figure 4.5: Majorana Demonstrator low energy spectrum from [92]. Only one photon line from ^{210}Pb is visible, suggesting some energy degradation of shallowly penetrating particles.

inactive region near the passivated surface and understand exactly how these alphas and low energy photons and electrons are being energy degraded.

4.2 Experimental Setup

4.2.1 OPPI

The detector used in KrSTC is the ORTEC Prototype PPC Investigation (OPPI). It is a p-type point contact (PPC) high purity germanium detector modeled in Figure 2.8. The detector was previously used in the CAGE test stand at the University of Washington to study surface alphas [113] [114] [115].

The true detector dimensions are not precisely known and those dimensions are critical simulation inputs as will be discussed later. These detectors are quite sensitive, especially the passivated surface, so conventional measuring techniques are not feasible. Measurement of these dimensions is relevant for simulation work and will be discussed in 5.1.1. An image of OPPI and its detector hardware is shown in Figure 4.6.

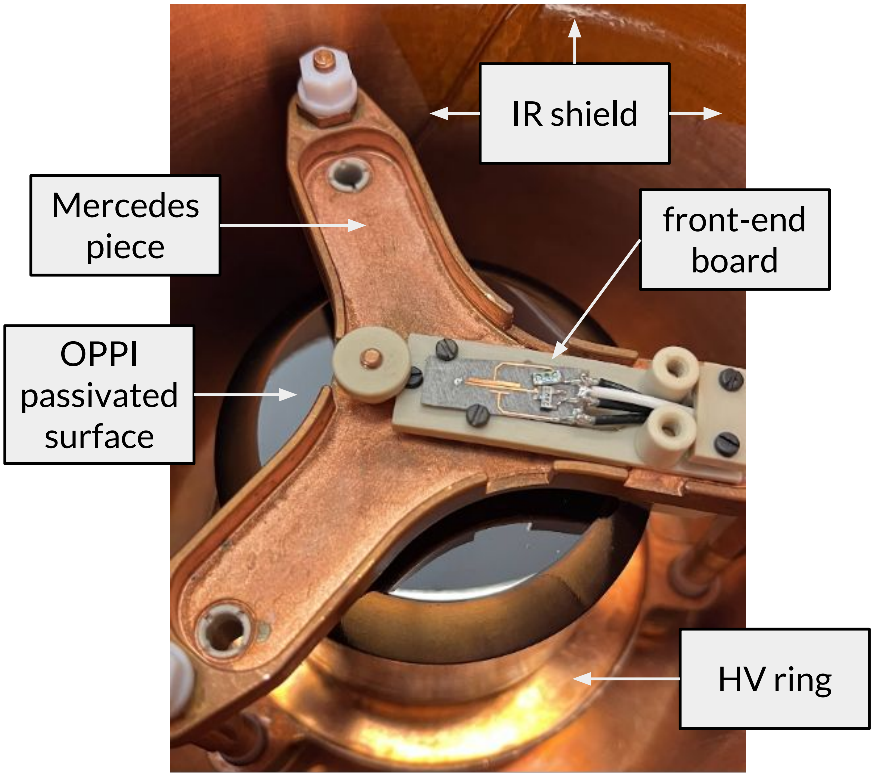

Figure 4.6: OPPI detector with mounting hardware from Majorana Demonstrator. Not seen here are the contact pin and point contact (underneath the left side of the front-end board) and the PTFE spacers (at the ends of the three Mercedes piece prongs)

.

4.2.2 Other Detector Hardware

The hardware used to deploy OPPI in our cryostat is from Majorana Demonstrator. It consists of a copper three-pronged "Mercedes piece" on which sits a PEEK "diving board". This diving board holds the front end electronics above the detector, and the diving board is flexed downward by a PEEK screw piece such that the contact pin soldered on the underside of the front end board can make good contact inside the $p+$ point contact. There are also copper rods and PTFE spacers on each prong of the Mercedes piece in part to provide a good electrical contact between OPPI and the high voltage ring piece, where we apply a bias voltage to the $n+$ surface of the detector. This all sits on an electrically insulated base piece of copper and is covered by a copper can used as an infrared radiation (IR) shield to protect the detector from blackbody radiation inside the cryostat. This hardware is shown in Figure 4.6.

The aforementioned cryostat also comes from Majorana Demonstrator, where it was a cryostat used to test the deployment of strings of HPGe detectors (hence the String Test Cryostat in the KrSTC acronym). The cryostat and much of the hardware mentioned in this section is shown in Figure 4.7 It consists of a number of steel flanges as well as an aluminum nipple. That nipple sits on a collar that serves as the interface between the vacuum cryostat and the liquid nitrogen (LN) dewar on which the cryostat sits. The base copper piece of the OPPI holder hardware bolts into a long copper cold finger which extends down into the LN dewar and cools the detector assembly. The cold finger consists of two copper pieces with a flattened ring of indium between them to provide better thermal contact. The cold finger is outfitted with cartridge heaters to provide the ability to perform a "pump and bake" of the detector, warming the detector to $\sim 60°$C and pumping on it to remove any residual material off detector surfaces.

After the detector is deployed inside the cryostat, all the flanges are sealed and the cryostat is pumped on with a Pfeiffer HiCube 80 turbomolecular vacuum pump. The pump consists of two stages; a roughing diaphragm pump to get the pressure down to a base of ~ 10 mbar, and a turbomolecular HiPace 80 that brings the vacuum level down to $\mathcal{O}(10^{-6}$ mbar) after pumping for about one day. This pump required some maintenance of both the roughing and turbo stages; this was all done by us onsite at CENPA with guidance from Pfeiffer. Once the cryostat is sufficiently pumped down, we fill the dewar with liquid nitrogen to cool the detector assembly—this cooling process takes about 16 hours and cools the detector to somewhere around 90 K. This cooling process will also lower the pressure of the cryostat by 1-2 orders of magnitude due to cryopumping of cold surfaces.

On one of the cryostat flanges we connect our $^{83\text{m}}$Kr source, shown in Figure 4.8. This is actually a ^{83}Rb source (half-life of 86 days) [116] adsorbed onto zeolite beads that produces this metastable krypton isotope in gas form, made by the Pacific Northwest National Laboratory (PNNL). This krypton gas can be introduced into the cryostat via two separate Swagelok valves. Typically, this

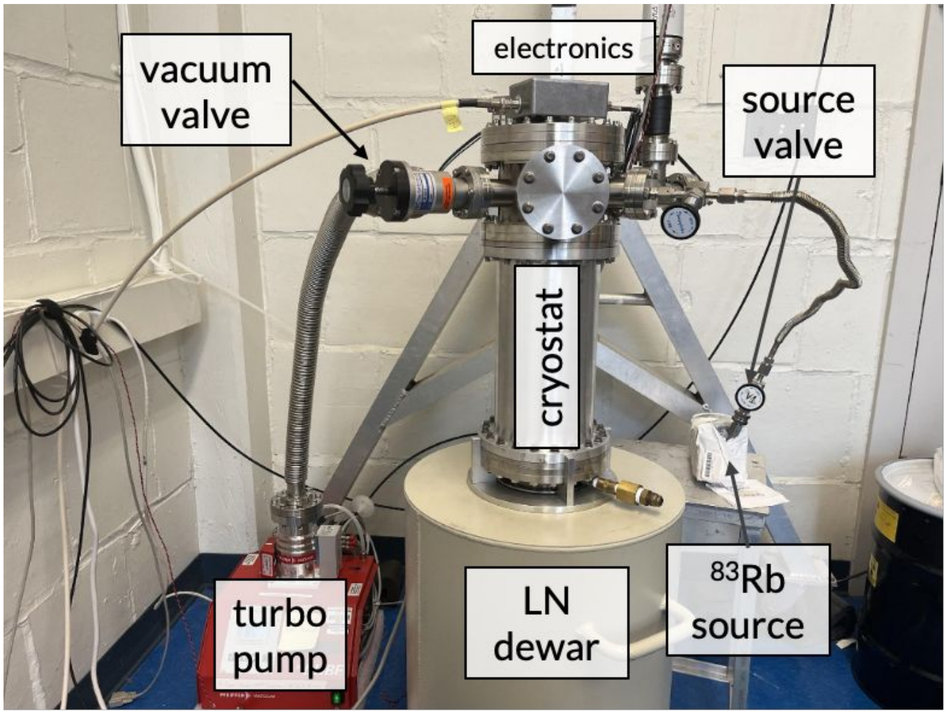

Figure 4.7: KrSTC experimental setup, showing the cryostat, pump, liquid nitrogen dewar, source, electronics, and important cryostat valves.

gas is brought into the cryostat while the vacuum pump is valved off of the system such that the gas is not immediately "captured" by the pump. Rather, the Kr gas can enter the cryostat nipple via diffusion and can decay near the detector with its 1.83 hour half-life. It is possible that the gas could condense onto the cold cryopumping surfaces but there no strong evidence that it strongly adheres to any surfaces, especially to those of the detector. When the krypton-filled cyrostat is exposed to the vacuum pump, the krypton rate drops immediately. The possible decay products of $^{83\mathrm{m}}$Kr is shown in Table 4.1.

Pressure monitoring turns out to be a very important part of this test stand. To do this we attach a Pfeiffer PKR 251 pressure gauge to the cryostat. The PKR 251 has two stages for pressure measurement. The Pirani stage is always switched on and is used for pressures above

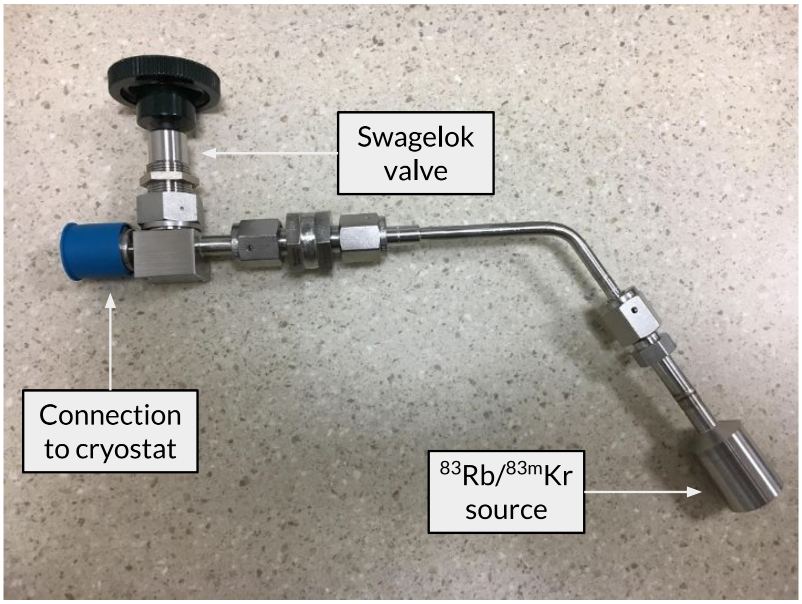

Figure 4.8: ^{83}Rb/$^{83\text{m}}$Kr source, made by PNNL, that connects to our cryostat via VCR. Normally the source is inside a brick of lead to shield the detector from ^{83}Rb photon lines.

$\sim 1 \times 10^{-2}$ mbar. Below this pressure the cold cathode stage activates to measure down to $\sim 5 \times 10^{-9}$ mbar. This gauge would sometimes require cleaning or a full repair and this work was all done on-site.

We also attach to the copper can of the detector assembly a thermally lagged PT-1000 temperature sensor. This does not provide a perfect temperature reading of OPPI due to uncertainties at LN temperatures of these sensors as well as some significant distance between the sensor and the detector surface, but it is a reasonable measurement in particular to determine when the detector is cold enough to operate. Typical temperature readings when cold were between 90-100 K, higher than LN temps of 77 K but a fine temperature at which to operate OPPI (there was some uncertainty in our temperature measurement so OPPI was likely colder but still performed well with temperature readings < 100 K).

The detector must be biased in order to properly collect physics signals. For that, we use a CAEN N1470 high voltage NIM module connected via SHV cable through a cryostat flange to the

Particle	**Energy (keV)**	**Intensity (%)**
Electrons		
Auger L	1.5	168.4
CE L	7.4847	80.0
CE M	9.1177	12.9
CE N	9.3817	1.26
Auger K	10.8	8.62
CE K	17.8260	24.8
CE L	30.2306	63.7
CE M	31.8636	10.66
CE N	32.1276	0.782
Photons		
XR 1	1.59	3.70
γ	9.4057	5.5
XR kα2	12.598	4.70
XR kα1	12.651	9.1
XR kβ3	14.104	0.65
XR kβ1	14.111	1.27
XR kβ2	14.311	0.167
γ	32.1516	0.062

Table 4.1: $^{83\mathrm{m}}$Kr decay products, excluding some very low energy information. ^{83}Rb decays with an 86 day half-life to $^{83\mathrm{m}}$Kr, which decays in two stages with these decay products and a half-life of 1.83 hours. Data from [116].

copper HV ring on which OPPI sits. The nominal operating voltage for OPPI is 2700 V (although that number is subject to change due to changing cryostat conditions, as will be discussed) and the typical depletion voltage was 2200 V. The voltage was ramped up slowly as to not damage the electronics and to avoid any discharges. When the detector showed signs of increased leakage current (a steady drop in baseline), we would revert back to the last voltage set point without that increase in leakage current. This CAEN HV module also feeds into a high voltage filter box (made by CENPA engineers) which filters high frequency noise from the HV input and provides a way to pulse the HV ring with a function generator.

The electronics chain was modeled after the MAJORANA DEMONSTRATOR electronics. As mentioned, a front end board—with a soldered-on contact pogo-pin—is connected via contact pressure to the $p+$ point contact. This front end board, in simple terms, consists of a feedback capacitor $C_f = 0.1$ pF and a feedback resistor $R_f = 10$ GΩ. The voltage difference induced on the point contact due to drifting charge carriers in the detector during physics events leads to a charge across our feedback capacitor. That charge is bled off by the feedback resistor on a timescale $\tau_{RC} = C_f \cdot R_f = 1$ ms. There is also a JFET on the board. The outputs of this front end board are the feedback line, the drain of the FET, and the ground of the FET (which is connected to cryostat ground at the copper can), as well as a pulser input. These outputs are routed through a DB9 connector at the flange and connected to our post-amplification stage which contains a feedback loop with amplification for gain increases. A diagram of the front-end electronics is shown in Figure 4.9.

Many parameters, such as pressure, temperature, baseline, HV set points, etc. are necessary to monitor both during data taking and after during analysis. We use a number of Docker containers to deploy our slow controls system, based off the slow controls of the Project 8 experiment. The core components are a rabbitMQ broker to communicate with Dripline, a postgres database from which Metabase can plot parameters in real time. More recently we have moved to Slowdash [117] for our visualization needs. We also use dragonfly and supervisor for other key communications. These commands are run using a Raspberry Pi in our slow controls box which also connects to our pressure gauge, temperature sensor, LN scale, and baseline monitor. Monitoring these values is a good, if too human, way to spot any problems in our system during data taking. For a more robust check, we use a high voltage interlock run on the Raspberry Pi to make sure no key parameters (pressure, temperature, baseline) exceed unwanted thresholds. If this happens, the Raspberry Pi sends a signal to the HV supply to bias down the detector.

We use a SIS 3302 digitizer for our data acquisition. This digitizer is an 8-channel, 16-bit ADC

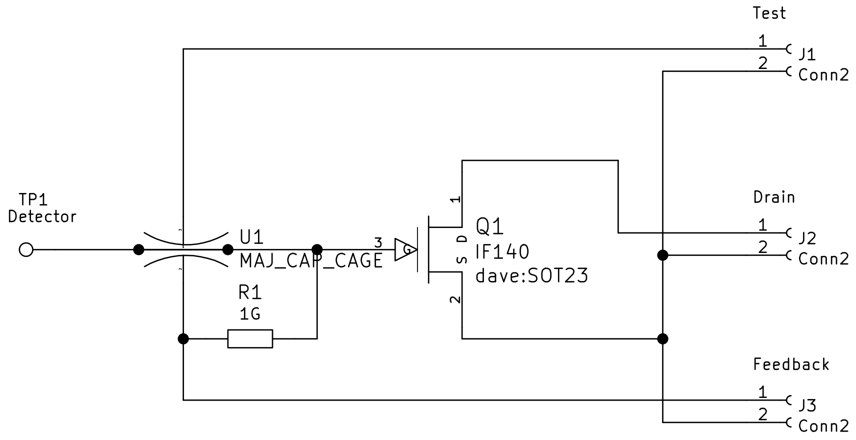

Figure 4.9: KrSTC front-end electronics schematic, from [113]. This is the same front-end as used in that CAGE paper, but during data-taking (and for all KrSTC data shown in this thesis) we switched to a 10 GΩ feedback resistor.

that operates at 100 MHz sampling frequency. This digitizer connects to a single board computer (SBC) for connection to our data acquisition software, ORCA [118]. ORCA (Object-oriented Real-time Control and Acquisition), developed at CENPA and at the University of North Carolina, provides run controls, data monitoring, easy interfacing with hardware, and many more useful tools during the data-taking process.

4.3 Data Taking Procedure

The lowest level KrSTC analysis (and thus, the goal of most data-taking campaigns) is to see a difference in the low-energy spectrum when krypton is introduced into the cryostat. To that end, most campaigns are comprised of mostly background runs and krypton runs. Background runs are any runs in which we do not open the valves to bring krypton into the cryostat. Krypton runs are runs in which we have krypton in the system and have our vacuum pump valved off so it cannot remove the gas from the cryostat. Typically, we would close the vacuum valve, let the pressure settle after the volume change, and start taking background data. Then after enough background events, we would open the krypton valve and start a krypton run. After this, we can just subtract the runtime-corrected background spectrum from the krypton spectrum and proceed with our analysis.

There are other run types we looked at with KrSTC; the most important are decay runs, barium runs, and pulser runs. Decay runs are useful as a check that what we are seeing in the low energy region really is krypton. $^{83\text{m}}$Kr has a 1.83 hour half-life. If we close the krypton valve and leave our vacuum valve closed, we can test to see if the krypton decays away with the expected half-life. Both barium and pulser runs are mostly for calibration purposes. We can use a ^{133}Ba source of activity $\sim 100\mu$Ci outside of the cryostat which gives us lower energy peaks, specifically a gamma at 81 keV [119]. This is useful since there may be energy non-linearities between the low energy Kr region and the higher energy regions from which we calibrate our energy spectrum. Pulser data consists of short runs where we seek to match known energy peaks with a pulser input; these runs were not used much in KrSTC but could be useful in understanding energy non-linearities.

There are other data-taking parameters with which we can play. We have cartridge heaters installed in our copper cold finger so we can bake OPPI to remove any residual condensation on detector surfaces. This was seen to change detector performance, as will be discussed in Section 4.5. This pump and bake consists of baking the detector to $\sim 60°$C and pumping on the system for $\sim$ 1 day. The sign of a successful bake is in the pressure vs. time curve, where the pressure shows an initial increase as gasses are released from the detector surfaces before leveling off and starting to decrease again. Baking the cryostat with heater tape was another option, though that was not often necessary and was scary with the very old heater tape we had. We also attempted baking the Kr source, which consisted of using a band heater borrowed from Project 8 and wrapping it around the capsule containing the zeolite beads. We followed a procedure from PNNL detailing how to properly bake this source. We could keep the vacuum valve open or closed during background runs but did not notice a difference between the two spectra. We could also open the vacuum valve when krypton gas was in the cryostat to see if the krypton was fully gaseous or was stuck to detector surfaces. The energy threshold would change campaign to campaign (and sometimes run to run) due to different noise conditions. The energy threshold in ORCA was selected to keep the maximum low energy information possible without exploding our data rates. Noise was dealt with in a number of ways, most often with aluminum foil and placement of the electronics boxes (post-amp and HV filter) on different parts of the outside of the cryostat, with different pressures applied to them.

4.4 Data Analysis

The current processing framework was developed by the LEGEND group at CENPA (with most of the development done by Clint Wiseman). It consists of a number of JSON config files holding information about the data acquisition, run numbers and types of runs[1], files to skip during processing, optimized DSP parameters, etc.

After data-taking, the binary data acquisition (DAQ) files are transferred to the NERSC cluster for processing and analysis. These DAQ ORCA files are decoded by a python script from the pygama software stack [120] that is used for the LEGEND analysis. Once these DAQ files are decoded they become RAW files, with parameters such as event timestamp, DAQ energy (an energy estimator provided by the DAQ software), and waveform values. This is typically where we get our first look at a campaign's energy spectrum. The DAQ energy value comes from a trapezoidal filter run on the incoming waveforms. The parameters of this trapezoidal filter are roughly optimized to yield optimal energy resolution of the 1460.82 keV ^{40}K gamma peak. Given our low event rate relative to our digitizer sampling rate, dead-time is expected to be negligible and thus runtimes for our background and krypton runs can be calculated by taking the Unix timestamps of the first and last event in a run and subtracting the two. We can then look at our runtime-normalized energy spectra as an initial look at our data.

We also want to use optimized trapezoidal filter parameters on individual runs, as well as look at various waveform parameters. This is done in the conversion from RAW files to DSP (digital signal processing) files. DSP files have a number of outputs and there are other optimizations done during the RAW to DSP conversion that are useful. Those key optimizations are: energy calibration, the pole-zero correction to our raw waveforms, and the optimized trapezoidal filter parameters for energy estimation.

---

[1] The naming hierarchy for our data-taking is: cycle (a single $\sim$ 25 minute data file), run (a group of cycles, separated by changes in data-taking conditions such as moving from background to krypton, opening a cryostat valve, etc.), and campaign (a group of runs, typically consisting of a full thermal cycle of the detector; some campaigns last a few hours, others a few weeks).

4.4.1 Data Cleaning

Doing sophisticated data cleaning is not terribly necessary in KrSTC. Provided noise conditions are relatively stable across a given campaign (and runs with significant noise are flagged and removed from the dataset), we can just apply simple data cleaning. KrSTC mostly looks at background-subtracted data so constant noise sources should be a small and roughly equal population in both background and krypton data. We can apply cuts to the baseline values of our waveforms as well as the slope, y-intercept, and baseline standard deviation. Applying a 1σ cut on each of these parameters for a given run lets us keep $\sim 97\%$ of all events and $\sim 96\%$ of events in krypton region. An example of histogrammed baseline values for one campaign is shown in Figure 4.10.

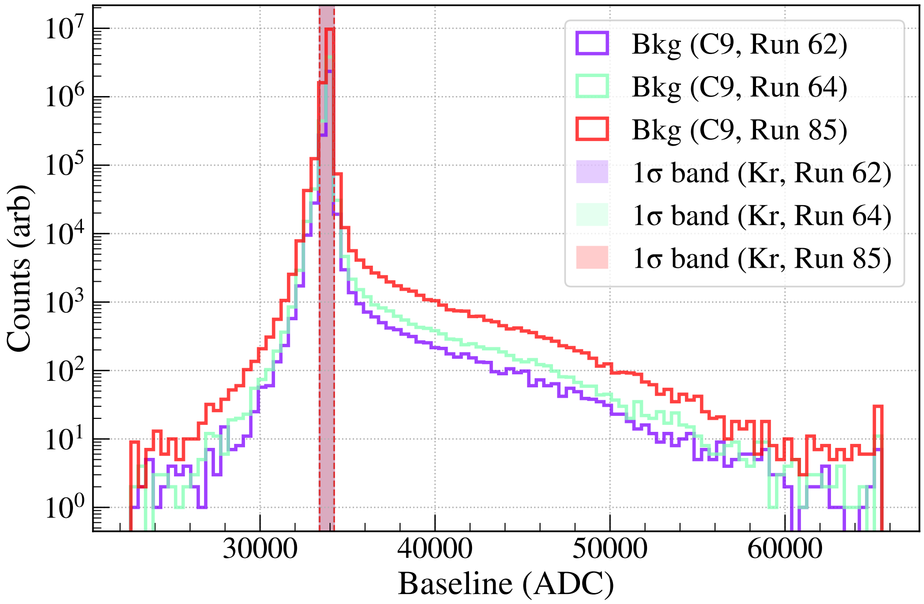

Figure 4.10: KrSTC baseline data cleaning of individual waveform baseline values in multiple krypton data runs. This is a 1σ cut that keeps $\sim 97\%$ of data.

4.4.2 Energy Calibration

An accurate energy calibration is difficult to produce for KrSTC. This is due to nonlinearities in the system, some of which are more easily resolvable than others. Specifically, these energy nonlinearities can distort the calibration parameters such that an energy spectrum that is well calibrated at higher energies ~ 1 MeV can be poorly calibrated in the low energy ~ 10 keV region in which we are interested. Some of our DSP optimizations require a rough calibration which is much simpler. From prior experience we know—barring some unusual noise burst—that our tallest higher energy peak will be the 1460.82 keV gamma line from ^{40}K. We can locate that peak in the uncalibrated energy spectrum (as seen in Figure 4.11 and either take the mode of that peak or fit a gaussian to the top of the peak to find the location μ in DAQ energy (in arbitrary ADC units). From there, we take the ratio $\frac{1460.82 \text{ keV}}{\mu(\text{ADC})}$ and scale all energy values by that ratio to perform a rough, order 0 polynomial calibration. This puts our energy peaks close enough to their true energies in order to use them in our other DSP analyses.

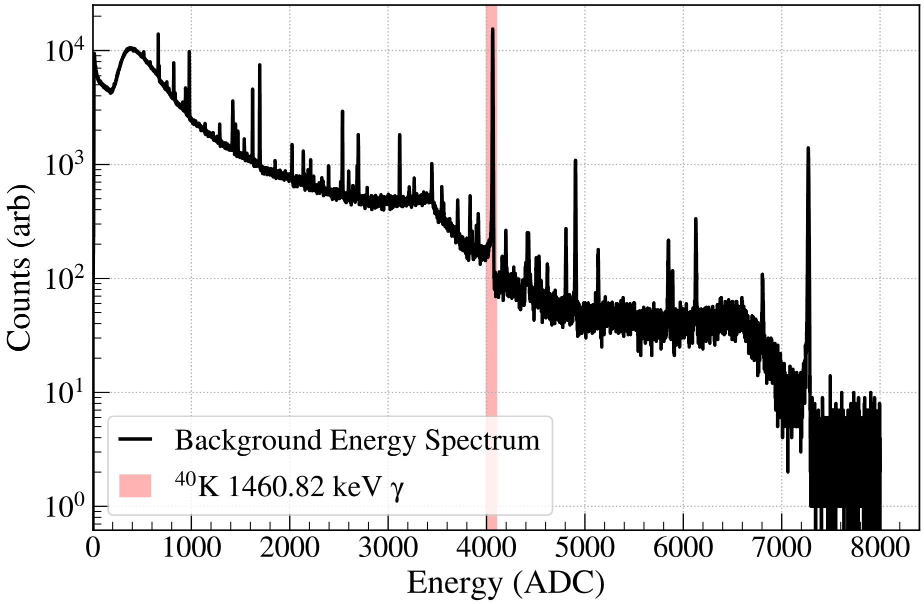

Figure 4.11: One run of a KrSTC background spectrum with the ^{40}K 1460 keV gamma peak highlighted.

A more complicated and accurate energy calibration involves fitting more peaks of known energy and applying a higher order polynomial calibration function. There are a number of peaks we can choose for our calibration. We seek to select peaks that have high enough statistics for fitting purposes, are well spread in energy, and minimize residuals when subtracting true energy from fitted calibrated energy. We also use optimized trapezoidal filter energies at this point, as is discussed in Section 4.4.5. Usually a fit to the top of a peak gives us a small enough uncertainty in energy that we can use that as the peak location. This peak-top fit is simply a second-order Taylor expansion fit used to find the mode and is known to be statistically stable and performant. We have also studied the effect of performing a more detailed peak fit to better account for our non-gaussian peaks. This provides a better fit to the entire peak but the peak-top fits provide a more accurate value for the peak energy. An example of both fits is shown in Figure 4.12.

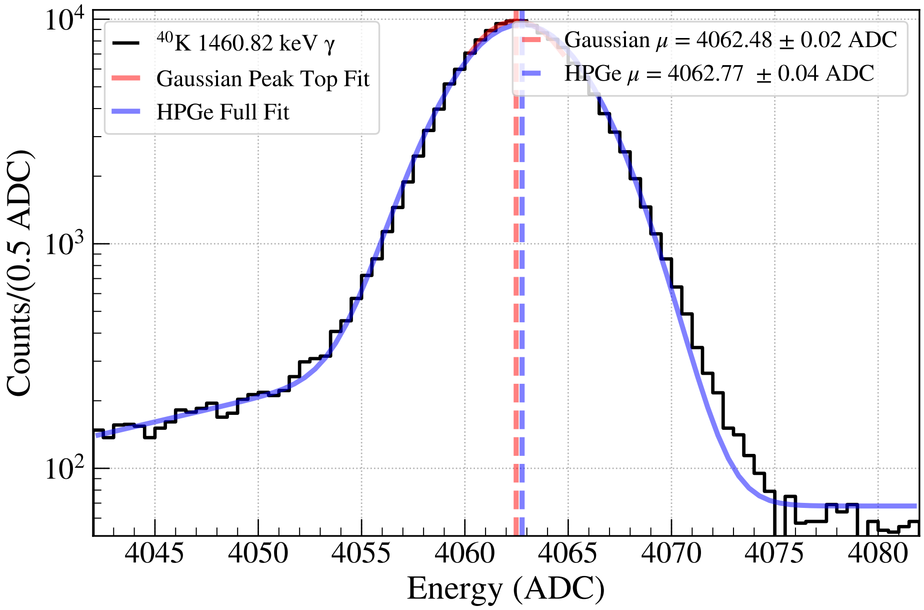

Figure 4.12: A gaussian peak top fit (top 10 bins) and a full HPGe peak fit (including low energy tail) on an uncalibrated background ^{40}K 1460.82 keV γ peak. The difference in fitted μ is at the sub-0.1 keV level, so a simple gaussian peak top fit should be sufficient for calibration, and seems to perform better in estimating peak location.

The resulting multi-peak calibration is shown in Figure 4.13. Although the uncertainty in the linear calibration parameters is lower than that of the quadratic parameters, the residuals in the quadratic case are noticeably smaller, as is true for a large majority of runs. Therefore we use a quadratic calibration. Note that this calibration is on data before we apply any dedicated nonlinearity correction, like the one described in Section 4.4.3.

We see some structure in the residuals of the quadratic energy calibration, hinting at possible energy nonlinearities that we cannot simply "calibrate out" of our analysis. We seek to remove one possible source of energy nonlinearity through an integrated nonlinearity correction.

4.4.3 Integrated Nonlinearity

One cause of energy nonlinearity comes from imperfect performance from the resistors in our digitizer [121]. An idealized digitizer assigns ADC values at each timepoint of a waveform with perfectly equal width. In reality, the widths of these ADC bins are variable and this variability is often structured and not random. We can correct for this nonlinearity in post-processing.

The procedure for performing the integrated nonlinearity (INL) correction is as follows: first we choose a precision pulser, in this case the PB-5 Precision NIM Pulse Generator from Berkeley Nucleonics Corporation. The specific pulser parameters used are shown in Table 4.2 and an example pulse is shown in Figure 4.14. Some considerations when picking these parameters were: a long enough fall time to avoid the waveform dropping more than one ADC per sample, a rate that gives us enough data without blowing up our file sizes, and as low an amplitude as possible.

This pulse is sent directly into the digitizer channel used for all of the KrSTC data-taking and then sent to ORCA. There is a "DAC offset" setting in ORCA that shifts the baseline of the incoming pulse by some amount of ADC. That value was not changed throughout the KrSTC dataset, so we only need to cover ADC values that would appear in some KrSTC raw waveform. Thus, we set the DAC offset to 33000 (arb units), take data for 1 second with 1000 waveforms at each offset, add 1 to the DAC offset parameter using ORCA scripting and repeat. We take data at 15000 different offsets to fully cover the dynamic range of the KrSTC data. Those data files were then transferred to NERSC for analysis.

The first step in the INL analysis is to window all the waveforms between 1000 and 3000 samples

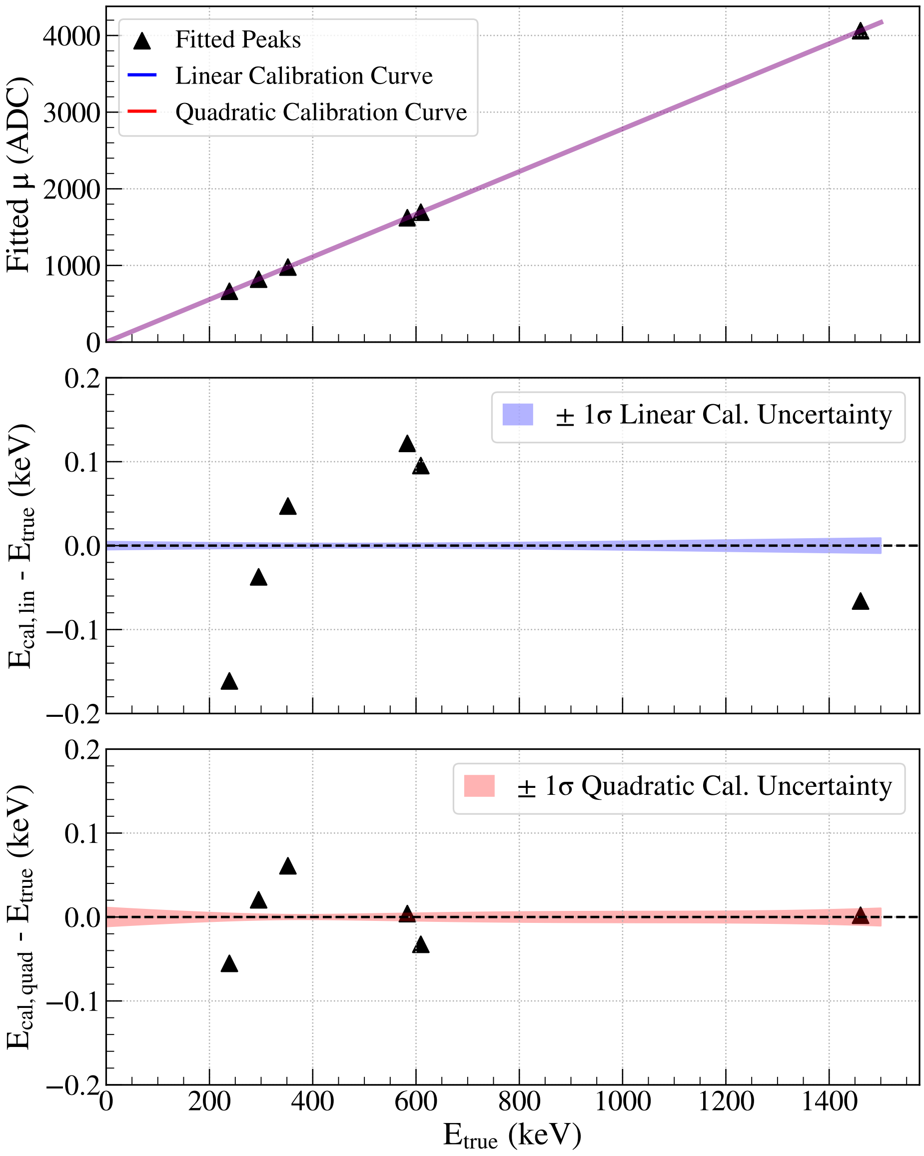

Figure 4.13: Calibration curve(s) of a long background run (C9 Run 85) with peak location residuals. A quadratic calibration performs better than a linear one despite slightly smaller fit uncertainties in the linear case. Individual peak fit error bars are too small to visualize. Uncertainties in the calibration curve fits are below 100 eV for both calibrations.

Parameter	**Value**
Pulse Rate	1 kHz
Amplitude	0.5008 V
Fall time	50 μs
Delay	250 ns
Flat width	100 ns
Rise time	0.05 μs
Polarity	Positive

Table 4.2: PB-5 pulser parameters for INL correction

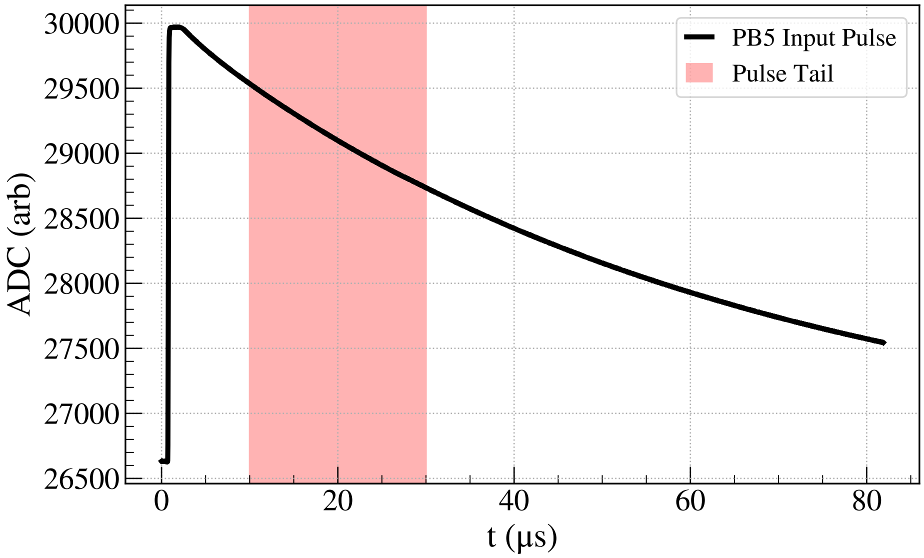

Figure 4.14: Pulser input for INL correction with tail portion of the waveform highlighted.

(10 - 30 μs) to capture a clean (and not too quickly varying) portion of the waveform tail. This tail should not decay through multiple ADC codes across a given sample. We then average all waveform tails together to get a global tail average. We take this average tail as a representative

tail shape with which to compare all our other waveforms. We load each waveform individually and find a baseline offset for the averaged tail such that its integral equals the waveform's integral. We histogram the number of times an ADC code shows up in a waveform as well as the summed residuals between the waveform and the averaged tail at each ADC value. We loop through all waveforms and add to these histograms. The ratio of the summed residual histogram and the ADC counts histogram is the INL as a function of ADC code, as seen in Figure 4.15. This is technically the INL up to some overall offset, as we were not able to sample the full ADC range of the digitizer, but this offset is removed by a constant calibration term. We subtract the INL value from each corresponding ADC value that appears in a waveform in the KrSTC dataset, correcting out this source of nonlinearity. The magnitude of the INL in the relevant ADC range is roughly 1 ADC, which corresponds to ~ 0.25 keV. The result of the INL correction can be seen in calibration residuals, as shown in Figure 4.16. The effects on the observed krypton spectrum can be seen in Section 4.5.1.

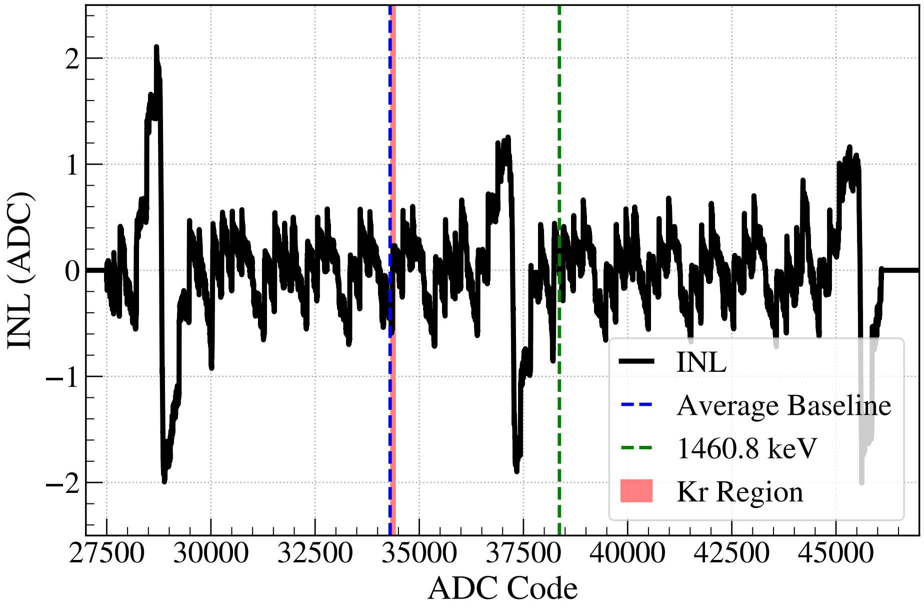

Figure 4.15: INL correction across KrSTC ADC range, with average KrSTC baseline value, krypton region, and 1460 keV shown.

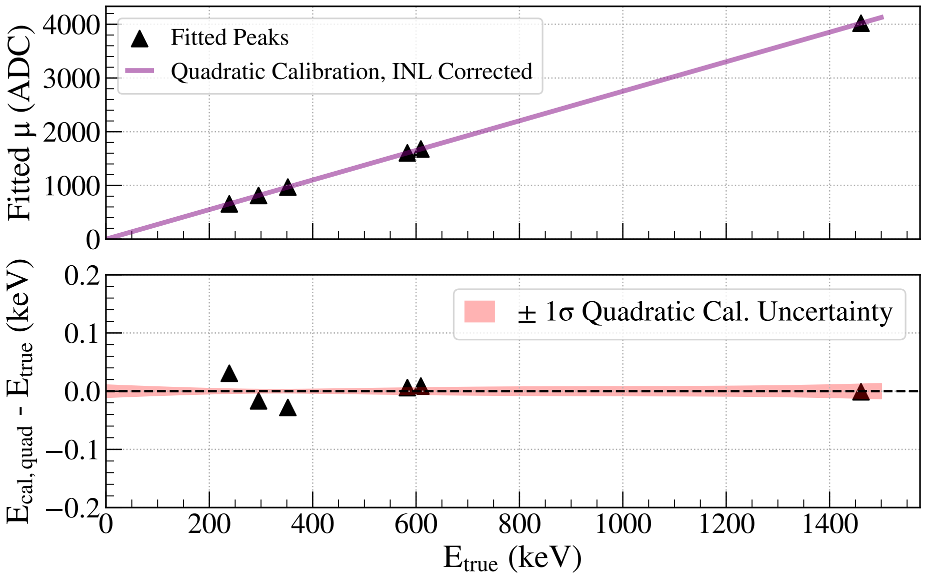

Figure 4.16: INL effect on quadratic calibration, to be compared with Figure 4.13. Peak location residuals are clearly reduced after the INL correction.

4.4.4 Pole-Zero

By the nature of our RC circuit electronics, our waveforms have a characteristic exponential decay, dominated by the RC decay time. However, there are other capacitances within our system that contribute different time constants to that decay. The poles of the transfer function that describes our output signals should give us those decay constants. We call these other decay constants our pole-zero constants and seek to correct them. An accurate pole-zero (PZ) correction is crucial for digital signal processing.

The basic idea behind the pole-zero correction we use, written by Sam Borden, is that we can sufficiently approximate our output signal as a convolution of 3 distinct exponential decays and apply a "Forward-Inverse-Forward" method. We first consider the long time constant coming from the RC decay in our circuit. We find that time constant (τ_1) by doing a fit to the baseline-subtracted tail of the waveform. We then correct it out (forward pole-zero correction) so we have a relatively flat tail. There are still faster time constants to worry about, so we perform another exponential fit on that once-corrected waveform and deconvolve out (inverse pole-zero correction) the most significant remaining faster time constant (τ_2). We are then left with a pretty clean exponential with a third time constant (τ_3). We perform the same operation as with the first forward pole-zero correction, giving us a nice flat signal. The intermediate steps of this operation are shown in Figure 4.17.

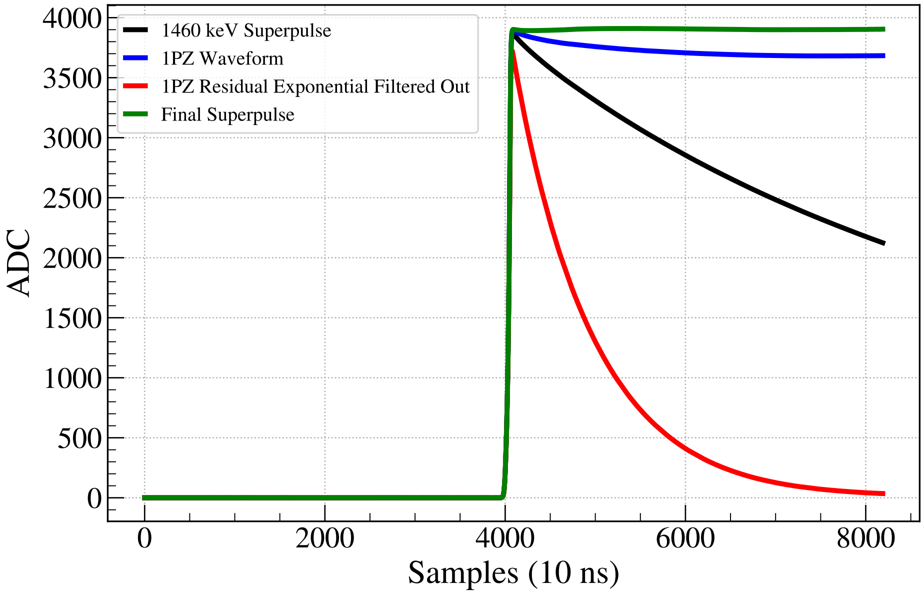

Figure 4.17: Pole-zero corrected KrSTC waveforms, showing the intermediate steps of the correction

4.4.5 Trapezoidal Filter

The amplitude of a pole-zero corrected waveform should be, to first order, proportional to the energy deposited in the detector during that event. However, electric noise can bias that amplitude to higher energies. One solution to this problem is to use a filtered output as an energy estimator. Trapezoidal filtering (trap filtering) is a fast and robust energy estimator [122] and we use the maximum of a trap filtered waveform (trapEmax) as our energy estimator for KrSTC.

We can perform a simple optimization of the risetime of our trap filter. We find an appropriate flat-top time to be 3 times the average risetime of a selection of pulses—our energy estimator should be fairly insensitive to changes in the flat-top time. Once we have this we can test multiple values of trap filter risetimes. We run this selection of pulses (taken from the ^{40}K 1460 keV peak) through our trap filter with the different risetime values. We can then take the maximum of the resulting filtered waveform (trapEmax) and use that as our energy estimator. What we seek to do is to minimize the full width at half maximum of this 1460 keV peak, so we fit a gaussian to the histogrammed trapEmax values for each risetime and measure the gaussian width (σ) divided by the uncalibrated location of the peak (μ). We can take the log of those ratios and plot them against the log of the corresponding risetime values, giving us a noise curve. This is the sum of the voltage noise, current noise, and $1/f$ noise added in quadrature. We can then use a quadratic fit to find the minimum of this curve. The minimum of this fit is the risetime we select. A plot detailing this method is shown in Figure 4.18.

4.4.6 Energy Resolution

Outstanding energy resolution is one of the many benefits of germanium detectors. When looking for low energy krypton peaks separated by $\mathcal{O}(1 \text{ keV})$, we must have performant energy resolution to be able to resolve those peaks. As part of our calibration function we fit known peaks across a wide energy range. We can use those peak fits to estimate our resolution at low energy where we see no known peaks aside from potential krypton events. The equation that governs this energy resolution is shown in Equation (4.1):

$$\sigma(E) = \sqrt{\sigma_{\mathrm{n}}^2 + F\varepsilon E + \sigma_{\mathrm{CT}}^2 E^2} \tag{4.1}$$

from [60]. The three components that determine our energy resolution are: the constant noise term (σ_{n}), Fano term ($\sqrt{F\varepsilon E}$), and the charge trapping term ($\sigma_{\mathrm{CT}} E$).

The noise term is independent of energy and will dominate the energy resolution in the krypton region. This noise term will have a large contribution from electronic noise, but leakage current, capacitance, and depletion can all have an impact on the detector side. The capacitance of PPC detectors is quite low compared to other germanium detector geometries which is a bonus of our setup. This noise component is expected to remain fairly constant across a single stable data-taking

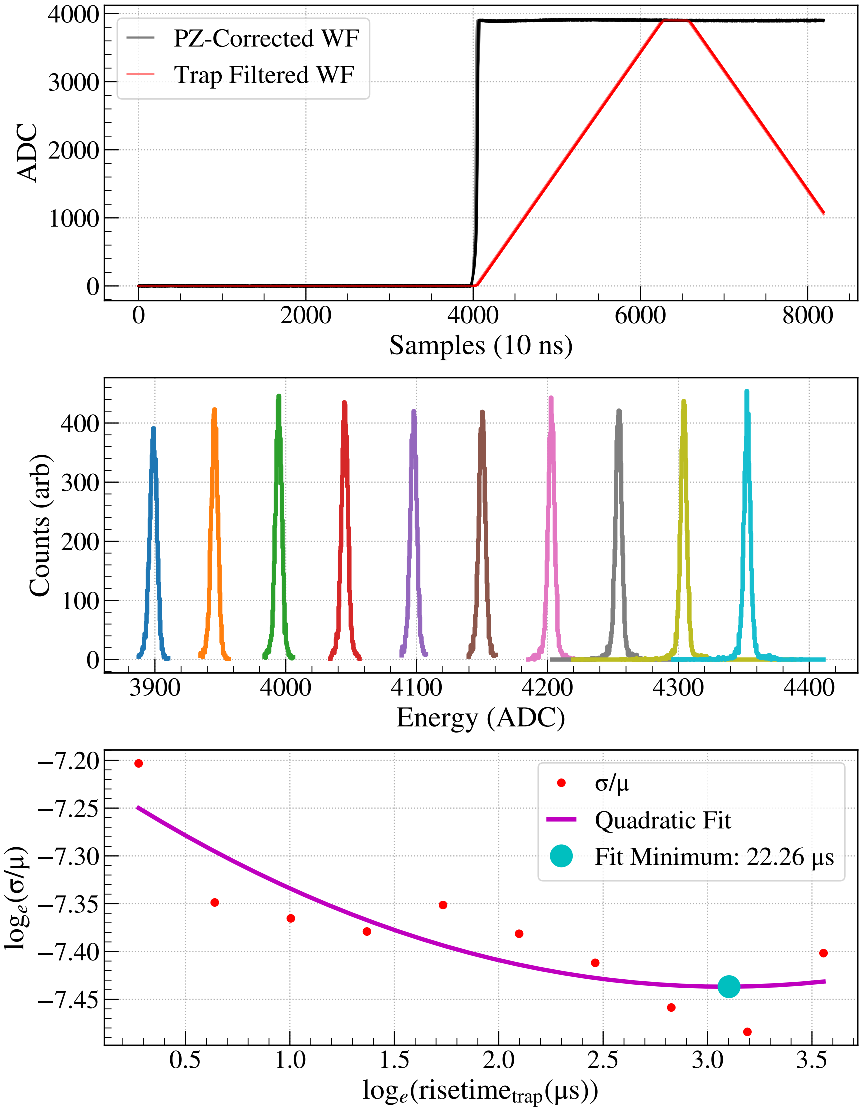

Figure 4.18: KrSTC trapezoidal filter optimization, with (*top*) a trap-filted, PZ-corrected waveform, (*middle*) the resulting uncalibrated 1460 keV peaks from applying different trap filter parameters, and (*bottom*) those 1460 keV peaks' σ/μ values and logarithmic quadratic fit used to find the best trap filter parameters.

campaign.

The Fano term comes from the sub-Poissonian processes involved in creating electron-hole pairs in semiconductors. There is some significant fraction of energy in these events that goes into ionization, but some of that energy can go into other processes like phonon generation. The Fano factor describes how much "better" than Poissonian statistics you can do with your resolution. A Fano factor of 1 yields a purely Poissonian distribution (which in our large value approximation is gaussian), and a Fano factor of 0 would yield a delta function. Germanium has a Fano factor near 0.1, meaning we can do quite better than purely Poissonian statistics would suggest. The Fano term is also scaled by the average energy needed to create an e-h pair ($\varepsilon = 2.96$ eV).

The charge trapping term comes about from different types of charge traps in our detectors. Impurity sites in the crystal as well as surface charges can cause charge carriers in the conduction band to get "stuck" and re-released on a slow timescale, causing a slight degradation in the measured energy. This term scales with drift time (and thus the deposited energy or number of charge carriers created by the ionizing radiation).

We can fit a number of peaks across a wide energy range in our background energy spectrum and plot those peak widths against their calibrated energy. If we then fit that function to the square root of a quadratic in energy, we find our energy resolution function as described in Equation (4.1) and shown in Figure 4.19.

4.4.7 Energy Threshold

The energy threshold is an important parameter for our krypton searches. Having a lower energy threshold gives us more information about the krypton spectral shape, but having too low a threshold leads to file size bloat from noise triggers. Keeping the energy threshold so low is difficult and requires careful consideration of the contact pin/point contact interface, the front-end electronics, cabling inside and out of the cryostat, our post amplifier, our HV supply and HV filter box, and any involved power supplies. Ground loops can be easily introduced and much time is taken to place the post amplifier and HV filter boxes in the optimal positions and with good physical contact with the cryostat. There is also instability in noise performance when the operating bias is too near the breakdown voltage or when there is increased leakage current. Bias voltages were set at the highest voltage without increased leakage current to yield the lowest noise levels. Even in campaigns with good noise performance and low energy thresholds, there is still significant noise on any low-energy

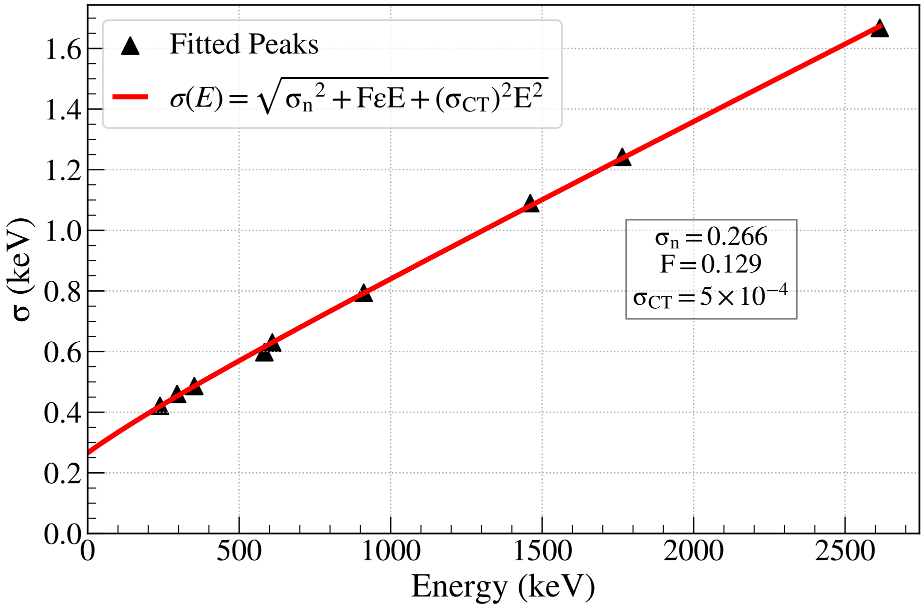

Figure 4.19: Energy resolution of 9 known peaks and a fitted energy resolution function as described in Equation (4.1). The Fano factor found matches up with expected values from [60] and the charge trapping component is small.

waveform, as shown in Figure 4.20. This leads to difficulty in using pulse shape discrimination techniques at these low energies, as we will discuss in Sections 4.5.5 and 4.5.4.

4.5 Results

4.5.1 Energy Spectra (Wet vs. Dry)

After all our processing and calibration we have the final analysis parameters to do a detailed analysis of the KrSTC dataset. The most basic analysis is a comparison of background-subtracted krypton energy spectra across different campaigns, shown in Figure 4.21.

This plot is immediately interesting for a number of reasons. First, we can split all our data-taking campaigns into two distinct categories: dry and wet (the source of these names stems from our hypothesis of residual gasses condensing on detector surfaces, as will be discussed later in this

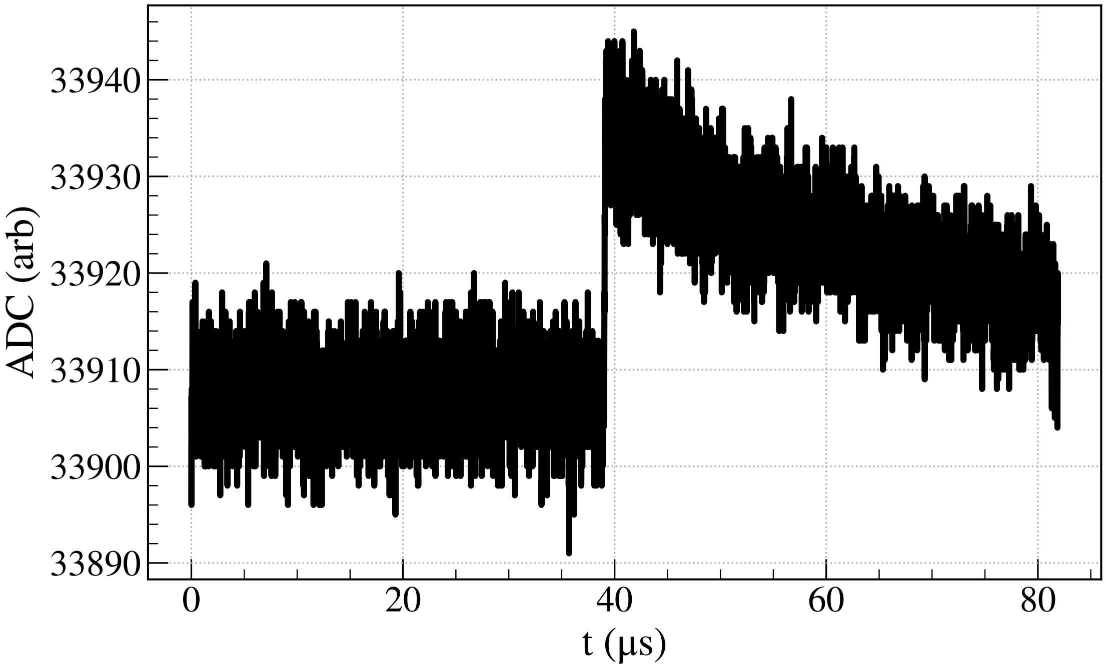

Figure 4.20: Low energy waveform from KrSTC data. This waveform has energy of ∼ 12 keV which is in the krypton region. With this low signal-to-noise ratio, pulse shape discrimination becomes significantly more difficult.

Section). The main characteristic of dry detector spectra is a lack of peaks from any photons or electrons expected from the $^{83\mathrm{m}}$Kr decay brought about by significant energy degradation of those decay products. The background-subtracted energy spectrum simply looks like a low-energy excess below ∼ 10 keV and is difficult to see without an appropriately low energy threshold. This behavior is thought to match that of the Majorana Demonstrator energy spectrum, with the expected ^{210}Pb lines degraded in energy in that case (see Section 4.1). In comparison, the wet detector spectra have distinct peaks at the photon line energies, with no electron peaks seen but much less energy degradation than dry spectra such that some events appear just below the expected electron energies. Modeling one or both of these detector behaviors is the crux of this work.

Acquiring good dry detector behavior was difficult for multiple reasons. One reason was that we initially thought this was simply a lack of krypton, especially with runs that had higher energy

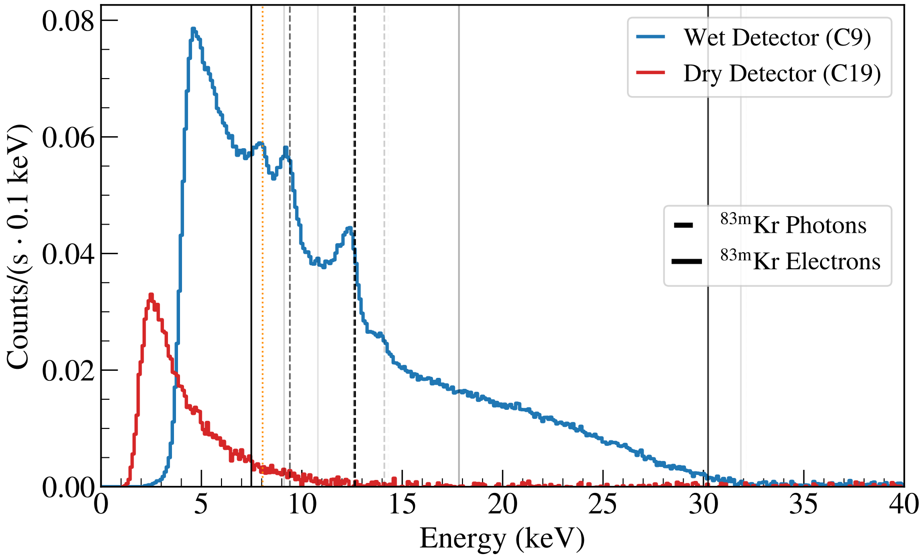

Figure 4.21: KrSTC wet and dry detector background-subtracted krypton spectra. Also plotted are the $^{83\text{m}}$Kr decay photons (electrons) with their opacity scaled by relative intensity compared to other photons (electrons).

thresholds. These spectra only became interesting to us when we decreased noise in our system enough to lower the energy threshold and see the spectral shape with sufficient statistics. It also required very specific detector conditions, as we will discuss. Two example dry detector spectra are shown in Figure 4.22.

Wet detector runs were more frequent and had higher statistics in the krypton region. Three example spectra are shown in Figure 4.23. There are interesting differences in the spectral shapes from different campaigns which will be discussed. There are also noticeable changes in energy threshold settings between campaigns, making it difficult to compare the lower energy spectral shapes between wet detector spectra. A clear difference in these spectra is the calibration: the krypton photon peaks seem to lineup quite well in the Campaign 9 (C9) spectrum—the steep spectrum from electron degradation visually shifts these peaks slightly, but there is no evidence of degradation of the photon lines. C17 and particularly C22 seem to be more poorly calibrated. This could be attributed to some difference in the noise performance of the system adding an unaccounted-for

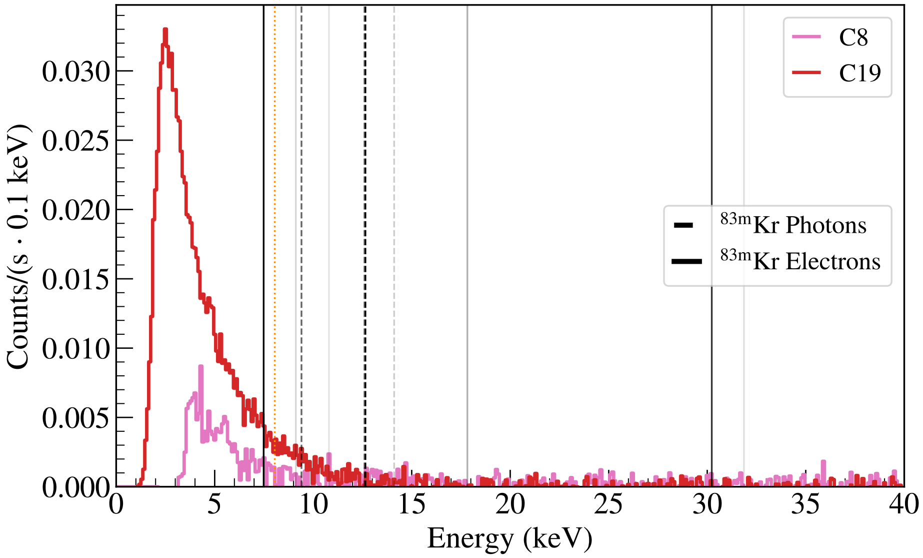

Figure 4.22: KrSTC dry detector spectra with difference in krypton rate attributed to decaying ^{83}Rb, changing ^{83m}Kr emanation rate from source, energy threshold values, and changing detector conditions. Pressure at cooldown for C8 $= 7.2 \times 10^{-7}$ mbar and for C19 $= 1.8 \times 10^{-6}$ mbar.

nonlinearity. Another consideration is a non-linearity at low energy of the trapEmax parameter. Utilizing a fixed-time-pickoff could potentially avoid this nonlinearity and is worth considering in future analyses. This is separate from the INL correction we performed on the whole KrSTC dataset, which does not explain fully the difference in calibration of these spectra. The effect of that INL correction on the C9 krypton spectrum is shown in Figure 4.24.

The main difference between these wet detector spectra (aside from overall rate, which depends on the decaying ^{83}Rb source, changing ^{83m}Kr emanation rate from the source, energy threshold values, and changing detector conditions) appears to be the energy degradation of the electrons. In C9 and C17, there are slight differences but the continuum between ~ 15 keV and ~ 30 keV—which is dominated by the 30.23 keV (63.7% intensity) electron—seems to line up. Both continua show a roughly linear degradation of this electron line. This is interesting because these campaigns were taken over three months (and over 1 half-life of ^{83}Rb) apart. This suggests that the spectral shapes and rates are quite different when accounting for the source decay, although there are other detector

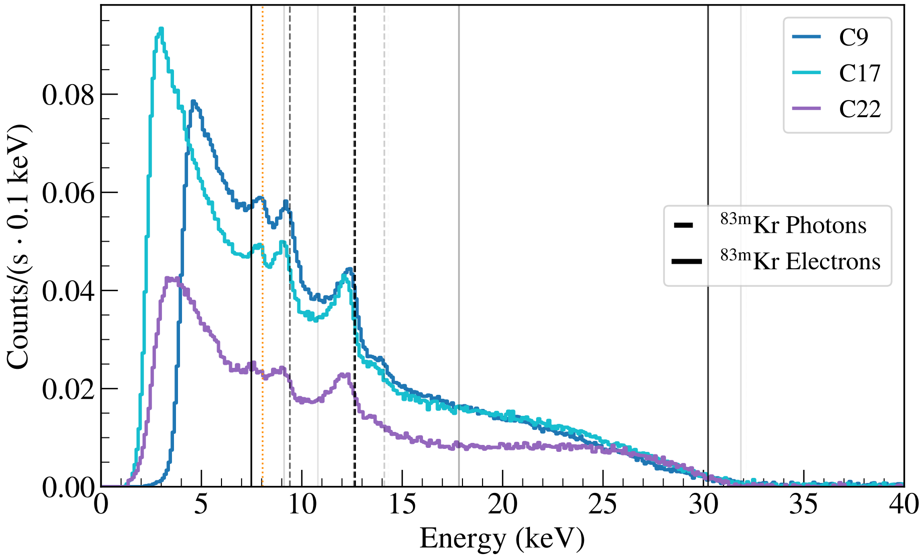

Figure 4.23: KrSTC wet detector background-subtracted spectra, with difference in krypton rate primarily attributed to decaying ^{83}Rb source and difference in spectral shape attributed to different detector conditions and less optimal energy calibration of C17 and C22. Pressure at cooldown for C9 $= 7.5 \times 10^{-6}$ mbar, for C17 $= 3.8 \times 10^{-6}$ mbar, and for C22 $= 2.6 \times 10^{-6}$ mbar. Note: this energy calibration uses the INL correction.

performance effects at play and drawing conclusions from this comparison would be difficult. C22 has a different spectral shape in this higher energy krypton region, with a more "shelf-like" behavior. The electron seems to be less degraded, yet there is still no electron peak at the full energy. The photon peaks also appear broader, but it is hard to determine true peak energy resolution when sitting on an unknown background.

There is no evidence that we see the 32.15 keV γ (0.062% intensity) from the first stage of the $^{83\text{m}}$Kr decay. This is expected given the activity of our krypton source. If detectable, this could have given us a clue as to the size of the dead layer with which we are dealing. It is possible that we could have seen this gamma in our dry detector runs, or that it would have been degraded some amount, or both. Data with a higher activity source could search for this interesting peak.

We also do not see anything past the beginning of the energy degradation of the 31 keV electron.

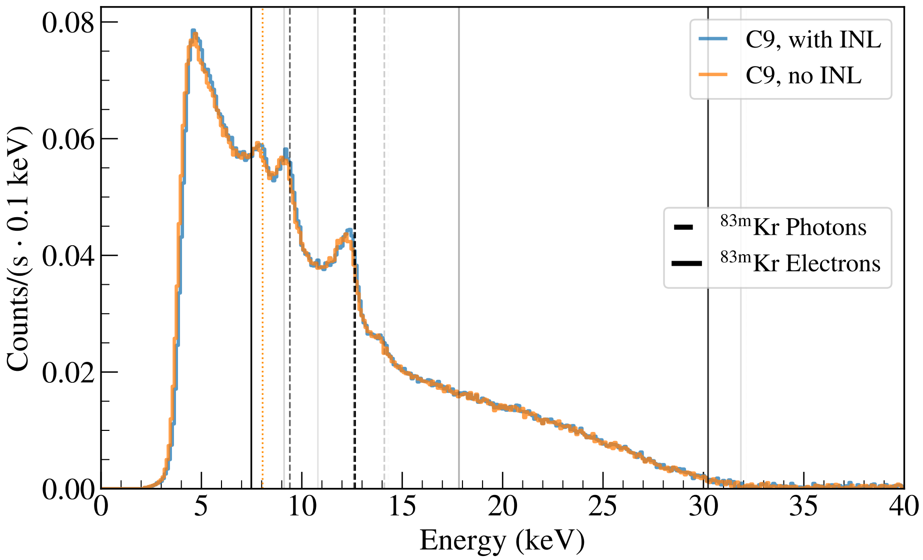

Figure 4.24: INL effect on C9 background-subtracted krypton spectrum, we see some very small shift toward true energies of $^{83\text{m}}$Kr photon peaks. The INL correction improved calibration residuals at higher energies but did not have a significant effect in the krypton region.

It is not impossible that we could see an event at the Q-value of the krypton decay (41.6 keV), but that would require detection of multiple decay products in coincidence, at least one of which would have to back-scatter off some material in the cryostat, and none of those particles could be degraded. Thus, we see nothing at those higher energies, as we expect.

A line that we did not expect to see that we do see in all of our wet detector campaigns shows up around 8 keV. This was determined to be the 8.05 keV x-ray fluorescence line from copper. There are significant amounts of copper very close to detector surfaces and many low-energy decay products capable of exciting this copper.

After much hypothesis testing we discovered the key component that determined whether a run would exhibit dry or wet detector behavior was the value of the pressure at cooldown (PAC). Specifically, cooling the detector down at a lower PAC (pumping on the cryostat for longer) would lead to dry detector behavior, while cooling down at a higher PAC yielded wet detector spectra. This was also subject to the time elapsed since a bake of the detector. If we cooled down at a higher PAC a few times in a row, the detector was more susceptible to be in a wet detector state even if we then pumped on it for a longer time. Baking the detector would often "recover" that dry detector state. The pressures at cooldown for each spectrum shown are mentioned in the captions of their associated figures.

The proposed model for the difference between wet and dry detector revolves around residual gases (especially water vapor) that condense on detector surfaces when the detector cools down to LN temperatures. We theorize that dry detector runs look like the MAJORANA DEMONSTRATOR low energy spectrum because the cryostat conditions are much closer to that of MAJORANA DEMONSTRATOR, with very low PACs. For wet detector runs, more gases are condensing on surfaces and changing the distribution of charges near the detector. This modeling will be discussed extensively in Section 5. This model is supported by the fact that we were not able to bias the detector all the way to our standard operating voltage of 2700 V for the wet detector campaigns. We were able to run at 2700 V for the dry detector campaigns. The theory is that this condensation on the passivated surface would lead to leakage current at lower voltages. We tested if operating a dry detector at 2400 V would yield a wet detector spectrum and there was no noticeable difference in the spectra from 2700 V to 2400 V. Bias voltage did not affect the spectrum significantly, it only served as an indication of the state in which the detector was operating.

An important point to consider is whether or not the photon peaks we see in the wet spectra are actually at the expected energies and are not energy degraded. If there were to be some energy degradation, we would expect these peaks to be broadened to some extent. Performing a spectral fit in this region is quite difficult, given the changes in detector environment and noise behavior between different campaigns, as well as many degenerate fitting parameters. However, the resolution of these photon peaks seem qualitatively consistent and we do not believe there is significant broadening. Additionally, after the INL correction and calibration, we see the photon peaks line up quite well with expected values in the Campaign 9 data. Campaign 22 shows photon peaks at lower than expected energy but it is not expected that this is due to more energy degradation; there are energy nonlinearities that change between campaigns. More study could be performed to confirm these photons are not degraded but it is a reasonable assumption to say they appear in our spectra at their full energy values.

4.5.2 Data Stability

Data stability is important to understand so that we can easily combine runs into larger campaign datasets. Provided we are at an appropriate bias voltage, baseline values do not significantly drift during campaigns. Outlier baseline values are tagged in the data cleaning process discussed in Section 4.4.1. Gain (and thus, energy calibration) can drift a bit and a more finely tuned (per cycle or per multiple cycles instead of per run) calibration would likely improve energy residuals of some krypton spectra, but this is not a source of concern.

An interesting source of data instability shows up at the beginning of most campaigns. We often begin campaigns soon after biasing the detector with a few background cycles and then start our first krypton run. This first krypton spectrum is susceptible to instability that changes the overall krypton rate, at least in wet detector runs. Examples of this spectral change is shown in Figure 4.25. The C17 spectrum (right plot) is particularly interesting because the krypton rate grows to a maximum and then relaxes to a "equilibrium" rate over the course of tens of hours. This is not expected to be caused by diffusion of the krypton gas because of the larger timescale. The current theory is that the potential surface charge conditions on and near the detector are changing and taking time to equilibrate. This may also be the reason for the depletion voltage of the detector changing after the detector is biased for some time. This is a difficult effect to study further because the runs after those shown are decay runs, so disentangling that change in rate with the expected decay of the krypton is challenging. The sensitivity of detector charge collection to the external environment is one reason LEGEND has focused more on the IC detector design given its larger disk-line $p+$ contact and smaller passivated regions only in the ditch surrounding the $p+$ region.

Stability in the krypton rate is seen later in those same campaigns in Figure 4.26. There is also an interesting part of the C17 stable spectrum. The first grouping of events is slightly higher than the rest of the run. This is attributed to a build-up in pressure of the krypton gas inside the source. When that source is opened, more radioactive gas finds its way into the cryostat, giving you an initial "Kr burst" that equilibrates after a few hours (or a few Kr half-lives).

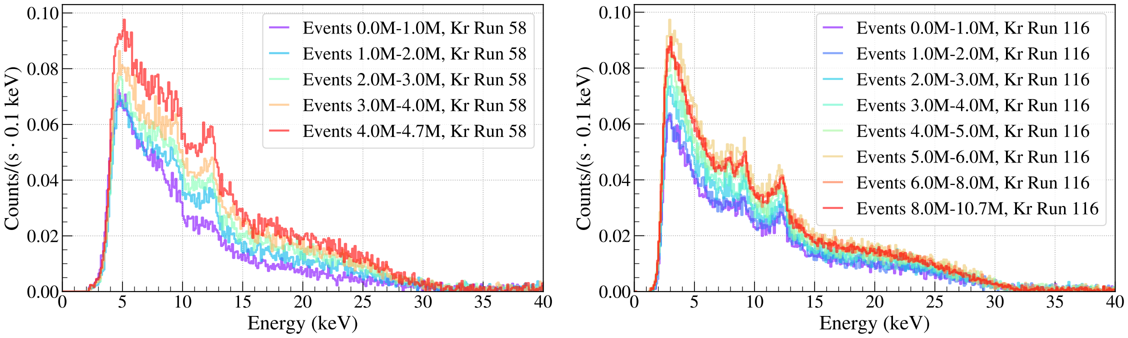

Figure 4.25: The krypton spectra of wet detector runs early in the data-taking of C9 and C17, grouped in time by event number. The overall event rate is dominated by background events, so the grouping of events roughly corresponds to uniform units of time. It takes ∼ 3.5 hours to reach one million events. The instability of the krypton rate appears to stabilize after ∼ 24 hours.

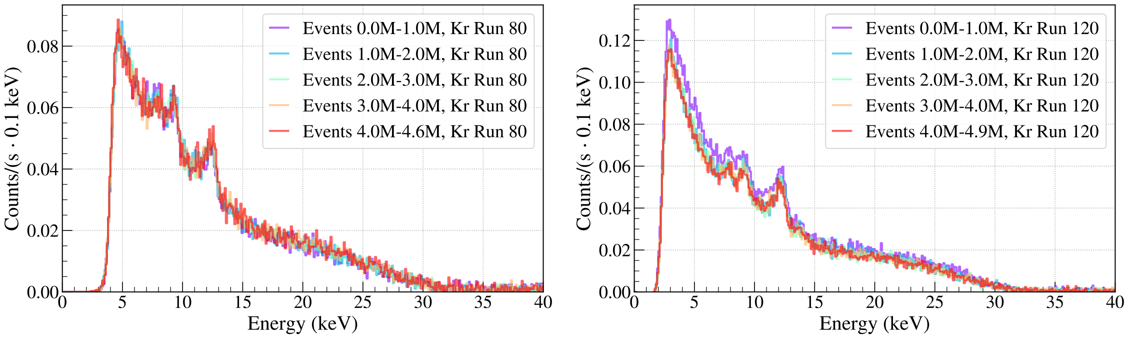

Figure 4.26: The krypton spectra of wet detector runs later in the data-taking of C9 and C17, grouped in time by event number. This stability shows up after the equilibration we see in Figure 4.25. In C17 we see evidence of a "Kr burst," lasting over a few hours.

4.5.3 Decay Runs

An important check that we are actually seeing krypton events is to take data while the krypton is decaying away in the cryostat. We close the valve connecting the source and the cryostat with the valve connecting the pump and cryostat still closed. This cuts off our krypton supply and allows us to watch the krypton gas decay away with half-life $\tau = 1.83$ hours. This half-life is not easy to measure precisely as the source activity is not strong enough to give significant statistics in this short time frame, but there is clear evidence of the krypton decaying away with a comparable half-life, as shown in Figure 4.27.

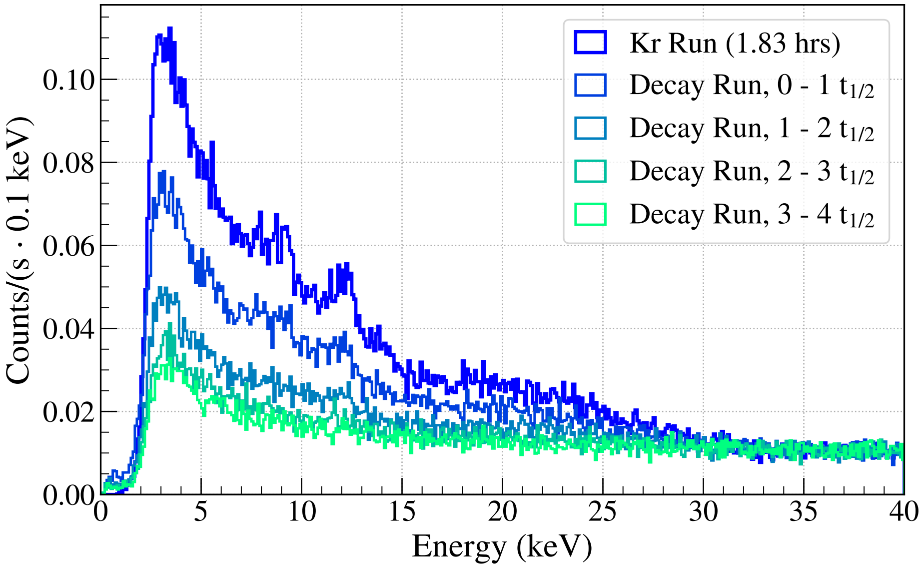

Figure 4.27: Krypton decay spectrum in wet detector campaign C17 when krypton is valved off from cryostat. The spectra are grouped in $^{83\text{m}}$Kr 1.83 hour half-life windows showing the decay of the radioactive gas.

This decay study was not possible if we valved in the pump to the system. This would almost immediately bring the krypton rate down to zero and give us a background-like spectrum. This suggests that the krypton was not sticking to cold detector surfaces and was in a gaseous state. It is not impossible that some of the krypton did cryopump onto cold surfaces but even if it did, when the pressure was lowered from pumping on the cryostat, that krypton was removed from the system into the pump.

4.5.4 Pulse Shape Discrimination — T/E

Krypton decay products are all low energy electrons and photons. These ionizing particles have very small penetration depths, most of them below 100 μm. Therefore, the only way these krypton events can deposit a significant-enough amount of their energy is for them to penetrate through the passivated surface or $p+$ point contact region. The $\sim$ 1 mm-thick $n+$ transition layer is too large for these events to deposit enough energy to be seen within $\sim$ 10% of their true energies. A consequence of this is that krypton signals are expected to rise more quickly in the early part of the waveform compared to regular bulk events. We can make cuts on energy and PSD parameters and then make a superpulse (time-aligned average of many normalized waveforms) to look at the difference between expected krypton events and bulk gamma events. Such a comparison is shown in Figure 4.28, with the PSD and energy cuts for each superpulse shown in Figure 4.29.

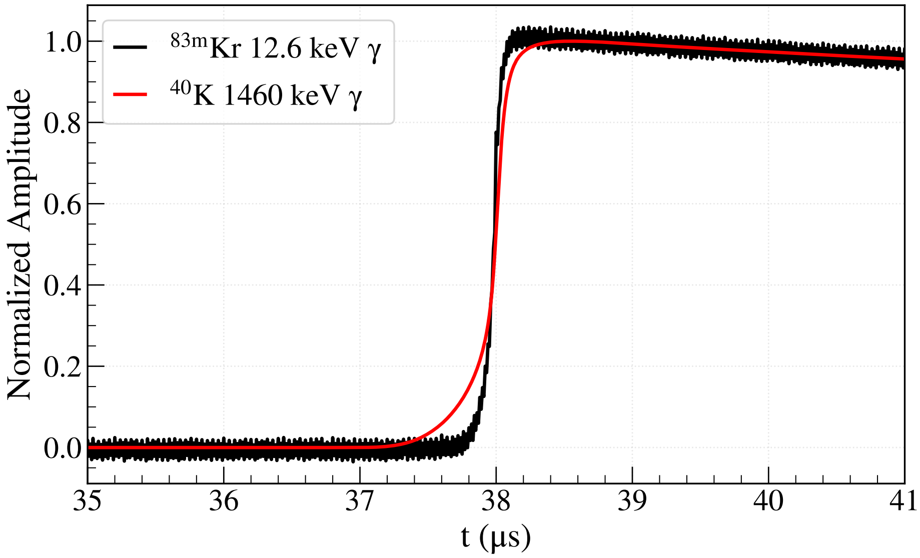

Figure 4.28: Superpulses of krypton events and bulk gamma events, using T/E and energy cuts shown in Figure 4.29. The superpulses are each averages of $\sim$ 5000 waveforms.

The majority of background events in this low energy krypton region are thought to be shallow angle Compton scatters (with some possible tritium decay contamination). These background

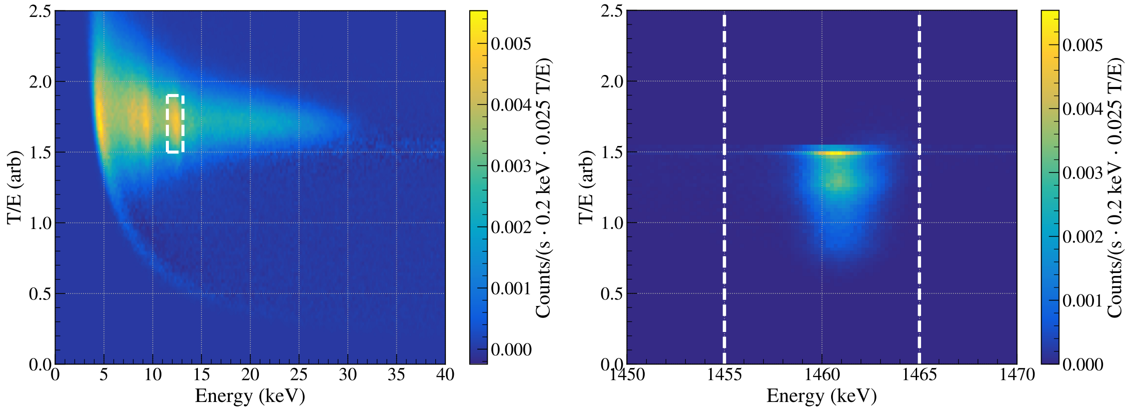

Figure 4.29: T/E distributions and cuts for krypton and bulk gamma superpulses shown in Figure 4.28.

events should be spread evenly through the detector and thus will on average have an initial waveform rise that is not so fast. The krypton events should have quick initial rises due to their proximity to the $p+$ region where the detector's weighting potential changes most rapidly (see Section 2.3.2 for more explanation). This is one possible way to use pulse shape discrimination (PSD) to tag events as krypton events (or more broadly, surface events).

One of the most useful analysis cuts in LEGEND is the A/E cut. This cut considers the maximum current of a waveform (evaluated through an asymmetric trapezoidal filtering, essentially a derivative) divided by the energy of the event. This parameter is effective in finding events that are "faster" (high A/E) or "slower" (low A/E) than normal. Low A/E events often consist of energy depositions in the $n+$ transition region where there are low electric fields, and high A/E events can come from depositions near the $p+$ region. This could also be a powerful tool for the KrSTC analysis. In our case, we prefer the T/E parameter. The T is the maximum output of a triangle filter. The key difference is that this T filter acts as a derivative of the charge signal on a smaller timescale than the A/E classifier. This is necessary in the low energy region due to less accumulated charge and thus more subtle differences in current signals as well as more significant amounts of noise.

The T/E vs. energy distributions for C9, the highest stats wet detector campaign, are shown in Figure 4.30.

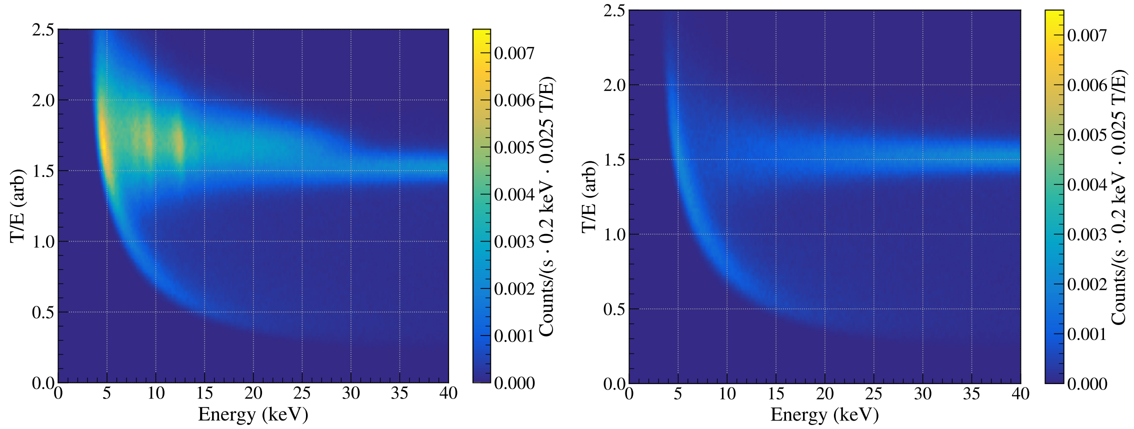

Figure 4.30: T/E distributions for wet detector krypton (*left*) and background runs (*right*), from C9.

These T/E distributions shows some more interesting structure as compared to their risetime counterparts. In particular, we see bands in energy corresponding to photon peaks in the wet detector spectra which makes sense given the larger range of penetration depths of those photons compared to electrons. However, the background T/E distribution is still not well separated from the krypton band. Additionally, we see a filtering artifact at low energies. For events with small enough amplitude, the noise dominates and the filter is liable to pick up the most extreme upward fluctuation of the noise in the baseline. This, scaled by 1/E, gives this "banana"-shaped feature that cannot distinguish between krypton and background events. This makes a T/E cut only somewhat useful on low energy events, as seen in Figure 4.31.

4.5.5 Pulse Shape Discrimination — Risetime

A more direct calculation of the "risetime" of our waveforms is also an interesting PSD parameter. The distribution of risetimes plotted against energy is shown in Fig 4.32.

Risetime here is defined as the amount of time it takes a signal to go from 2% to 20% of its full amplitude. Due to an unfavorable signal to noise ratio at low energies, we also apply a Savitsky-

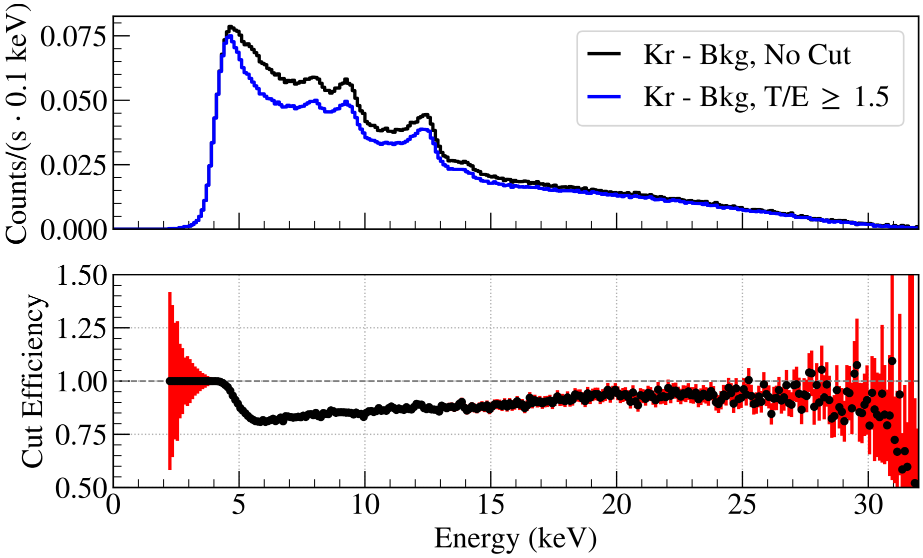

Figure 4.31: T/E cut efficiency for tagging krypton events in wet detector runs, from C9.

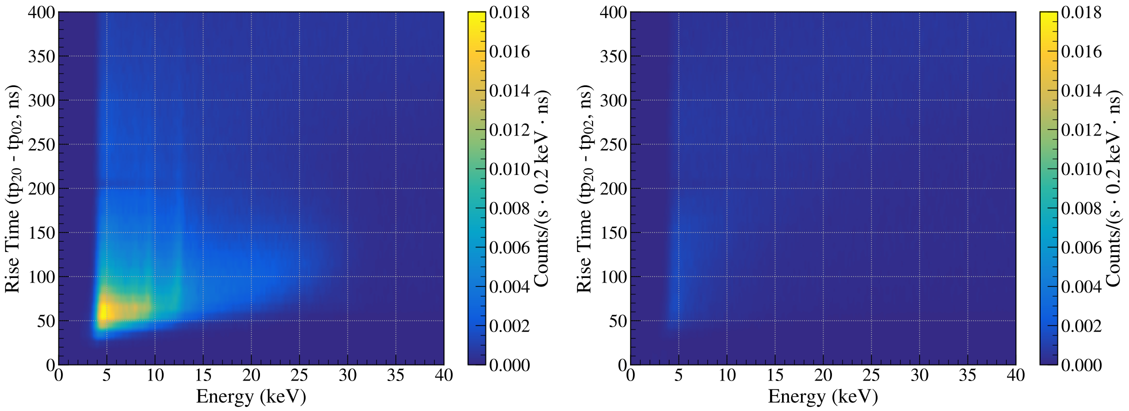

Figure 4.32: Rise time distributions for wet detector krypton (*left*) and background runs (*right*), from C9. The background distribution is very faint but there is a population at low energy and risetime overlapping with the krypton distribution.

Golay filter to smooth the the waveforms before finding these time points (referred to as tp_n for the $n\%$ time point).

We see a distinct population of events at low risetimes that we expect to be our krypton events. There is a non-negligible amount of overlap between suspected krypton and background events which makes performing a risetime cut difficult yet interesting on low energy events. Such a cut is shown in Figure 4.33.

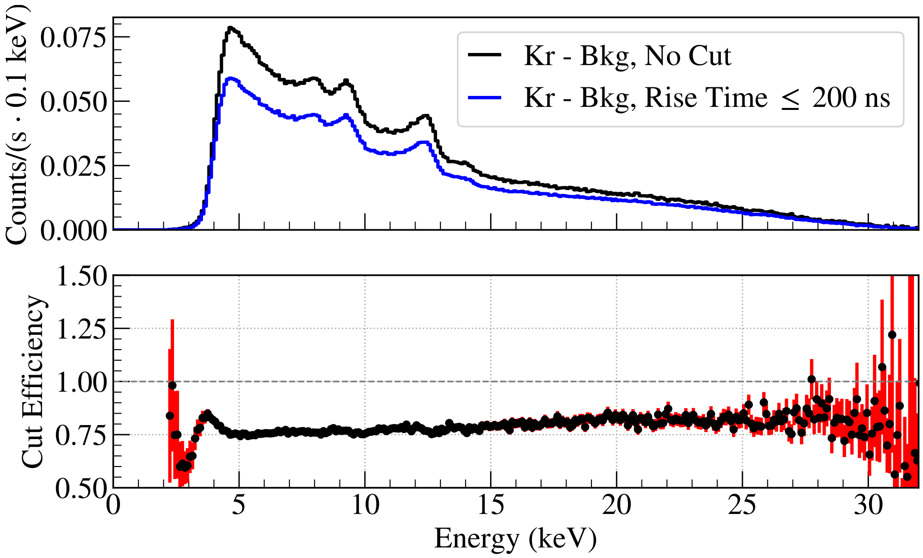

Figure 4.33: Risetime cut efficiency for tagging krypton events in wet detector runs, from C9.

Risetime is not the most reliable PSD parameter at low energies since it becomes much more difficult to define where a waveform begins and ends given the lower signal-to-noise ratio. This is the reason we consider tp_{02} as opposed to tp_0. Smoothing the waveform helps here but is not ideal due to the loss of some information. We are also slightly biased due to our method of finding these time points. We step back from the max of the smoothed waveform until we cross the first instance of the waveform reaching $n\%$ of its amplitude. At high energies this is still not trivial but is a cleaner process.

That said, both the risetime and T/E are good checks that the krypton events are near the $p+$ region and are behaving roughly as we expect.

Chapter 5

KrSTC Simulations

We seek to model our surface charge hypothesis through simulations to better understand the behavior in our KrSTC dataset. This necessitates two distinct simulations: a particle simulation considering krypton decays on our germanium detector and a pulse shape simulation considering the effect of surface charge on our charge collection.

5.1 $^{83\mathrm{m}}$Kr Particle Simulation

In order to model this surface charge hypothesis, we must have a reliable particle simulation that accurately produces energy depositions of $^{83\mathrm{m}}$Kr decay products in germanium. For this we use the Geant4 (G4) simulation package [123] and a modified version of g4simple [124]. The most crucial inputs to this simulation are the detector dimensions and the krypton decay scheme.

5.1.1 OPPI Detector Dimensions and CT Scan

Reports of the OPPI dimensions are inconsistent and the detector geometry is very important to our simulations. To this end we decided to use the CT Scanning facility at UW to try to accurately measure OPPI's dimensions. Images of this CT scan (with rough pixel counts) are shown in Figure 5.1.

There is some variation in the images as the machine scans around the detector and x-rays bounce off the edges of the detector. We chose the cross sectional image with the least distortion in r and z both for the full detector and for the point contact. This was in the middle of the group of images we received so we imagine this is a cross section of the center of the detector. We can use free photo editing software to count the pixels in these images and use the ratio of different pixel counts to estimate the ratios of the dimensions. In particular, our simulation proves to be very sensitive to the size of the p+ point contact region. We find this region to differ significantly from

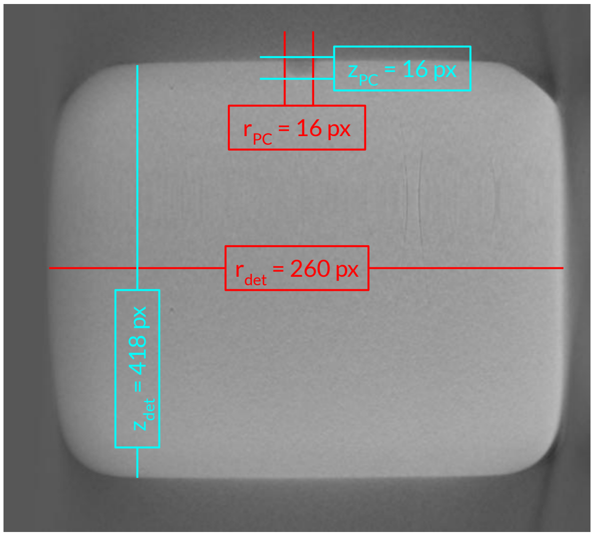

Figure 5.1: CT scan of OPPI, showing some rough pixel counts of the point contact and the full detector length.

previous models and reports of OPPI dimensions, with the point contact being a perfect hemisphere of radius $r = 1.9$ mm. We also take the $n+$ bevel to be 6 mm long at a 45° angle (not fully accurate but able to model this way in the pulse shape simulations) and the full detector $(r,\, z) = (30.8,\, 51)$ mm.

We also took pictures with a phone of the detector and did the same pixel counting process as a check of the CT scan procedure. There was not perfect agreement but measurements were within reasonable ranges that we went forward with the dimensions determined from the CT scan. The CT scanner stated a resolution of ~ 100 μm, likely with some added uncertainty from variations between cross sectional images.

5.1.2 Other KrSTC Hardware Dimensions

The material adjacent to the detector in our hardware setup is also important to properly model in our G4 simulations. The hardware pieces we include in our simulation are the copper contact pin that connects to the p+ point contact, the copper “Mercedes piece” that sits above the detector, the copper rods that connect to the Mercedes piece, and the copper can IR shield that contains all the other hardware. These objects were modeled using a CAD rendering that was converted to GDML to provide reasonable estimates of their locations and sizes. An image showing some of those components in the simulation is shown in Figure 5.2.

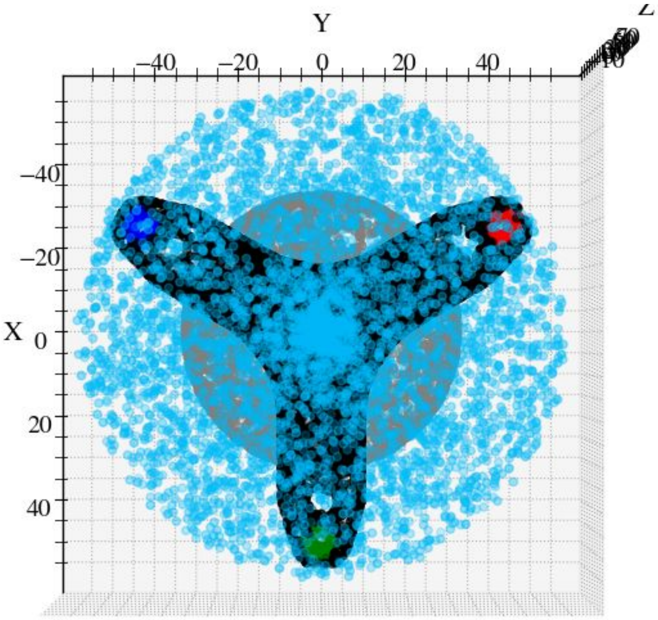

Figure 5.2: Geant4 simulation geometry used for the Kr sims. The sky blue points are a subset of the Kr primaries, gray shows the passivated surface of OPPI, black shows the Mercedes piece, and red/green/blue shows the copper support rods. Not pictured but accounted for in the simulation are the copper contact pin and the copper IR shield surrounding the setup.

5.1.3 Kr Decay Scheme

We were not able to find a reliable $^{83\mathrm{m}}$Kr decay scheme within G4 so we adapted the g4simple code to take in decay information in the HEPEVT format. Kr decays were generated by code written by a UW undergraduate at the time, Josh Kaler. This code uses NuDat [116] and results from a

KATRIN study [125] to generate individual Kr decays based off the energy levels and intensities of the decay products. We generate a large number of decays (for the final simulation, 2.5×10^7 decays) and put them all into HEPEVT format. This contains information about the decay products such as event number, particle type, momenta, energy, position, time, etc. We assume that the momenta of ejecta are isotropic; angular correlations are not considered. We also filter out events that would start inside of one of our G4 geometries. Once we have all this information, we save it in a .txt file to which our g4simple has access. We run the simulation using the "Shielding_EMY" physics list (which accounts for hadronic interaction models and, more importantly for our simulation, low-energy electromagnetic interactions) and produce .hdf5 output files. The energy spectrum we input into G4 is shown in Figure 5.3 and the resulting G4 output energy spectrum before any post-processing is shown in Figure 5.4.

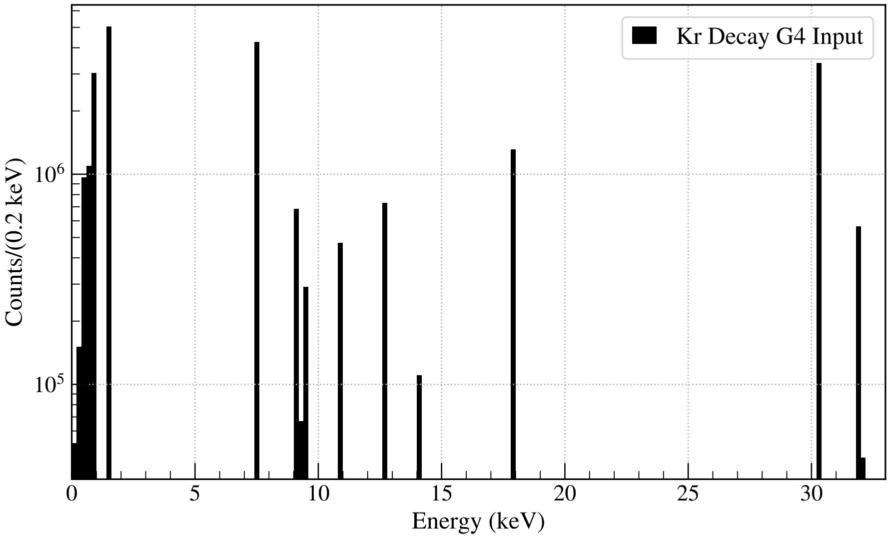

Figure 5.3: $^{83\mathrm{m}}$Kr decay products inputted into Geant4.

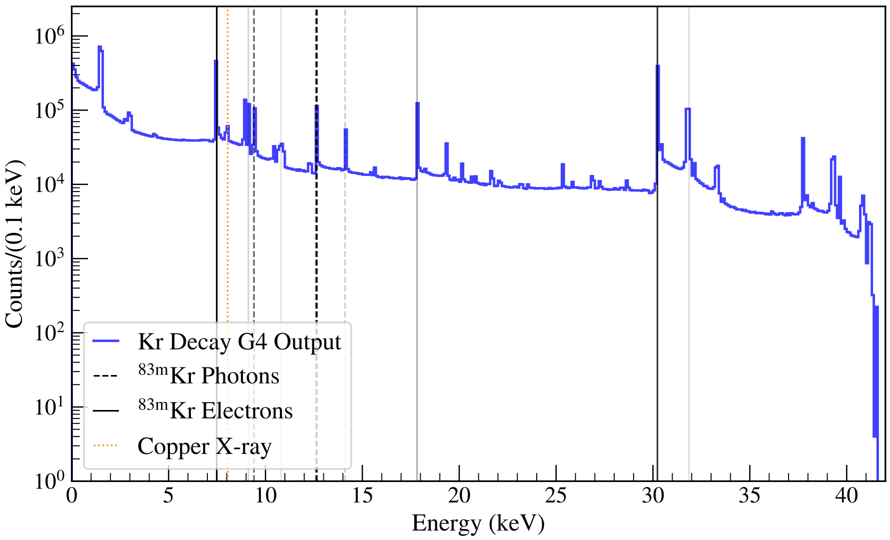

Figure 5.4: Geant4 simulated krypton spectrum with no post-processing. Also plotted are the ^{83m}Kr decay photons (electrons) with their opacity scaled by relative intensity compared to other photons (electrons). We see all the expected peaks as well as a number of summed peaks from the two-level decay scheme.

5.2 siggen Simulation

In tandem with the G4 particle simulation we must try to model this incomplete charge collection in our detector through a pulse shape simulation. For this we use the siggen simulation package [64]. Inputs for this simulation are the detector geometry, impurity profile of the detector, surface charge on the detector, detector bias, and other configuration parameters.

5.2.1 CV Curve and Impurity Profile

The impurity profile of OPPI was not known prior to simulation. Much like the detector geometry we had to make measurements to approximate these values. The impurity profile will impact the capacitance of the detector, so we can make a measurement of the detector's CV curve and estimate the impurity profile from there.

The CV curve measurement consists of a square pulse of known amplitude from a signal generator sent into our high voltage (HV) filter box which pulses the HV ring connected to the detector's n+ surface. We measure the amplitude of the first stage output of this pulse on an oscilloscope. We then use the fact that charge ought to be conserved along with the definition of capacitance to assert that

$$C_{\text{eff}} = C_{\text{f}} \left(\frac{V_{\text{out}}}{V_{\text{in}}} \right) \tag{5.1}$$

where C_{eff} is the effective capacitance of the detector, $C_{\text{f}} = 0.1$ pF is the feedback capacitance of the front-end board (see Section 4.2.2 for circuit details), and $V_{\text{out(in)}}$ is the output (input) voltage. This capacitance measurement is shown in Figure 5.5.

The impurity profile will impact the CV curve as it is essentially an excess of charge distributed through the detector to shape the electric field and change the shape of the depleted region at a given voltage. This impurity profile at its simplest consists of a net impurity concentration at $z = 0$ (at the passivated surface), measured in electrons/cm^3, and an impurity gradient, measured in electrons/cm^4. There is evidence of a radial dependence in these impurity values [126] but that was not modeled. An undergraduate working at UW, Jason Diao, ran a grid search of different impurity values using the SolidStateDetectors.jl simulation package [127] and ran a chi-squared test to determine the impurity profile that provided the best-fit to our CV curve data. There was an overall multiplicative factor between the final capacitance measurements between data and simulation which was scaled down. The capacitance of the detector is very sensitive to the geometry of the $p+$ point contact. This geometry depends on exactly where the boron is implanted into the contact which is an unknown. The field inside the detector is insensitive to this shaping, and so the uncertainty in that boron implantation, to first order, provides some overall scaling of the capacitance. We are thus able to find a good fit to the data up to some overall constant scaling. The comparison between simulation and data is shown in Figure 5.5.

The value of the impurity concentration at $z = 0$ that we get from Jason's simulation is expected to be a combination of the true intrinsic impurity value at that position and any additional external surface charge. This is simply a rough approximation and can likely be refined in future simulations. We then use Equation (5.2)

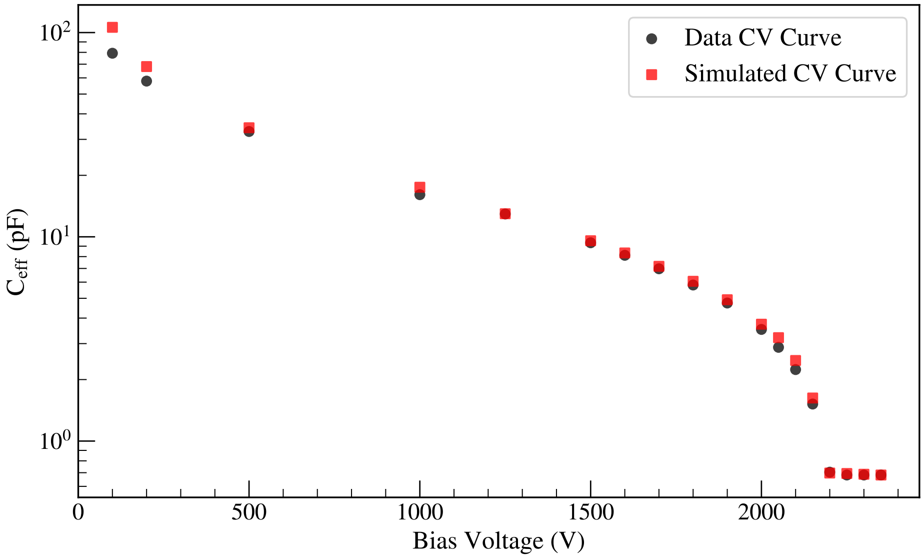

Figure 5.5: OPPI CV curve from data and simulation. The simulation overestimated the capacitance and CV that we found in data by a factor of 2.9; this was scaled down to match the data curve. The impurity values we find for this sim are $\Sigma\left(\rho(z=0)\right) = -1.147 \times 10^{10}$ e/cm^3 and $\Delta\rho = 1.1 \times 10^9$ e/cm^4. The detector depletes around 2200 V.

$$-1.147 \times 10^{10} \mathrm{e/cm}^3 = \sigma/z_{\mathrm{det}} + \rho(z=0) \tag{5.2}$$

5.2.2 Weighting Potential

We seek to calculate signals generated from ionization events at various positions in our detector. The equation, Equation 2.2 and Equation (5.3), that governs the calculation of these signals comes from the Shockley-Ramo theorem, as discussed in Section 2.3.2.

$$Q = q_{\mathrm{drift}} \Delta\varphi_0 \tag{5.3}$$

The first component of this equation we consider is the weighting potential. The weighting potential is independent of surface charge and any impurities in the detector and is purely a geometric solution to Laplace's equation. Siggen solves this through an over-relaxation method. The weighting potential of OPPI is shown in Figure 2.4.

5.2.3 Surface Charge and Electric Field

The amorphous germanium passivated surface is an insulating surface. This means that free charges inside the cryostat can collect on that surface. This will distort the electric field inside the crystal and thus change the drift paths of charge carriers created during ionization events. Of specific importance is that a surface charge will attract oppositely charged carriers to the passivated surface. The mobility of these charge carriers is vastly reduced on the passivated surface and in this thesis is not considered to contribute to the waveform. This means that for a negative (positive) surface charge, holes (electrons) will drift towards the passivated surface and will stop contributing to the amplitude of the signal when they reach the surface. This leads to energy degradation and a partially inactive region forming in the detector where charge carriers are susceptible to the electric field added by the surface charges. The changing pressure at cooldown (discussed in Section 4.5.1) is expected to lead to different partial pressures of residual gas species that condense on detector and near-detector surfaces. We believe this difference in concentration of condensing gasses changes the surface charge distribution.

We show the difference that surface charge makes on the electric field inside the detector in Figure 5.6.

These electric fields, as well as all other simulations in this thesis, were calculated on a (0.02 × 0.02) mm^2 grid. This was the smallest possible grid we could use in our siggen simulations and may be a source of uncertainty at distances very close to detector surfaces.

5.2.4 Surface Charge and Energy-Degraded Regions

The sign and magnitude of the surface charge will greatly affect the dead layer that is generated near the passivated surface. We can run a siggen simulation with ionization events placed throughout the detector on a grid. The simulation assumes that only one electron-hole pair is created at that location—we can scale the amplitude of the signal by however much we want in post-processing. The simulation will calculate the electric field given that surface charge and drift the hole (electron)

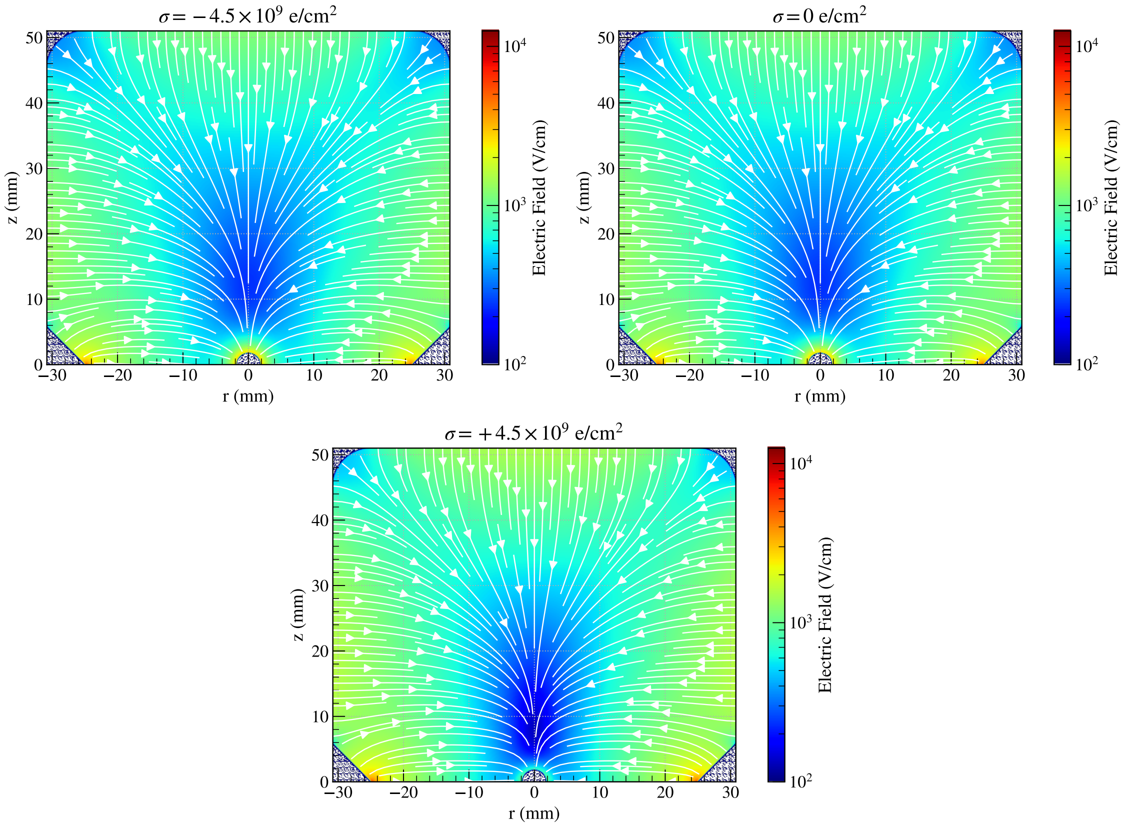
$\sigma = -4.5\times10^9$ e/cm^2

$\sigma = 0$ e/cm^2

$\sigma = +4.5\times10^9$ e/cm^2

Figure 5.6: OPPI electric fields for different surface charges at $V_{\text{bias}} = 2700$ V.

through the detector towards the $p+$ ($n+$) contact. This drift is affected by not only the electric field but also the charge carrier mobilities and crystal axes, as described in Section 2.3.2. A standard drift path with and without surface charge is shown in Figure 5.7 and the resulting waveforms are shown in Figure 5.8. To calculate these waveforms we apply Equation (2.2) and stop charge collection once a charge carrier reaches the passivated surface.

Once the siggen simulation is run and we calculate waveforms at different locations in the detector, we can determine the energy-degraded region in the detector. We take the amplitude of the resulting signal at some position as the fraction of energy degradation we see at that point in the detector. We show the resulting energy-degraded regions for negative and zero surface charge in Figure 5.9. These simulations have good agreement with those in a similar study from [128].

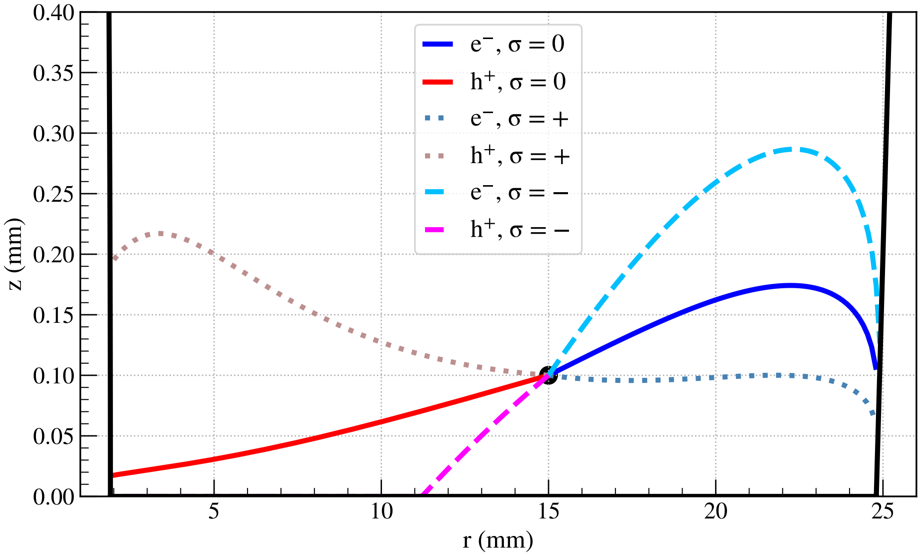

Figure 5.7: Charge carrier drift paths, with/without surface charges

Clearly negative surface charge generates the largest energy-degraded regions (note that "dead layer" is not an apt name for this since there are regions of partial charge collection, the region is not completely "dead;" a potential acronym stand-in is the "Edge of Activeness in Germanium for Low Energy Surface events", or EAGLES[1] but I will mostly refer to it as an "energy-degraded region"). This is due to the fact that our signals are "hole-dominated," a consequence of the rapidly changing weighting potential near the $p+$ point contact. Given the scale of energy degradation we see in the KrSTC dataset, we assert that the surface charge on the detector must be negative. A positive surface charge is not viable for our data, and we are not able to keep increasing the positive surface charge without it affecting the depletion and biasing of our detector. There is a limit (according to simulations) to how much surface charge you can apply to these surfaces. Another aspect of the inviability of a positive surface charge for our model comes from the significant active region along the passivated surface around r = 17 mm in Figure 5.9. This large active region would result in electrons depositing energy in active regions and appearing as peaks in our data, a phenomenon we

---

[1] Go Birds

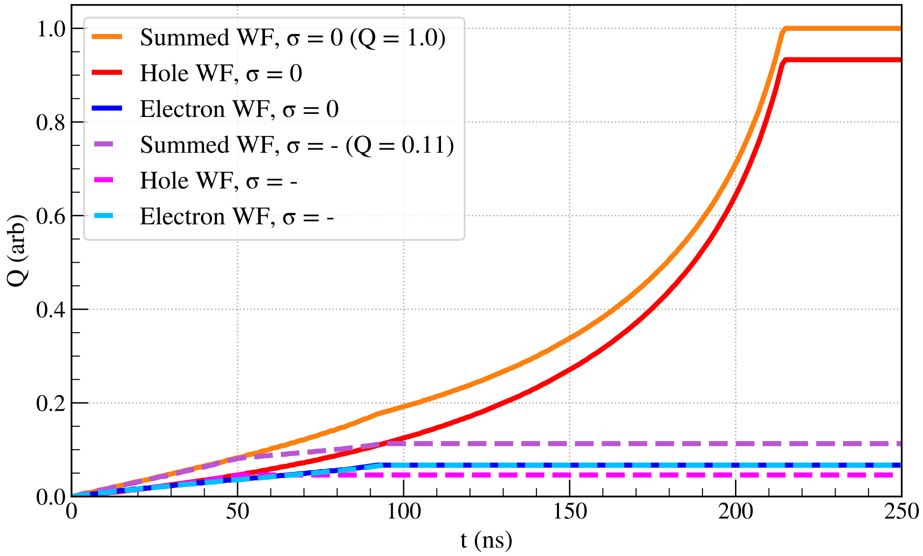

Figure 5.8: Simulated hole and electron waveforms for drift paths in Figure 5.7. The positive surface charge is not shown here as it overlaps with the case with no surface charge. The hole waveform in the negative surface charge case is very degraded.

do not see.

Note that we also call these energy-degraded regions "elephant ears" due to their appearance on a linear z scale. This helps distinguish the surface charge-induced energy-degraded region from other dead layers in the detector.

5.2.5 Drift Path Angular Dependence of Energy-Degraded Region

As we discussed in Section 2.3.2, there is an angular dependence on the mobility of the charge carriers. This leads to a difference in the energy degradation of events that travel in different angular directions in the detector, making this a three-dimensional problem. The effect is not large but is noticeable. The activeness contours of two different simulated angles are shown in Figure 5.10.

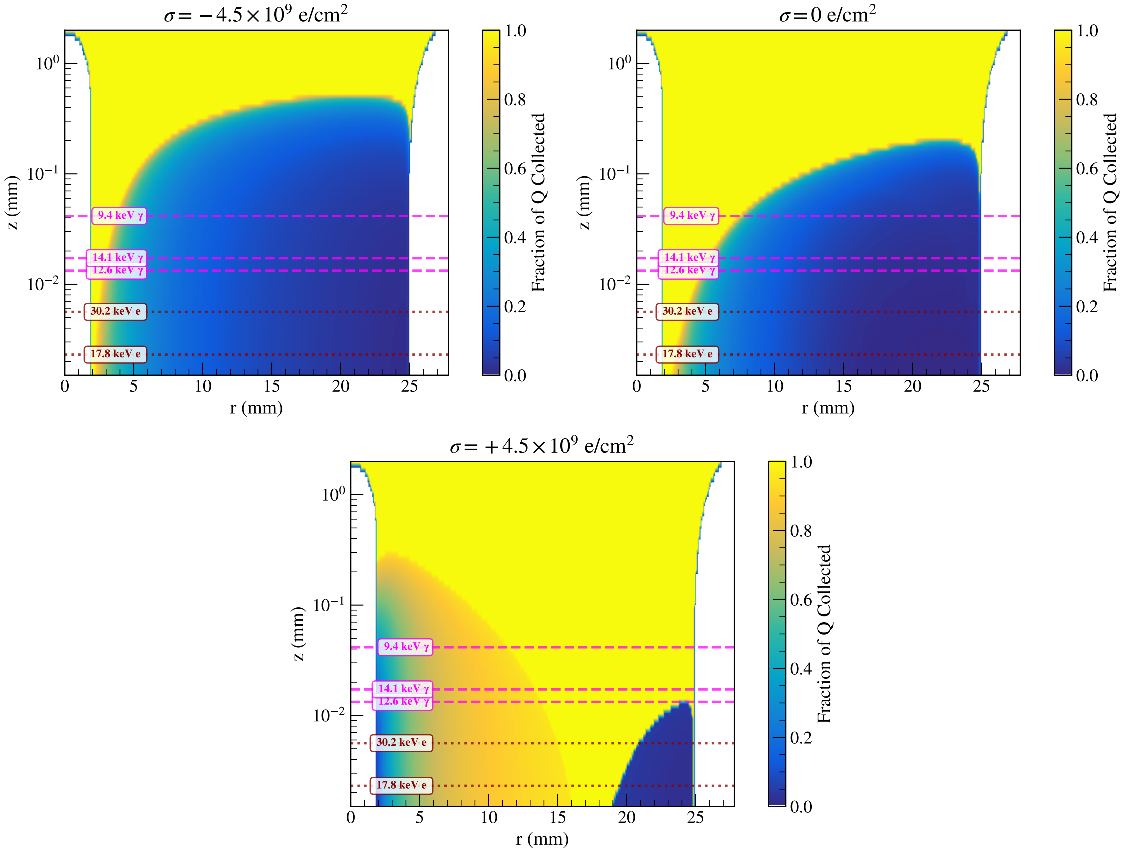

Figure 5.9: Simulated energy-degraded regions for different surface charges (positive surface charge required $V_{\text{bias}} = 2600$ V, others at $V_{\text{bias}} = 2400$ V). All energy-degraded regions are shown at $\theta = 0$ and major $^{83\text{m}}$Kr decay product penetration depths are shown.

5.3 Results and Data vs. Simulation

5.3.1 Final Spectrum Comparison

There are a number of (somewhat degenerate) parameters in the G4 and siggen sims as well as in our analysis that we can tune to best match our simulated spectrum with the data. For parameters that we have an idea of their scale (such as the $n+$ and $p+$ dead layers) we try to stay within a reasonable range of those expectations. Other parameters are considered mostly on how they affect the final simulated spectrum and its comparison to data. In Section 5.3.2 we will discuss the most

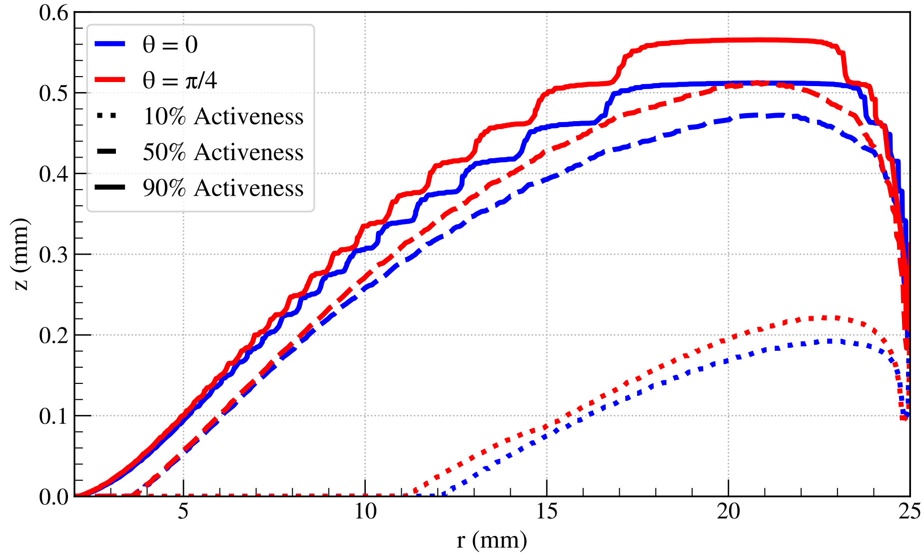

Figure 5.10: Angular dependence of energy-degraded regions, showing three activeness contours for two angle values. The effect is periodic in θ with $(0, \pi/4)$ being the boundaries of that periodicity.

relevant simulation and post-processing parameters. We will see how variations in these parameters affect the simulated spectrum and what that can tell us about our surface-charge model. First, we start with our best match between simulation and data.

Simulation and data appear to match very well. In optimizing the simulation parameters we focused on matching the degraded electron spectrum in the region 18 keV $\lesssim E \lesssim$ 30 keV as well as the photon peaks. There is some very slight disagreement in that electron continuum as well as some difference at low energies below the photon peaks, the latter possibly due to a mis-modeling of the energy threshold function applied to simulation. The threshold function applied is:

$$f_{\text{thresh}}(E) = \frac{1}{2}\left(\text{erf}\left(\frac{E - E_{\text{midpoint}}}{\sigma\sqrt{2}}\right) + 1\right) \tag{5.4}$$

where $E_{\text{midpoint}} = 4.5$ keV and $\sigma = 0.6$ keV.

The final simulated spectrum and its comparison to data is shown in Figure 5.11. The elephant ear used for this simulation is shown in Figure 5.12 and the key simulation parameters are shown in Table 5.1.

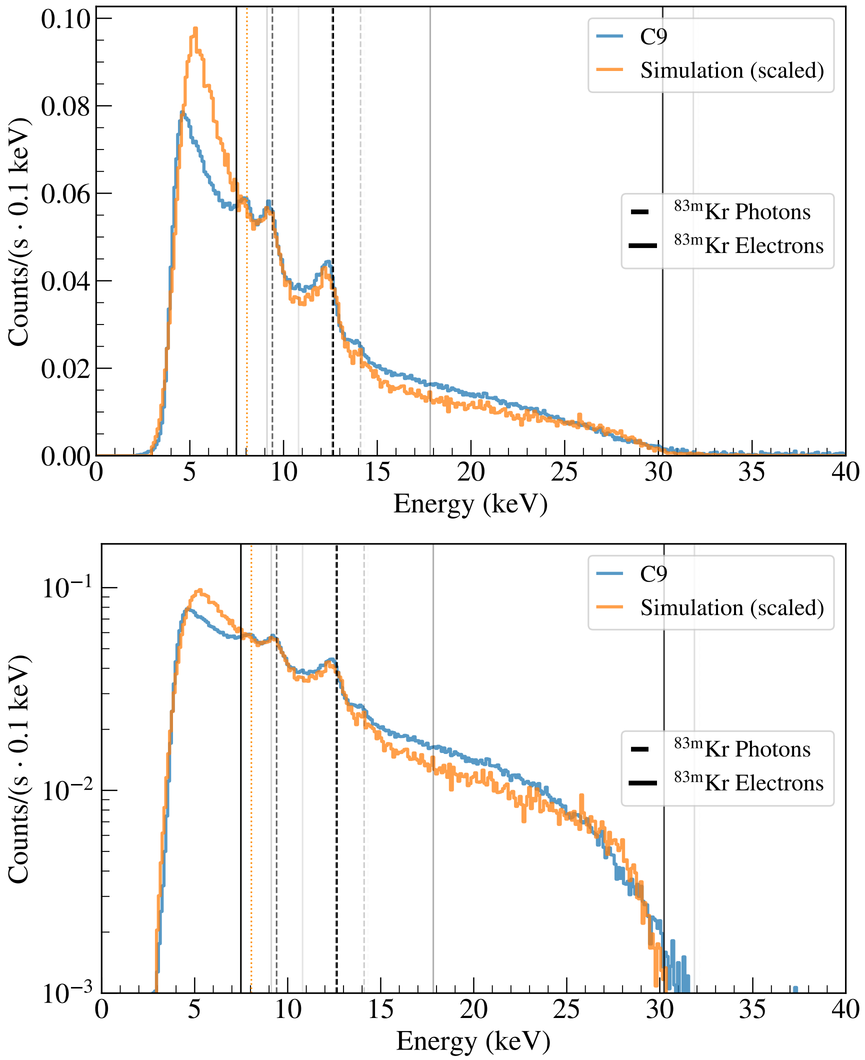

Figure 5.11: Final simulated spectrum compared to wet detector KrSTC data (C9), shown in (*top*) linear and (*bottom*) log scale.

Note that only one wet detector campaign (C9) is shown in the comparison to simulation in Figure 5.11. This is the highest krypton rate we achieved with KrSTC and was most of the focus for matching simulation and data. We could match simulations to our other wet detector spectra at

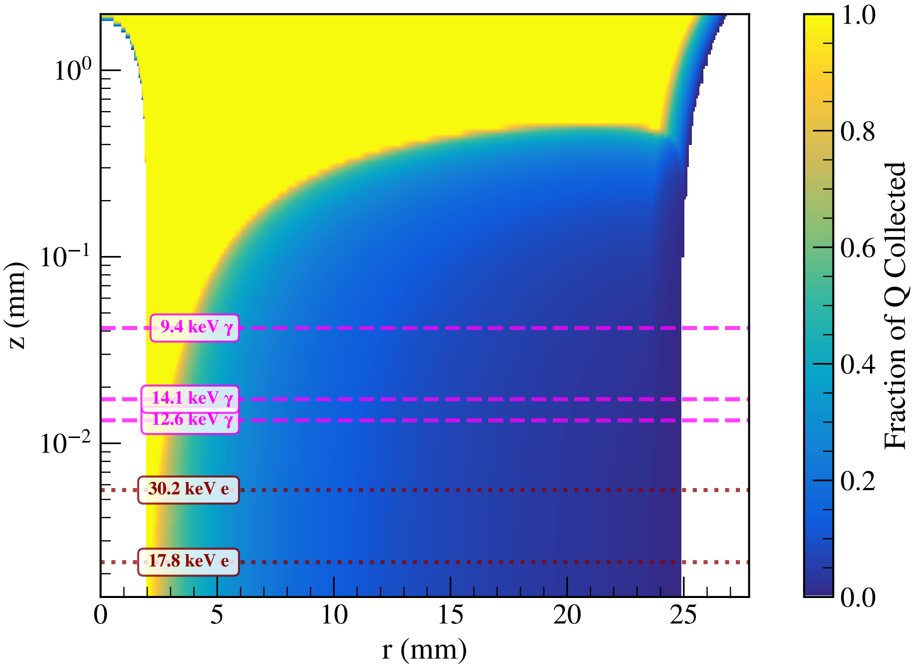

Figure 5.12: Final simulation elephant ear with parameters from 5.1, for just $\theta = 0$. Shown as well is the $n+$ dead layer (other dead layers are too small to plot) and the penetration depths of some major decay products.

least qualitatively, but this did not significantly further our understanding. Dry detector behavior was not fully matched with simulation; this will be discussed in Section 5.4.

5.3.2 Different Parameters and Dead Layers

We can consider the effects that variations in the major tunable simulation parameters can have on the resultant simulated spectrum. This helps guide the values we choose for these parameters. We abbreviate dead layers in this section as DL.

Due to the fact that the Kr source is diffuse in the cryostat, normalizing simulation to data across different campaigns and with different parameters is very difficult. The method we apply here is to consider the spectra in Figure 5.11 to be "matched" and use the scaling applied to that

Parameter	**Symbol (Units)**	**Value**
Surface Charge	σ (e/cm^2)	-4.5×10^9
Impurity, $z = 0$	ρ_{z_0} (e/cm^3)	-1.06×10^{10}
Impurity Gradient	$\Delta\rho$ (e/cm^4)	1.1×10^9
Angles Simulated	θ (rad)	$\left(0, \frac{\pi}{12}, \frac{\pi}{6}, \frac{\pi}{4}\right)$
Bias Voltage	V_{bias} (V)	2400
$n+$ DL Length	ℓ_{n+} (mm)	1
$p+$ DL Length	ℓ_{p+} (μm)	0.5
PS DL Length	ℓ_{PS} (μm)	1
Energy Resolution	σ (keV)	0.45

Table 5.1: Major simulation parameters for final Geant4 and siggen sims. Parameters were chosen to match simulation and data spectra by eye.

“final” simulation as a reference in all other simulation plots. That scaling is a simple multiplicative constant applied to match the integrals of the data and simulated spectra.

In the legends of the spectra plots in this section you will see “Simulation (scaled by $1/n$)” with n being the factor by which we reduce the “final” simulation in Figure 5.11. For example, in Figure 5.13, “Simulation (scaled by 1/23.7)” indicates that only removing the $n+$ dead layer from the simulation grows the integral of that spectrum by a factor of 23.7. We then scale that spectrum down to match the integral of the data. For $n < 1$ the parameter change caused the simulation counts to go down, so in that case we scale up that simulated spectrum.

$n+$ ***Dead Layer***

We know to expect a $\mathcal{O}(1\text{ mm})$ DL extending from the $n+$ surface. This DL is also expected to grow [129] over time as we are not keeping the detector cold during inactive periods. After years of sitting at room temperature, OPPI’s $n+$ DL is expected to be growing very slowly at this point. However, our simulation is insensitive to changes in the $n+$ layer size as none of our decay products can penetrate that deep into the detector. Our $n+$ DL model (taken from some standard values proposed by [72]) and the resulting simulated spectrum when that DL is removed is shown in Figure 5.13..

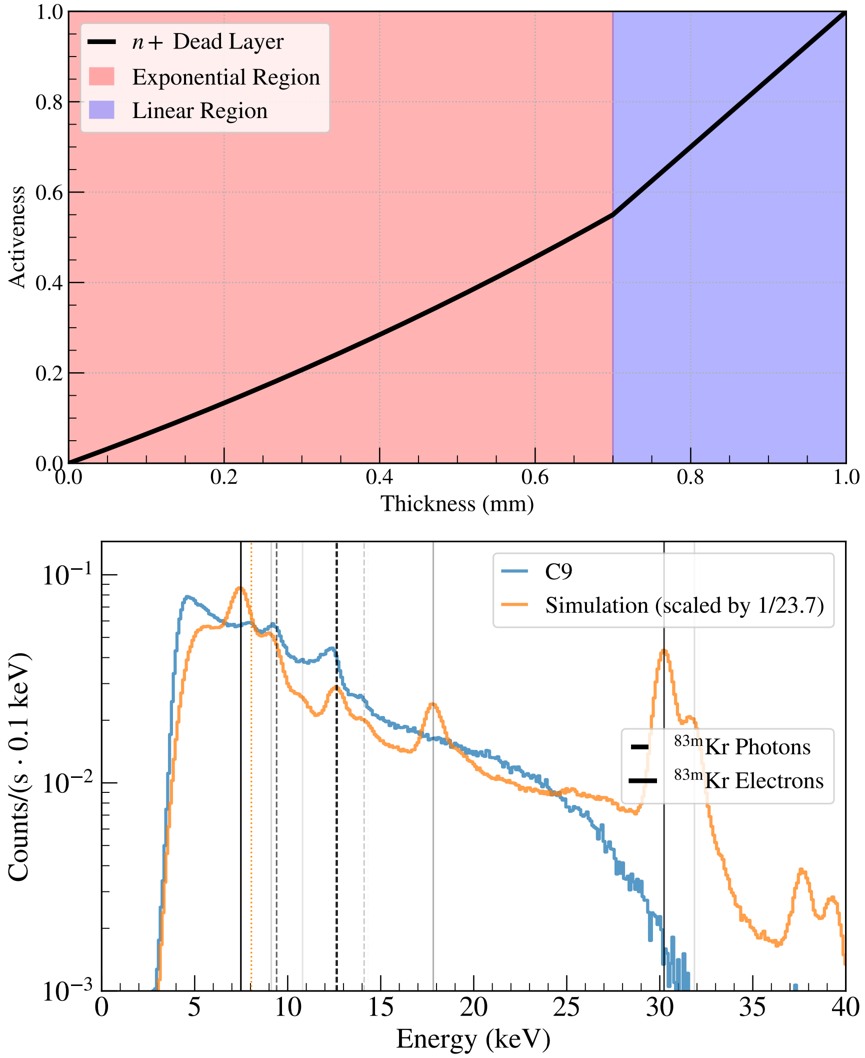

Figure 5.13: $n+$ DL model (*top*) and effect when removed on simulated spectrum (*bottom*). The parameters used for the DL are: $x_t = 0.7$ mm (thickness of the exponential region), $f = 0.55$ (the activeness at that exponential/linear interface, and total thickness = 1 mm.

Clearly we need an $n+$ DL to get good agreement between our spectra. Without it, the higher intensity electron lines begin to dominate the spectrum. All of our DLs need to be able to degrade electron lines at least a little bit.

$p+$ ***Dead Layer***

The $p+$ point contact is made by implanting boron onto the surface of the hemispherical point contact. We expect a DL in this region of about 0.3 μm [130] (increased to 0.5 μm to yield a better match between simulation and data, particularly at the 30 keV kryptond decay endpoint). This DL extends hemispherically out from the contact—we model the contact as a hemispherical shell with boron implanted uniformly along that shell. There is a question of whether the entire point contact is implanted, as we will discuss in Section 5.3.2. An exaggerated $p+$ DL and spectra from no DL and a larger, 5 μm DL are shown in Figure 5.14.

The primary effect of changing this DL is on the electron continuum near 30 keV. It is possible that this is not a fully DL like the $n+$ transition region, but we expect this region to be sharply defined by the well-controlled ion implantation depth and feel it is reasonable to model it as a fully dead region. We also model the point contact as not fully implanted in Section 5.3.2.

Passivated Surface Dead Layer

We also expect a dead region at the passivated surface (PS). The passivated surface is of unknown material and formation. It may be generated from sputtering amorphous germanium or silicon on the detector. Regardless, we expect this dead layer to be roughly 1μm in size [131]. We again show an exaggerated dead layer and results from changing that dead layer in Figure 5.15.

This dead layer changes the higher energy electron continuum quite a bit. This may give a hint that the key to recreating a spectrum like C22 is deadening the region where the $p+$ point contact meets the passivated surface.

Diffusion

more accurately, we have assumed that every e-h pair follow a single trajectory determined only by the E field and the mobility tensor.

So far we have assumed that energy depositions create one electron-hole pair and that those

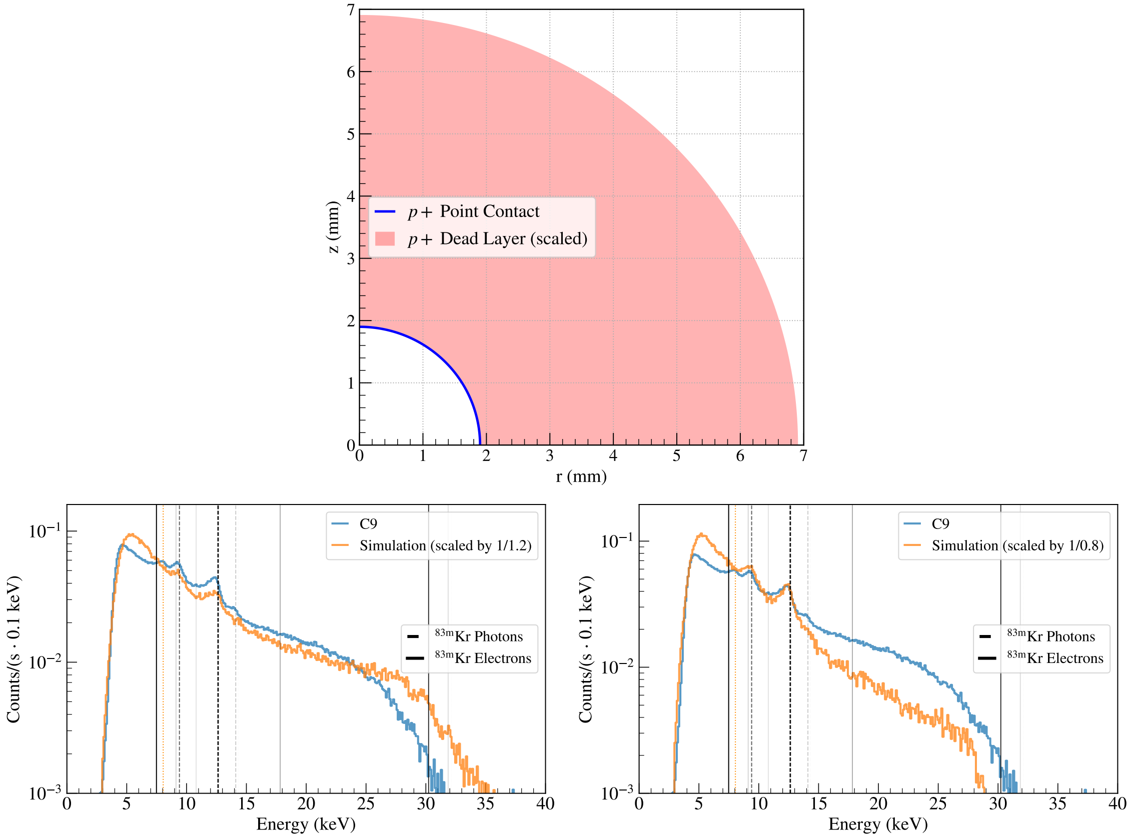

Figure 5.14: $p+$ DL model (*top*, size exaggerated) and effect on simulated spectra (*bottom*). With no $p+$ DL (*bottom left*) we see the electron continuum extend past $\sim$ 30 keV which begins to wash out the photon peaks. With a 5 μm DL (*bottom right*, factor of 10 increase from the "final" simulation), you start to lose those lightly degraded higher energy electrons as they are fully degraded. A 0.5 μm-length DL puts the simulated spectrum endpoint near 30 keV, consistent with the data.

charge carriers follow a single trajectory through the detector, determined only by the electric field and the mobility tensor. In reality, it takes $\sim$ 3 eV on average to create 1 e-h pair, so a 3 MeV energy deposition would generate 1 million e-h pairs. This charge cloud is subject to dynamics such as diffusion in the detector. As a very crude diffusion model, we use the equation

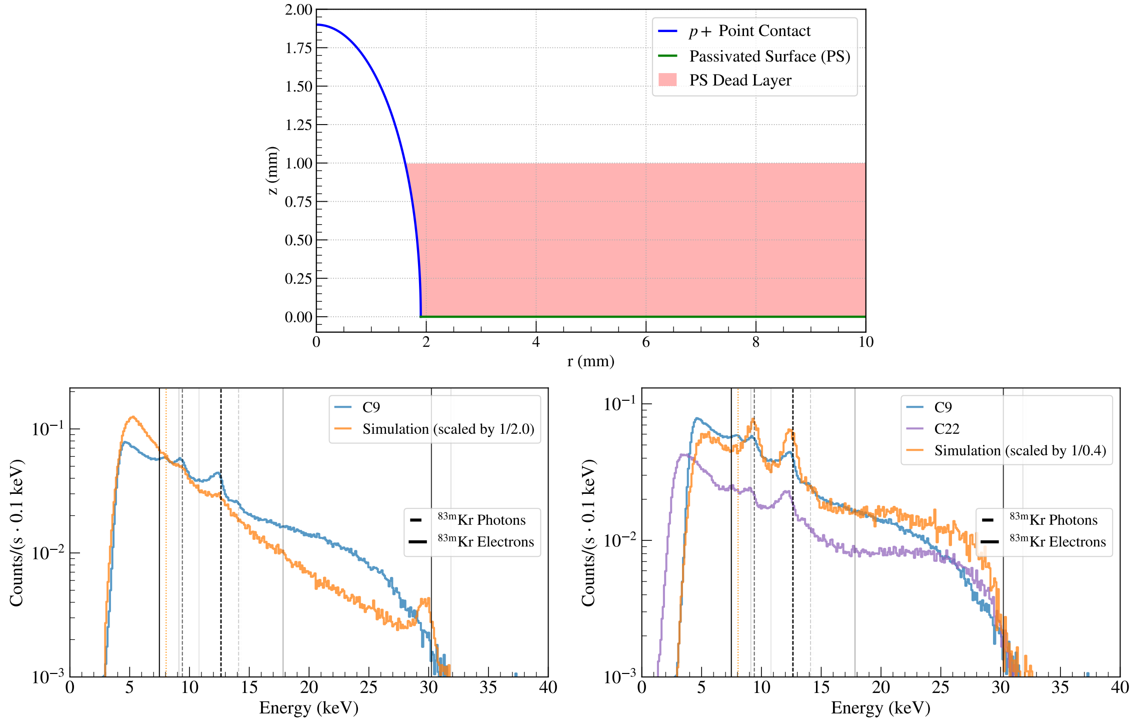

Figure 5.15: Passivated surface (PS) DL model (*top*, size exaggerated) and effect on simulated spectra (*bottom*). Removing the PS DL (*bottom left*) starts to resolve the $\sim$ 30 keV electron peak which we do not see in data. With a 5 μm PS DL (*bottom right*, factor of 5 increase from the "final simulation"), we start to see a shelf-like higher energy electron spectrum which is more reminiscent of C22. In this case, the photons are more resolved.

$$r_{\text{diff}} = \sqrt{2D_i t} \tag{5.5}$$

where r_{diff} is the radius of the spherical charge cloud, D_i is the diffusion coefficient of the charge carrier ($D_h = 0.0265 \cdot \left(\frac{77\text{ K}}{90\text{ K}}\right)\text{mm}^2/\mu\text{s}$ and $D_e = 0.0332 \cdot \left(\frac{77\text{ K}}{90\text{ K}}\right)\text{mm}^2/\mu\text{s}$) [132], and t is the drift time in μs. At each time point we measure the ratio of the volume of sphere subtended by the passivated surface to the full volume which is the amount of charge we degrade at that point. This is a very naive model, as the charge cloud will self-repel and distort under influence of the electric field, but this should give us a rough estimate of how impactful diffusion is. The diffusion model we use is shown in Figure 5.16 and the effect on the elephant ears and spectra is shown in Figure 5.17.

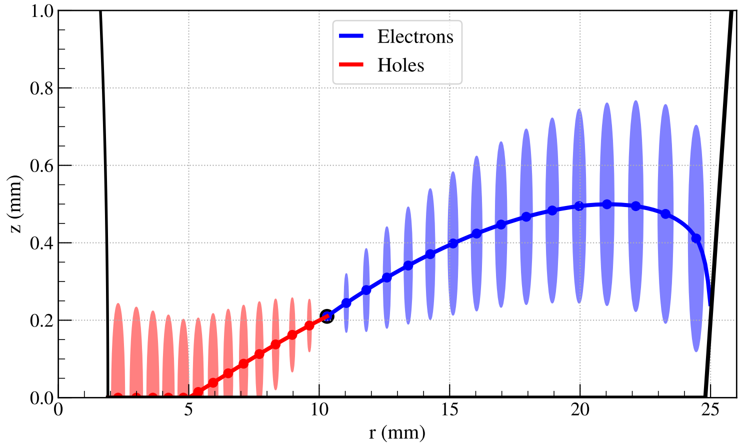

Figure 5.16: Diffusion model used in simulation. The model consists of a single energy deposition at the plotted black dot, with each point on the scatter plot corresponding to different time steps along the trajectory. The circles surrounding those scatter points represents the size of the charge cloud at each time point.

Diffusion does not have a large effect on our simulation. The holes in the simulation are affected the most by diffusion and they are already losing most of their charge to the passivated surface in the energy-degraded region. Smearing that energy-degraded region out slightly does not change the spectrum significantly. It does have an impact on the prominence of the gamma peaks and it is possible that the resolution of those gamma peaks at low energy is some combination of energy resolution and diffusion, but in this case we do not need to differentiate between the two and do not apply diffusion to our final simulation.

Energy Resolution

We measured the energy resolution of our OPPI detector, shown in Figure 4.19. We can apply this energy resolution equation to our simulated spectrum to see if there is good agreement between the photon peak resolutions, as shown in Figure 5.18.

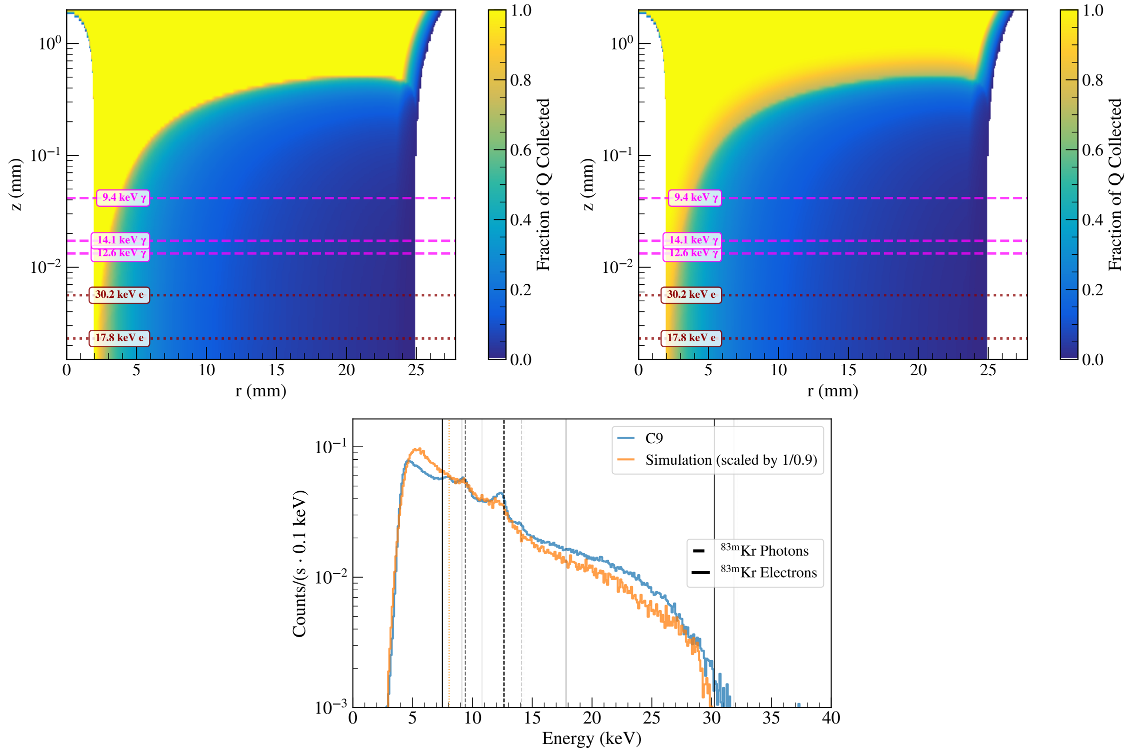

Figure 5.17: Diffusion effect on elephant ears (*top*) and simulated spectra (*bottom*). The elephant ear with diffusion (*top right*) differs from its diffusion-less counterpart (*top left*) in the region between the energy-degraded region and active bulk, with a "fuzzy" slightly degraded region in between the two. The effect on the spectrum (*bottom*) is noticeable but not unexpected when also combined with detector resolution effects and mostly serves to smear the spectrum in tandem with the energy resolution.

The data energy resolution matches quite well when applied to the simulation. There is a slight difference and we apply a larger energy resolution to our final simulation. The discrepancy there is likely due to the fact that we optimize our energy estimators on high energy peaks, not low energy peaks. We also cannot measure our energy resolution down near the krypton region energies due to a lack of low energy photon peaks in our background data. However, this is good confirmation that our energy resolution function is fairly accurate.

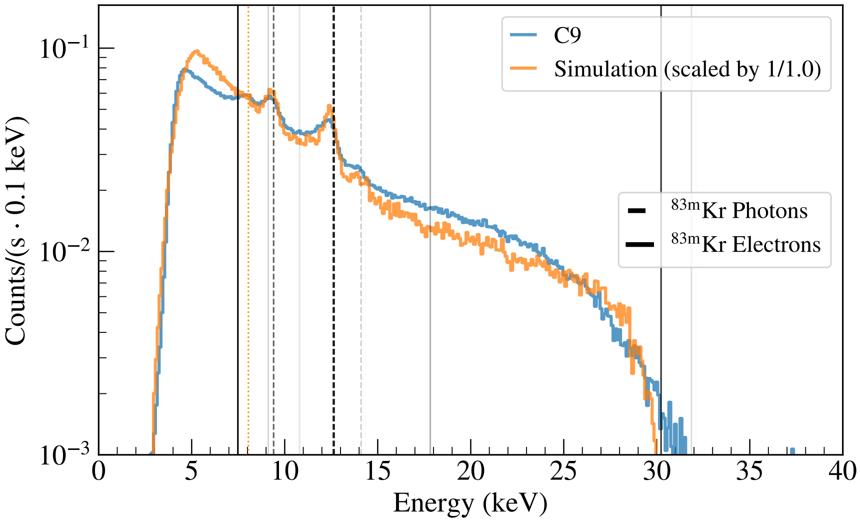

Figure 5.18: Data energy resolution applied to simulation, which provides a nice match between data and simulation. In our final simulation we increase resolution a bit.

For the following subsections, to reduce simulation time and file size, we limit the siggen simulations to only consider events with $r < 15$ *mm and* $\theta = 0$*. This does not noticeably change the final simulation spectrum with all other parameters kept the same as Table 5.1, as shown in Figure 5.19.*

Bias Voltage

Due to fear of increased leakage current, we operated OPPI during wet detector campaigns between 2400-2500 V. One of our early hypotheses to explain the wet/dry detector question was that the operating bias voltage was affecting the spectrum. We tested and ruled out this hypothesis in data, and confirm this by operating a wet detector simulation at 2700 V instead of 2400 V, as shown in Figure 5.20.

The higher bias voltage only serves to slightly increase electric field strength in the germanium, and so the DL will shrink by a tiny amount and thus affect the highest energy electrons in our spectrum. We anticipate a similar effect here as we do in lowering the surface charge.

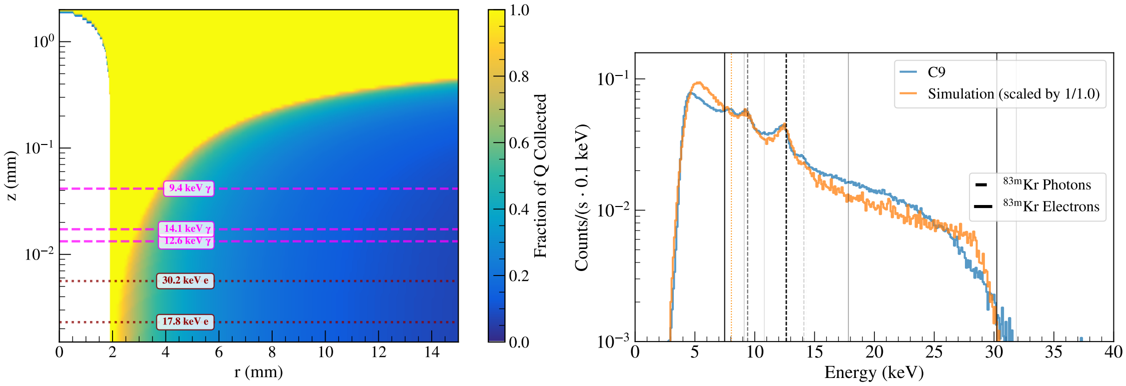

Figure 5.19: Elephant ear (*left*) and final simulation spectrum (*right*) with r < 15 mm, $\theta = 0$. There is no significant difference from Figure 5.12 and Figure 5.11.

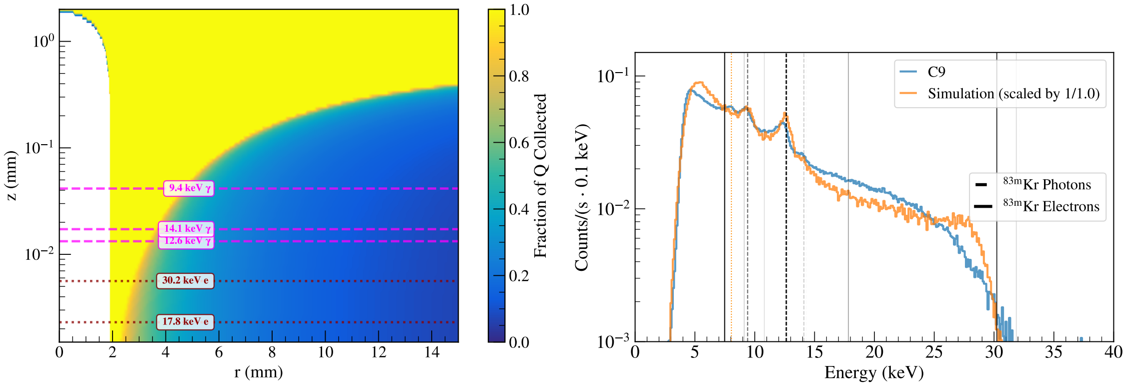

Figure 5.20: Elephant ear (*left*) and final simulation spectrum (*right*) with $V_{\text{bias}} = 2700$ V. There is no significant difference aside from a slight sharpening of the electron continuum near 30 keV.

Changing Surface Charge

We can consider changes to the surface charge and how that can affect our elephant ears. In this study, we only change the magnitude of the negative surface charge while keeping the impurity profile the same. This is different from our model based on the CV curve measurement in Figure 5.5, but it will highlight the effect that a changing surface charge will have on the elephant ear and simulated spectra. We consider no surface charge in Figure 5.21, a smaller surface charge in Figure 5.22 and a larger surface charge in Figure 5.23.

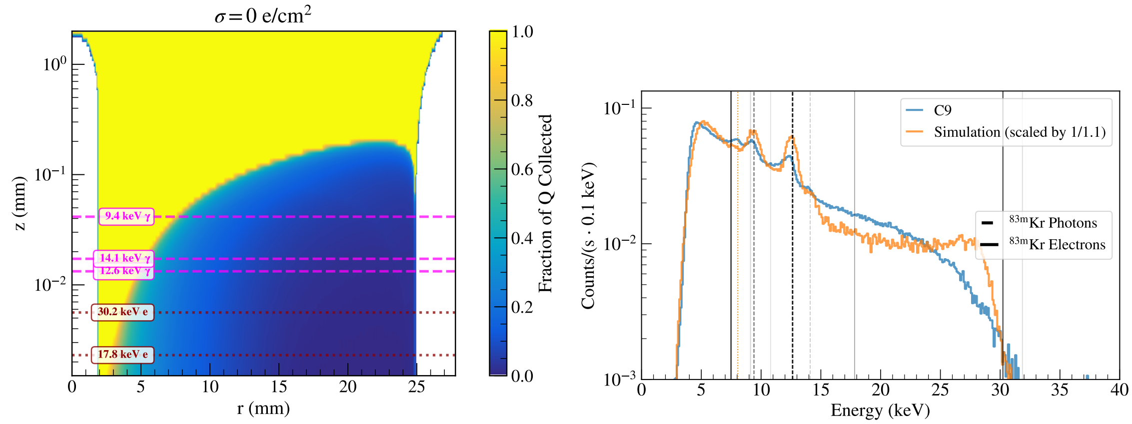

Figure 5.21: Elephant ear and final simulation spectrum with $\sigma = 0$ e/cm^2. This spectrum is not far from our final spectrum but with a sharper electron continuum near 30 keV and more prominent photon peaks.

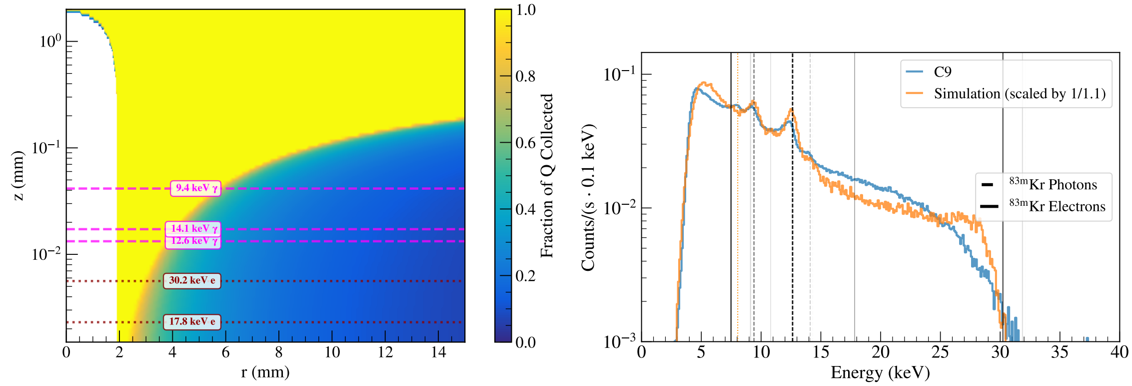

Figure 5.22: Elephant ear and final simulation spectrum with $\sigma = -1 \times 10^9$ e/cm^2, a factor of 4.5 smaller than the final simulation. There is no significant difference in the spectrum aside from a slight sharpening of the electron continuum near 30 keV.

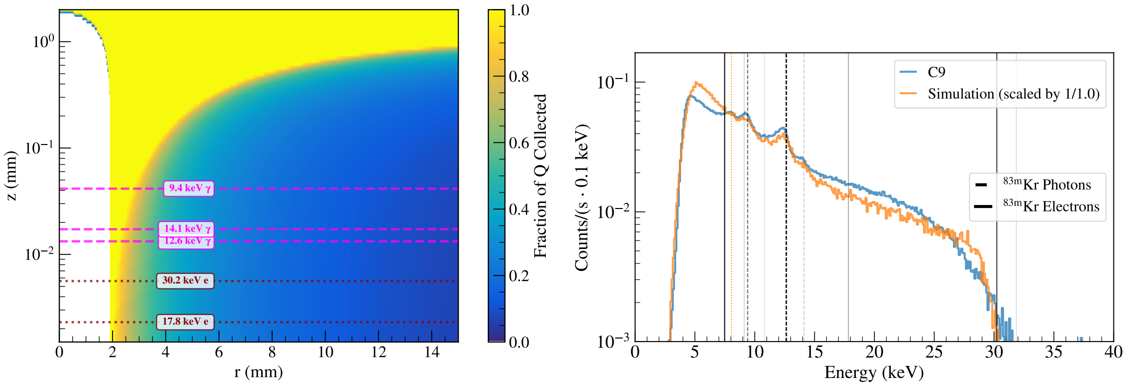

Figure 5.23: Elephant ear (*left*) and final simulation spectrum (*right*) with $\sigma = -1 \times 10^{10}$ e/cm^2, a factor of 2.2 larger than the final simulation. There is no significant difference in the spectrum aside from a slight smearing of the electron continuum near 30 keV.

Applying zero surface charge gives us a simulated spectrum not too far from our data but there are clear differences that motivate us to pursue some negative surface charge. Changing the magnitude of a negative surface charge does not significantly change the simulated spectrum. This is the case primarily because we find a fairly large impurity profile value at $z = 0$ of -1.06×10^{10} e/cm^3, as compared to surface charges of $\sim -10^9$ e/cm^2. If this impurity profile was smaller, a larger surface charge would have a larger effect on the spectrum. As is the case with positive surface charge, there is a limit to how much charge you can place on the passivated surface before the detector depletes at extreme voltages, does not deplete at all, or you get discharges.

Impurity Profile

Here we lower the impurity value at $z = 0$ and the impurity gradient across the detector by a factor of 0.8. This causes the detector to deplete around 1700 V which is far from our typical 2200 V depletion voltage. The resulting elephant ear and simulated spectrum are shown in Figure 5.24.

Changing the impurity profile mimics the change we see in the case of less surface charge, which is to be expected. In our approximation there is no difference between surface charge and impurity-based charge at the passivated surface.

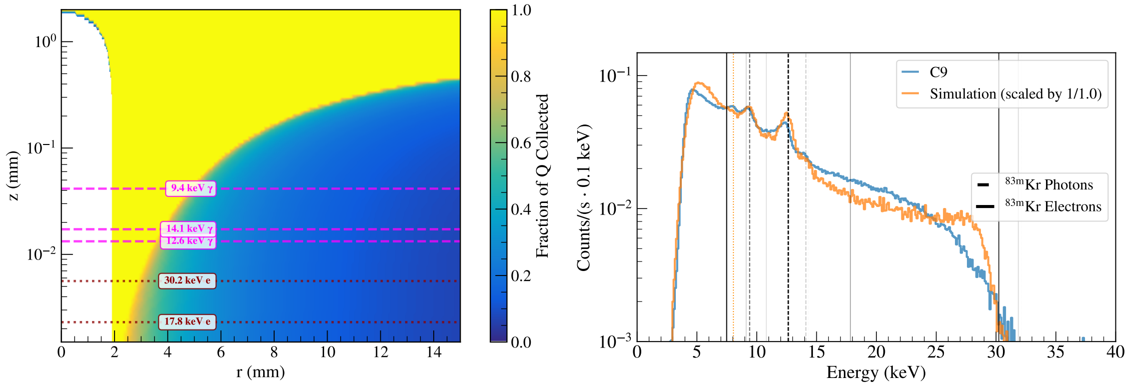

Figure 5.24: Elephant ear (*left*) and final simulation spectrum (*right*) with an 20% decrease in impurity profile. There is no significant difference in the spectrum aside from a slight sharpening of the electron continuum near 30 keV.

Size of $p+$ ***Point Contact***

The $p+$ point contact is made through a boron implantation using a particle accelerator. It is not unreasonable to think that there are portions of the point contact, particularly the interface between the point contact and passivated surface, that are not fully implanted with boron. This is also consistent with our CV curve measurement from Section 5.2.1 giving agreement between data and simulation up to some scaling factor. We can try to study this by leaving the physical point contact at its normal size but shrinking the region that the siggen simulation views as point contact and expanding the passivated region. The resulting elephant ears and spectra for two different point contact sizes are shown in Figures 5.25 and 5.26.

These plots are very interesting because, like the plots shown in this section of the thesis, they suggest the region between the point contact and energy-degraded region is responsible for most of the events in our spectrum. A smaller $p+$ point contact makes this region partially dead, but photons can still enter the detector through the top of the point contact. In order to completely eliminate these photon lines, we need some other source of deadness in the detector. We also consider a slightly smaller $p+$ contact here despite our CV curve measurement suggesting a significantly smaller contact. It would be surprising if the $p+$ point contact was significantly smaller and thus

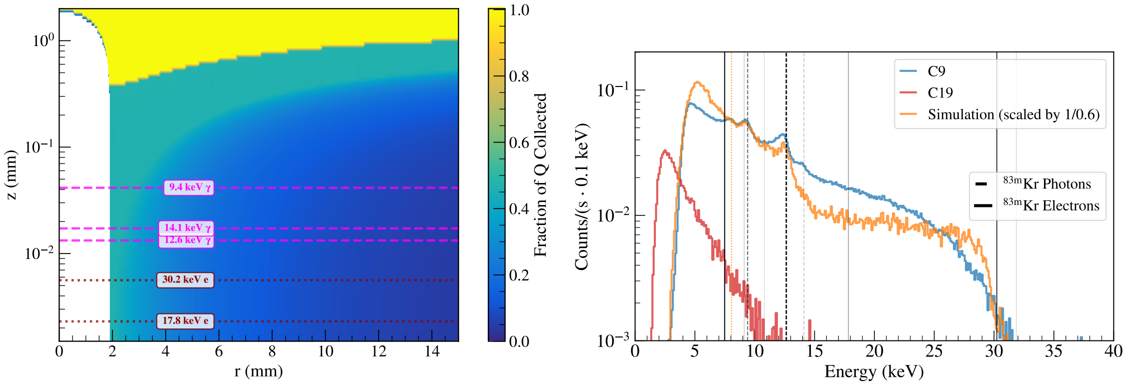

Figure 5.25: Elephant ear (*left*) and final simulation spectrum (*right*) with an 20% decrease in $p+$ point contact size. There is a clear difference in the elephant ear, with the simulated spectrum exhibiting a sharp "shelf" feature at higher energies which begins to wash out the photon peaks in the normalization. Also plotted is the C19 dry spectrum which is not as far off in shape as usual but the normalization is off.

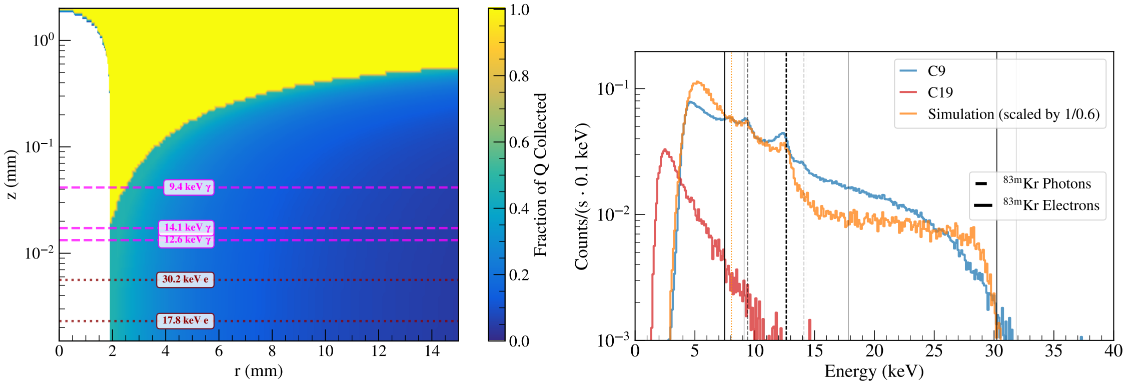

Figure 5.26: Elephant ear (*left*) and final simulation spectrum (*right*) with an 1% decrease in $p+$ point contact size. This spectrum looks very similar to the one in Figure 5.25 but the elephant ear is noticeably different.

we use the more physically intuitive values in Figures 5.25 and 5.26.

5.4 Discussion

Our surface charge model gives qualitative agreement with our wet detector physics data. This is a very exciting result that serves as strong evidence of the existence of these energy-degrading regions in PPC detectors. The photon peaks are well-recreated as is the electron degradation beginning near 30 keV. Minor tweaks to the simulation could likely provide an even better fit to data. That being said, a full likelihood-based fit or a machine learning algorithm is not expected to yield a substantial improvement since this match is only qualitative—a fit would likely fail to converge and/or could give misleading results, especially for the dead layer parameters.

There are a number of reasons why matching simulation to data for each spectral shape and each different detector behavior is difficult and I will address some of these difficulties in this section.

For one, there are a ton of parameters to tune in these simulations that are somewhat degenerate with each other and are not known to the precision that is needed to confidently pin these values and free up parameter space for other values. Values like the $p+$ and PS DLs are fairly well known generally, but are not known for our detector. The lack of an impurity profile is a major source of uncertainty in these simulations. The CV curve measurement is only an approximating of the shape of this curve and thus could be different from our simulation values. More complicated models, like ones with radial dependence of the impurity, can also have a significant impact.

Using a diffuse gaseous source with a constantly decaying parent also hurts our ability to say something confidently about different campaign's krypton rates. We can make a correction based off the half-life of the ^{83}Rb decay, but that still does not take into account the size of the energy-degraded region, where the krypton gas is in the cryostat when it decays, whether it sticks to cold surfaces in the cryostat, and how much gas we actually produce and what fraction of that gas has decay products depositing energy. Using a collimated source with a long half-life solves most of these issues. We plan to use an x-ray fluorescence source [133] (XRF) to study x-rays of different energies impacting the passivated surface of OPPI. This will serve as a powerful companion piece to the KrSTC research and will hopefully illuminate some of the loose ends of this thesis.

We were not able to recreate with simulation the dry detector behavior we saw in the KrSTC data by varying our considered simulation and post-processing parameters. We expect this dry detector behavior to mirror that of the Majorana Demonstrator low energy spectrum question with degraded photon lines. It is still not understood why some alpha particles with smaller penetration depths would deposit a significant fraction of their energy while photons that penetrate deeper into the detector would get "lost." XRF data may help to untangle this phenomenon with a larger range of photon energies.

Of particular interest in the simulation work is this "alley" between the $p+$ point contact and the passivated surface. This alley is active in Figure 5.12 because we cannot put enough surface charge onto the detector to prevent the holes generated in this region from reaching the nearby point contact. In contrast, if we shrink the point contact like in Figure 5.26, we can start to remove activeness in this region. This simulation suggests an ability to recreate different wet detector behaviors by changing the point contact size as well as changing a number of the other simulation parameters. We certainly do not expect the size of the $p+$ point contact to change over time, so once a better model of the implantation is found a larger range of potential simulated spectra is unlocked. However, this $p+$ implantation question still cannot fully explain the dry detector behavior. Unless particles are completely blocked by the boron-implanted point contact, there will be events sneaking into the active region of the detector through the point contact. This serves as the biggest unresolved question from this work.

There are a number of other factors that affect this work that we could not discuss in detail. Something briefly mentioned was charge cloud effects like diffusion and self-repulsion which certainly will have an impact on alpha energy depositions, although they seem more irrelevant for this study. One can imagine, like the DCR effect in alphas, that there is some slower surface charge release for these low energy krypton events, although this is incredibly difficult to find and study due to the significant noise on low energy waveforms.

Other approximations made that could have an impact is the grid size from the siggen simulation, (0.02×0.02) mm^2. Interpolations at length scales below this grid size (which is relevant for some of these decay products) could introduce issues in calculating the elephant ears due to slightly incorrect drift paths. Additionally, the detector was modeled as having a "sharp" 45 degree $n+$ bevel next to the passivated surface, when in reality this surface is smooth. There are clear oddities in electric field behavior near these sharp corners and smoothing these regions out in the simulation can change the electrodynamics of the system.

Chapter 6

Conclusions

This study focused on detector characterization of low energy photons and electrons on the passivated surface of a PPC HPGe detector. We saw two distinct spectra from our krypton source, suggesting that conditions inside the cryostat and near the detector can affect the energy collection of these decay products. One of those spectra, from the "dry" detector campaigns, mimics what we see in the MAJORANA DEMONSTRATOR low energy analysis, with a lack of low energy photon and electron peaks visible in the spectrum. This suggests a larger dead layer than expected with some unknown mechanism that blocks radiation from entering in the point contact of the detector, according to our models. The other spectra we saw, from the "wet" detector campaigns, shows clear photon peaks and some less significantly-energy degraded electrons. These spectral shapes were able to be partially recreated in simulations by applying a negative surface charge on the passivated surface of the detector. This generated a dead layer in the detector that was optimized for one of our campaigns of data, and there is evidence that wet detector spectra with different spectral shapes can also potentially be recreated.

There are still unanswered questions left after this study, mostly relating to this dry detector behavior. Our model cannot recreate this spectrum but there are plans to study this effect further with the XRF teststand at UW. The simulation component of this study can also be expanded quite a bit as there were a number of assumptions and limitations that can be properly accounted for in the future.

What was this all for? Germanium detectors are often used to look for low energy signals [134] [135] [91] so understanding these low energy signals is generally useful. In the case of LEGEND, LEGEND-1000 can be sensitive to supernova neutrinos and such a detection would be very useful for the community in the case that we see a supernova in the near future. These low energy regions can be contaminated with energy-degraded photons and electrons, as we see in this study, and understanding and modeling the dead layers that cause this energy degradation can help clean up this region of the energy spectrum, allowing for easier detection of various low energy phenomena.

Additionally, while LEGEND's primary goal is not to do low energy BSM physics searches, it is still impacted by surface backgrounds. There are some differences, but the physics governing the degradation that KrSTC sees is the same physics that governs the degradation of a 5 MeV alpha down to 2 MeV. This effect is crucial for background reduction and any angle we can take to study and potentially model this energy degradation is important. Studying this effect on a PPC detector which is highly susceptible to these surface charges helps us understand or potentially predict more subtle and unexpected effects that can appear in the IC detectors in LEGEND-1000. Applying this model to IC detectors should be pursued in future work to avoid the risk that this energy degradation, which is not currently included in the L1000 background model, can present. Additionally, applying this model to different cryostat settings like liquid argon and refining them and comparing them to models for alpha degradation can serve as a powerful tool in the fight to reduce backgrounds near $Q_{\beta\beta}$ and in the potential discovery of neutrinoless double beta decay.

Bibliography

[1] J. J. Thomson. Xl. cathode rays. *The London, Edinburgh, and Dublin Philosophical Magazine and Journal of Science*, 44(269):293–316, 1897. doi:10.1080/14786449708621070.

[2] E. Rutherford. Lxxix. the scattering of α and β particles by matter and the structure of the atom. *The London, Edinburgh, and Dublin Philosophical Magazine and Journal of Science*, 21(125):669–688, 1911. doi:10.1080/14786440508637080.

[3] E. Rutherford. Viii. uranium radiation and the electrical conduction produced by it. *The London, Edinburgh, and Dublin Philosophical Magazine and Journal of Science*, 47(284):109–163, 1899. doi:10.1080/14786449908621245.

[4] Henri Becquerel. Sur les radiations invisibles émises par les corps phosphorescents. *Comptes Rendus Hebdomadaires des Séances de l'Académie des Sciences*, 122:501–503, 1896.

[5] P. Curie and M. Curie. Sur une nouvelle substance radioactive, contenue dans la pechblende. *Comptes Rendus Hebdomadaires des Séances de l'Académie des Sciences*, 127:175–178, 1898.

[6] P. Villard. Sur le rayonnement du radium. *Comptes Rendus Hebdomadaires des Séances de l'Académie des Sciences*, 130:1010–1012, 1900.

[7] J. Chadwick. Intensitätsverteilung im magnetischen spektrum der β-strahlen von radium b + c. *Verhandlungen der deutschen physikalischen Gesellschaft*, 16:383–391, 1914.

[8] Wolfgang Pauli. Dear radioactive ladies and gentlemen. Letter to participants of the Gauverein meeting in Tübingen, December 4 1930. Proposing the existence of the neutrino.

[9] E. Fermi. Versuch einer theorie der β-strahlen. i. *Zeitschrift für Physik*, 88(3-4):161–177, 1934. doi:10.1007/BF01351864.

[10] Jr. Cowan, C. L., F. Reines, F. B. Harrison, H. W. Kruse, and A. D. McGuire. Detection of the free neutrino: a confirmation. *Science*, 124(3212):103–104, 1956. doi:10.1126/science.124.3212.103.

[11] C. S. Wu, E. Ambler, R. W. Hayward, D. D. Hoppes, and R. P. Hudson. Experimental test of parity conservation in beta decay. *Physical Review*, 105(4):1413–1415, 1957. doi:10.1103/PhysRev.105.1413.

[12] R. L. Garwin, L. M. Lederman, and M. Weinrich. Observations of the failure of conservation of parity and charge conjugation in meson decays: the magnetic moment of the free muon. *Physical Review*, 105(4):1415–1417, 1957. doi:10.1103/PhysRev.105.1415.

[13] M. Goldhaber, L. Grodzins, and A. W. Sunyar. Helicity of neutrinos. *Physical Review*, 109 (3):1015–1017, 1958. doi:10.1103/PhysRev.109.1015.

[14] J. C. Palathingal. Helicity of antineutrinos emitted by nuclei. *Physical Review Letters*, 24 (10):524–526, 1970. doi:10.1103/PhysRevLett.24.524.

[15] E. C. G. Sudarshan and R. E. Marshak. Chirality invariance and the universal fermi interaction. *Physical Review*, 109(5):1860–1862, 1958. doi:10.1103/PhysRev.109.1860.

[16] R. P. Feynman and M. Gell-Mann. Theory of the fermi interaction. *Physical Review*, 109(1): 193–198, 1958. doi:10.1103/PhysRev.109.193.

[17] G. Danby, J.-M. Gaillard, K. Goulianos, L. M. Lederman, N. Mistry, M. Schwartz, and J. Steinberger. Observation of high-energy neutrino reactions and the existence of two kinds of neutrinos. *Physical Review Letters*, 9(1):36–44, 1962. doi:10.1103/PhysRevLett.9.36.

[18] K. Kodama et al. Observation of tau neutrino interactions. *Physics Letters B*, 504(3):218–224, 2001. doi:10.1016/S0370-2693(01)00307-0.

[19] R. Davis, D. S. Harmer, and K. C. Hoffman. Search for neutrinos from the sun. *Physical Review Letters*, 20(21):1205–1209, 1968. doi:10.1103/PhysRevLett.20.1205.

[20] B. T. Cleveland, T. Daily, Jr. Davis, R., J. R. Distel, K. Lande, C. K. Lee, P. S. Wildenhain, and J. Ullman. Measurement of the solar electron neutrino flux with the homestake chlorine detector. *Astrophysical Journal*, 496(1):505–526, 1998. doi:10.1086/305343.

[21] B. Pontecorvo. Mesonium and anti-mesonium. *Zhurnal Eksperimental'noi i Teoreticheskoi Fiziki*, 33:549, 1957. English translation: Sov. Phys. JETP 6, 429 (1958).

[22] B. Pontecorvo. Inverse beta processes and nonconservation of lepton charge. *Zhurnal Eksperimental'noi i Teoreticheskoi Fiziki*, 34:247, 1958. English translation: Sov. Phys. JETP 7, 172 (1958).

[23] Z. Maki, M. Nakagawa, and S. Sakata. Remarks on the unified model of elementary particles. *Progress of Theoretical Physics*, 28(5):870–880, 1962. doi:10.1143/PTP.28.870.

[24] K. Hirata et al. Observation of a neutrino burst from the supernova sn1987a. *Physical Review Letters*, 58(14):1490–1493, 1987. doi:10.1103/PhysRevLett.58.1490.

[25] K. S. Hirata et al. Observation in the kamiokande-ii detector of the neutrino burst from supernova sn1987a. *Physical Review D*, 38(2):448–458, 1988. doi:10.1103/PhysRevD.38.448.

[26] R. M. Bionta et al. Observation of a neutrino burst in coincidence with supernova 1987a in the large magellanic cloud. *Physical Review Letters*, 58(14):1494–1496, 1987. doi:10.1103/PhysRevLett.58.1494.

[27] Y. Fukuda et al. Evidence for oscillation of atmospheric neutrinos. *Physical Review Letters*, 81(8):1562–1567, 1998. doi:10.1103/PhysRevLett.81.1562.

[28] Q. R. Ahmad et al. Measurement of the rate of $\nu_e + d \rightarrow p + p + e^-$ interactions produced by ^{8}b solar neutrinos at the sudbury neutrino observatory. *Physical Review Letters*, 87(7): 071301, 2001. doi:10.1103/PhysRevLett.87.071301.

[29] Q. R. Ahmad et al. Direct evidence for neutrino flavor transformation from neutral-current interactions in the sudbury neutrino observatory. *Physical Review Letters*, 89(1):011301, 2002. doi:10.1103/PhysRevLett.89.011301.

[30] K. Eguchi et al. First results from kamland: evidence for reactor antineutrino disappearance. *Physical Review Letters*, 90(2):021802, 2003. doi:10.1103/PhysRevLett.90.021802.

[31] T. Araki et al. Measurement of neutrino oscillation with kamland: evidence of spectral distortion. *Physical Review Letters*, 94(8):081801, 2005. doi:10.1103/PhysRevLett.94.081801.

[32] S. Abe et al. Precision measurement of neutrino oscillation parameters with kamland. *Physical Review Letters*, 100(22):221803, 2008. doi:10.1103/PhysRevLett.100.221803.

[33] S. Navas et al. Review of particle physics. *Physical Review D*, 110(3):030001, 2024. doi:10.1103/PhysRevD.110.030001. and 2025 update.

[34] L. Stanco. The next challenge for neutrinos: the mass ordering. *EPJ Web of Conferences*, 164:01031, 2017. doi:10.1051/epjconf/201716401031.

[35] R. L. Workman et al. Review of Particle Physics. *Prog. Theor. Exp. Phys.*, 2022:083C01, 2022. doi:10.1093/ptep/ptac097.

[36] M. Aker et al. Direct neutrino-mass measurement based on 259 days of katrin data. *Science*, 388(6743):180–185, 2025. doi:10.1126/science.adq9592.

[37] T. Yanagida. Horizontal gauge symmetry and masses of neutrinos. In O. Sawada and A. Sugamoto, editors, *Proceedings of the Workshop on the Unified Theory and the Baryon Number in the Universe*, page 95, Tsukuba, Japan, 1979. KEK. Unpublished.

[38] T. Yanagida. Horizontal symmetry and masses of neutrinos. *Progress of Theoretical Physics*, 64(3):1103, 1980. doi:10.1143/PTP.64.1103.

[39] M. Gell-Mann, P. Ramond, and R. Slansky. Complex spinors and unified theories. In P. van Nieuwenhuizen and D. Z. Freedman, editors, *Supergravity*, pages 315–321, Amsterdam, 1979. North-Holland. Presented at Stony Brook Supergravity Workshop, 1979.

[40] R. N. Mohapatra and G. Senjanović. Neutrino mass and spontaneous parity nonconservation. *Physical Review Letters*, 44(14):912–915, 1980. doi:10.1103/PhysRevLett.44.912.

[41] M. Fukugita and T. Yanagida. *Physics of neutrinos and applications to astrophysics*. Theoretical and Mathematical Physics. Springer-Verlag, Berlin, Germany, 2003. ISBN 978-3-662-05119-1, 978-3-540-43800-7, 978-3-642-07851-4. doi:10.1007/978-3-662-05119-1.

[42] A. D. Sakharov. Violation of CP invariance, C asymmetry, and baryon asymmetry of the universe. *JETP Letters*, 5:24–27, 1967. Translation of Pis'ma Zh. Eksp. Teor. Fiz. 5, 32-35 (1967).

[43] M. Fukugita and T. Yanagida. Baryogenesis without grand unification. *Physics Letters B*, 174(1):45–47, 1986. doi:10.1016/0370-2693(86)91126-3.

[44] N. Aghanim et al. Planck 2018 results. VI. Cosmological parameters. *Astronomy & Astrophysics*, 641:A6, 2020. doi:10.1051/0004-6361/201833910.

[45] R. J. Cooke, M. Pettini, and C. C. Steidel. One percent determination of the primordial deuterium abundance. *Astrophysical Journal*, 855:102, 2018. doi:10.3847/1538-4357/aaab53.

[46] P. A. Zyla et al. Review of particle physics. *Progress of Theoretical and Experimental Physics*, 2020(8):083C01, 2020. doi:10.1093/ptep/ptaa104.

[47] J. Kotila and F. Iachello. Phase-space factors for double-β decay. *Physical Review C*, 85(3): 034316, 2012. doi:10.1103/PhysRevC.85.034316.

[48] V. Cirigliano, W. Dekens, M. Graesser, and E. Mereghetti. Shell model study of using an effective field theory for disentangling several contributions to neutrinoless double-β decay. *Physical Review C*, 98(3):035502, 2018. doi:10.1103/PhysRevC.98.035502.

[49] M. Agostini, G. Benato, J. A. Detwiler, J. Menéndez, and F. Vissani. Toward the discovery of matter creation with neutrinoless $\beta\beta$ decay. *Reviews of Modern Physics*, 95(2):025002, 2023. doi:10.1103/RevModPhys.95.025002.

[50] A. Belley, J. M. Yao, B. Bally, J. Pitcher, J. Engel, H. Hergert, J. D. Holt, T. Miyagi, T. R. Rodríguez, A. M. Romero, S. R. Stroberg, and X. Zhang. Ab initio uncertainty quantification of neutrinoless double-beta decay in ^{76}ge. *Physical Review Letters*, 132(18):182502, 2024. doi:10.1103/PhysRevLett.132.182502.

[51] Glen Cowan, Kyle Cranmer, Eilam Gross, and Ofer Vitells. Asymptotic formulae for likelihood-based tests of new physics. *European Physical Journal C*, 71:1554, 2011. doi:10.1140/epjc/s10052-011-1554-0.

[52] H. Acharya et al. First results on the search for lepton number violating neutrinoless double-β decay with the legend-200 experiment. *Physical Review Letters*, 136(2):022701, 2026. doi:10.1103/25tk-nctn.

[53] S. Abe et al. Search for majorana neutrinos with the complete kamland-zen dataset. *Physical Review Letters*, 135(26):262701, 2025. doi:10.1103/jkf6-48j8.

[54] D. Q. Adams et al. Improved limit on neutrinoless double-beta decay in ^{130}te with cuore. *Physical Review Letters*, 124(12):122501, 2020. doi:10.1103/PhysRevLett.124.122501.

[55] O. Azzolini et al. Final result on the neutrinoless double beta decay of ^{82}se with cupid-0. *Physical Review Letters*, 129(11):111801, 2022. doi:10.1103/PhysRevLett.129.111801.

[56] A. Agrawal et al. Improved limit on neutrinoless double beta decay of ^{100}Mo from amore-i. *Phys. Rev. Lett.*, 134:082501, Feb 2025. doi:10.1103/PhysRevLett.134.082501. URL `https://link.aps.org/doi/10.1103/PhysRevLett.134.082501`.

[57] N. Abgrall et al. Legend-1000 preconceptual design report. *arXiv preprint*, 2021.

[58] M. Agostini et al. Final results of gerda on the two-neutrino double-β decay half-life of ^{76}ge. *Physical Review Letters*, 131(14):142501, 2023. doi:10.1103/PhysRevLett.131.142501.

[59] I. J. Arnquist et al. Final result of the majorana demonstrator's search for neutrinoless double-β decay in ^{76}ge. *Physical Review Letters*, 130(6):062501, 2023. doi:10.1103/PhysRevLett.130.062501.

[60] Glenn F. Knoll. *Radiation Detection and Measurement.* John Wiley & Sons, Hoboken, NJ, 3rd edition, 2000. ISBN 978-0-470-13148-0.

[61] S. Richard, F. Aniel, and G. Fishman. Energy-band structure of ge, si, and gaas: A thirty-band $k \cdot p$ method. *Physical Review B*, 70(23):235204, 2004. doi:10.1103/PhysRevB.70.235204. Erratum: Phys. Rev. B 71, 169901 (2005).

[62] W. Shockley. Currents to conductors induced by a moving point charge. *Journal of Applied Physics*, 9(10):635–636, 1938. doi:10.1063/1.1710367.

[63] S. Ramo. Currents induced by electron motion. *Proceedings of the IRE*, 27(9):584–585, 1939. doi:10.1109/JRPROC.1939.228757.

[64] David Radford. icpc_siggen, 2024. URL `https://github.com/radforddc/icpc_siggen`.

[65] M. A. Omar and L. Reggiani. Drift velocity and diffusivity of hot carriers in germanium: Model calculations. *Solid-State Electronics*, 30(12):1351–1354, 1987. doi:10.1016/0038-1101(87)90063-3.

[66] Christian Brendel. *Topologically Protected Transport of Phonons at the Nanoscale*. Phd thesis, 01 2019.

[67] Majorana Collaboration et al. The Majorana Demonstrator readout electronics system. *Journal of Instrumentation*, 17:T05003, 05 2022. doi:10.1088/1748-0221/17/05/T05003. URL `https://iopscience.iop.org/article/10.1088/1748-0221/17/05/T05003`.

[68] Jun Chen. Nuclear data sheets for a=39. *Nuclear Data Sheets*, 149:1–196, 2018. doi:10.1016/j.nds.2018.03.002.

[69] P. Agnes et al. Results from the first use of low radioactivity argon in a dark matter search. *Physical Review D*, 93(8):081101, 2016. doi:10.1103/PhysRevD.93.081101. Rapid Communication; Erratum: Phys. Rev. D 95, 069901 (2017).

[70] INFN Laboratori Nazionali del Gran Sasso. Annual report 2011. `https://www.lngs.infn.it/images/REIS/Annual_Report/annual_report_2011.pdf`, 2011.

[71] E. W. Hoppe, C. E. Aalseth, O. T. Farmer, T. W. Hossbach, M. Liezers, H. S. Miley, N. R. Overman, and J. H. Reeve. Reduction of radioactive backgrounds in electroformed copper for ultra-sensitive radiation detectors. *Nuclear Instruments and Methods in Physics Research Section A*, 763:21–28, 2014. doi:10.1016/j.nima.2014.06.082.

[72] Micah James Noecker Buuck. *A Radiogenic Background Model for the MAJORANA DEMONSTRATOR*. Phd thesis, University of Washington, 2019. URL `http://hdl.handle.net/1773/44889`. Advisor: Jason A. Detwiler.

[73] Gerard 't Hooft. Predictions for neutrino - electron cross-sections in Weinberg's model of weak interactions. *Phys. Lett. B*, 37:195–196, 1971. doi:10.1016/0370-2693(71)90050-5.

[74] H. Ejiri. Nuclear spin isospin responses for low-energy neutrinos. *Phys. Rep.*, 338:265–351, 2000. doi:10.1016/S0370-1573(00)00044-2.

[75] Christoph Wiesinger, Luciano Pandola, and Stefan Schönert. Virtual depth by active background suppression: Revisiting the cosmic muon induced background of GERDA Phase II. *Eur. Phys. J. C*, 78(7):597, 2018. doi:10.1140/epjc/s10052-018-6079-3.

[76] D. H. Wilkinson. The evaluation of allowed β-decay. *Nucl. Phys. A*, 143:365–372, 1970. doi:10.1016/0375-9474(70)90570-1.

[77] J. H. Thies et al. The (He-3, t) reaction on Ge-76, and the double-beta-decay matrix element. *Phys. Rev. C*, 86:014304, 2012. doi:10.1103/PhysRevC.86.014304.

[78] Eunja Ha and Myung-Ki Cheoun. Gamow-Teller Strengths in ^{76}Ge, ^{82}Se, ^{90}Zr, and ^{92}Zr from the Deformed Quasi-particle RPA (DQRPA), 5 2012.

[79] M. Bhattacharya, C. D. Goodman, and A. García. Weak-interaction strength from charge-exchange reactions versus β decay in the $a = 40$ isoquintet. *Phys. Rev. C*, 80:055501, Nov 2009. doi:10.1103/PhysRevC.80.055501. URL `https://link.aps.org/doi/10.1103/PhysRevC.80.055501`.

[80] Myung-Ki Cheoun, Eunja Ha, and Toshitaka Kajino. High-lying excited states in Gamow Teller strength and their roles in neutrino reactions. *Eur. Phys. J. A*, 48:137, 2012. doi:10.1140/epja/i2012-12137-y.

[81] Steven Gardiner. Simulating low-energy neutrino interactions with MARLEY. *Comput. Phys. Commun.*, 269:108123, 2021. doi:10.1016/j.cpc.2021.108123.

[82] Steven Gardiner. Nuclear de-excitations in low-energy charged-current ν_e scattering on ^{40}Ar. *Phys. Rev. C*, 103(4):044604, 2021. doi:10.1103/PhysRevC.103.044604.

[83] Hiroyasu Ejiri. Double beta decays and neutrino masses. *Journal of the Physical Society of Japan*, 74(8):2101–2127, 2005. doi:10.1143/JPSJ.74.2101. URL `https://doi.org/10.1143/JPSJ.74.2101`.

[84] D. Akimov et al. First Measurement of Coherent Elastic Neutrino-Nucleus Scattering on Argon. *Phys. Rev. Lett.*, 126(1):012002, 2021. doi:10.1103/PhysRevLett.126.012002.

[85] J. D. Lewin and P. F. Smith. Review of mathematics, numerical factors, and corrections for dark matter experiments based on elastic nuclear recoil. *Astropart. Phys.*, 6:87–112, 1996. doi:10.1016/S0927-6505(96)00047-3.

[86] N. Van Dessel, V. Pandey, H. Ray, and N. Jachowicz. Cross sections for coherent elastic and inelastic neutrino-nucleus scattering. *Universe*, 9:207, 2023. doi:10.3390/universe9050207.

[87] A. Bonhomme et al. Direct measurement of the ionization quenching factor of nuclear recoils in germanium in the keV energy range. *Eur. Phys. J. C*, 82(9):815, 2022. doi:10.1140/epjc/s10052-022-10768-1.

[88] P. Agnes et al. Measurement of the liquid argon energy response to nuclear and electronic recoils. *Phys. Rev. D*, 97(11):112005, 2018. doi:10.1103/PhysRevD.97.112005.

[89] Jens Lindhard, V Nielsen, M Scharff, and P V Thomsen. Integral equations governing radiation effects. *Mat. Fys. Medd. Dan. Vid. Selsk*, 33(10):1–42, 1963.

[90] D. M. Mei, Z. B. Yin, L. C. Stonehill, and A. Hime. A Model of Nuclear Recoil Scintillation Efficiency in Noble Liquids. *Astropart. Phys.*, 30:12–17, 2008. doi:10.1016/j.astropartphys.2008.06.001.

[91] Z. Y. Zhang et al. Constraints on Sub-GeV Dark Matter–Electron Scattering from the CDEX-10 Experiment. *Phys. Rev. Lett.*, 129(22):221301, 2022. doi:10.1103/PhysRevLett.129.221301.

[92] I. J. Arnquist et al. Exotic Dark Matter Search with the MAJORANA DEMONSTRATOR. *Phys. Rev. Lett.*, 132(4):041001, 2024. doi:10.1103/PhysRevLett.132.041001.

[93] S.L. Watkins, S.R. Elliott, R. Henning, A.F. Leder, R. Massarczyk, and J.C. Waters. L-Note 24-002: Ar-399 Requirement for LEGEND-1000. LEGEND Collaboration Internal Note, 2024. URL `https://legend-exp.atlassian.net/wiki/spaces/LEGEND/pages/918323211/L-Note+24-002`.

[94] Aldo Serenelli. Alive and well: a short review about standard solar models. *Eur. Phys. J. A*, 52(4):78, 2016. doi:10.1140/epja/i2016-16078-1.

[95] S. P. Mikheyev and A. Yu. Smirnov. Resonance Amplification of Oscillations in Matter and Spectroscopy of Solar Neutrinos. *Sov. J. Nucl. Phys.*, 42:913–917, 1985.

[96] L. Wolfenstein. Neutrino Oscillations in Matter. *Phys. Rev. D*, 17:2369–2374, 1978. doi:10.1103/PhysRevD.17.2369.

[97] H. Ejiri and S. R. Elliott. Charged current neutrino cross section for solar neutrinos, and background to $\beta\beta(0\nu)$ experiments. *Phys. Rev. C*, 89(5):055501, 2014. doi:10.1103/PhysRevC.89.055501.

[98] A. Fazliakhmetov, L. Inzhechik, G. Koroteev, Yu Lutostansky, V. Tikhonov, and A. Vyborov. High-lying gamow-teller resonances and neutrino capture cross-section for 76ge. volume 2165, page 020015, 10 2019. doi:10.1063/1.5130976.

[99] K. Hirata et al. Observation of a Neutrino Burst from the Supernova SN 1987a. *Phys. Rev. Lett.*, 58:1490–1493, 1987. doi:10.1103/PhysRevLett.58.1490.

[100] R. M. Bionta et al. Observation of a Neutrino Burst in Coincidence with Supernova SN 1987a in the Large Magellanic Cloud. *Phys. Rev. Lett.*, 58:1494, 1987. doi:10.1103/PhysRevLett.58.1494.

[101] E. N. Alekseev, L. N. Alekseeva, V. I. Volchenko, and I. V. Krivosheina. Possible detection of a neutrino signal on 23 february 1987 at the baksan underground scintillation telescope of the institute of nuclear research. *JETP Lett.*, 45:589–592, 1987.

[102] K. Abe et al. Supernova Model Discrimination with Hyper-Kamiokande. *Astrophys. J.*, 916 (1):15, 2021. doi:10.3847/1538-4357/abf7c4.

[103] Ken'ichiro Nakazato, Kohsuke Sumiyoshi, Hideyuki Suzuki, Tomonori Totani, Hideyuki Umeda, and Shoichi Yamada. Supernova Neutrino Light Curves and Spectra for Various Progenitor Stars: From Core Collapse to Proto-neutron Star Cooling. *Astrophys. J. Suppl.*, 205:2, 2013. doi:10.1088/0067-0049/205/1/2.

[104] Kelly M. Patton, Cecilia Lunardini, Robert J. Farmer, and F. X. Timmes. Neutrinos from beta processes in a presupernova: probing the isotopic evolution of a massive star. *Astrophys. J.*, 851(1):6, 2017. doi:10.3847/1538-4357/aa95c4.

[105] H. Thomas Janka, Tobias Melson, and Alexander Summa. Physics of Core-Collapse Supernovae in Three Dimensions: a Sneak Preview. *Ann. Rev. Nucl. Part. Sci.*, 66:341–375, 2016. doi:10.1146/annurev-nucl-102115-044747.

[106] Alexandru Hostiuc. *Search for Neutrinoless Double Beta Decay Using the Full Majorana Demonstrator Dataset.* Phd thesis, University of Washington, 2023.

[107] F. G. Kondev. Nuclear data sheets for a=203. *Nuclear Data Sheets*, 201:346–607, May 2025. doi:10.1016/j.nds.2025.03.002.

[108] J. Gruszko and on behalf of the Majorana Collaboration. Delayed charge recovery discrimination of passivated surface alpha events in P-type point-contact detectors. *Journal of Physics: Conference Series*, 888:012079, 2017. doi:10.1088/1742-6596/888/1/012079. URL `https://iopscience.iop.org/article/10.1088/1742-6596/888/1/012079`.

[109] M. J. Berger, J. H. Hubbell, S. M. Seltzer, J. Chang, J. S. Coursey, R. Sukumar, D. S. Zucker, and K. Olsen. Xcom: Photon cross sections database. NIST Standard Reference Database 8 (XGAM), 2010. URL `https://www.nist.gov/pml/xcom-photon-cross-sections-database`. Accessed: 2026-02-16.

[110] M. J. Berger, J. S. Coursey, M. A. Zucker, and J. Chang. Estar: Stopping-power and range tables for electrons. NIST Standard Reference Database 124, 2017. URL `https://www.nist.gov/pml/stopping-power-range-tables-electrons-protons-and-helium-ions`. Accessed: 2026-02-16.

[111] M. J. Berger, J. S. Coursey, M. A. Zucker, and J. Chang. Astar: Stopping-power and range tables for helium ions. NIST Standard Reference Database 124, 2017. URL `https://www.nist.gov/pml/stopping-power-range-tables-electrons-protons-and-helium-ions`. Accessed: 2026-02-16.

[112] I. J. Arnquist et al. α-event characterization and rejection in point-contact hpge detectors. *European Physical Journal C*, 82(3):226, 2022. doi:10.1140/epjc/s10052-022-10161-y.

[113] G. Othman, C. Wiseman, T. H. Burritt, J. A. Detwiler, M. P. Held, R. Henning, T. Mathew, D. Peterson, W. Pettus, G. Song, and T. D. Van Wechel. Cage: An internal source scanning cryostat for hpge characterization. *arXiv preprint*, 2026. arXiv:2602.06289 [physics.ins-det].

[114] Grace Song. *The CAGE Scanner: Development of a Novel Surface Event Rejection Technique in High Purity Germanium Detectors*. Phd thesis, University of Washington, 2025. ProQuest ID: 3292885495.

[115] Gulden Othman. *The CAGE Scanner: Investigating Surface Backgrounds in High-Purity Germanium Detectors*. Phd thesis, University of North Carolina at Chapel Hill, 2021. URL `https://cdr.lib.unc.edu/concern/dissertations/d217r000d`.

[116] E. A. McCutchan. Nuclear data sheets for a=83. *Nuclear Data Sheets*, 125:201–394, 2015. doi:10.1016/j.nds.2015.02.002.

[117] S. Enomoto et al. Slowdash. `https://github.com/slowproj/slowdash`, 2024.

[118] M. Howe et al. Orca: Data acquisition and analysis for physics experiments, 2024. URL `https://github.com/unc-enap/Orca`.

[119] Yu. Khazov, A. Rodionov, and F. G. Kondev. Nuclear data sheets for a=133. *Nuclear Data Sheets*, 112:855–1113, 2011. doi:10.1016/j.nds.2011.03.001.

[120] LEGEND Collaboration. pygama: Python package for germanium detector data analysis, January 2026. URL `https://github.com/legend-exp/pygama`.

[121] N. Abgrall et al. Adc nonlinearity correction for the majorana demonstrator. *IEEE Transactions on Nuclear Science*, 68(3):359–367, 2021. doi:10.1109/TNS.2020.3043671.

[122] V. T. Jordanov and G. F. Knoll. Digital synthesis of pulse shapes in real time for high resolution radiation spectroscopy. *Nuclear Instruments and Methods in Physics Research Section A*, 345(2):337–345, 1994. doi:10.1016/0168-9002(94)91011-1.

[123] S. Agostinelli et al. Geant4—a simulation toolkit. *Nuclear Instruments and Methods in Physics Research Section A*, 506(3):250–303, 2003. doi:10.1016/S0168-9002(03)01368-8.

[124] J.A. Detwiler et al. g4simple. `https://github.com/legend-exp/g4simple`, 2024.

[125] D. Vénos, J. Sentkerestiová, O. Dragoun, M. Slezák, M. Ryšavý, and A. Špalek. Properties of ^{83m}kr conversion electrons and their use in the katrin experiment. *Journal of Instrumentation*, 13(2):T02012, February 2018. doi:10.1088/1748-0221/13/02/T02012.

[126] I. Abt, C. Gooch, F. Hagemann, L. Hauertmann, O. Schulz, M. Schuster, and A. J. Zsigmond. Bayesian inference of high-purity germanium detector impurities based on capacitance measurements and machine-learning accelerated capacitance calculations. *European Physical Journal C*, 83:352, 2023. doi:10.1140/epjc/s10052-023-11509-8.

[127] I. Abt, F. Fischer, F. Hagemann, L. Hauertmann, O. Schulz, M. Schuster, and A. J. Zsigmond. Simulation of semiconductor detectors in 3d with solidstatedetectors.jl. *Journal of Instrumentation*, 16(08):P08007, 8 2021. doi:10.1088/1748-0221/16/08/p08007. URL `https://doi.org/10.1088/1748-0221/16/08/p08007`.

[128] Frank Edzards, Lukas Hauertmann, Iris Abt, Chris Gooch, Björn Lehnert, Xiang Liu, Susanne Mertens, David C. Radford, Oliver Schulz, and Michael Willers. Surface characterization of P-type point contact germanium detectors. *Particles*, 4(4):489–511, 2021. doi:10.3390/particles4040036. URL `https://doi.org/10.3390/particles4040036`.

[129] N.Q. Huy, D.Q. Binh, and V.X. An. Study on the increase of inactive germanium layer in a high-purity germanium detector after a long time operation applying MCNP code. *Nuclear Instruments and Methods in Physics Research Section A*, 573(3):384–388, 2007. doi:10.1016/j.nima.2006.12.048.

[130] Mirion Technologies, Inc. *REGe™ Reverse Electrode Coaxial Germanium Detectors*, October

2025. URL `https://assets-mirion.mirion.com/prod-20220822/cms4_mirion/files/pdf/spec-sheets/rege-data-sheet.pdf`. SPC-657-EN-B.

[131] P.N. Luke, C.S. Rossington, and M.F. Wesela. Low energy x-ray response of ge detectors with amorphous ge entrance contacts. *IEEE Transactions on Nuclear Science*, 41(4):1074–1079, 1994. doi:10.1109/23.322861.

[132] C. Jacoboni, C. Canali, G. Ottaviani, and A. Alberigi Quaranta. A review of some charge transport properties of silicon. *Physical Review B*, 24(2):1014–1026, 1981. doi:10.1103/PhysRevB.24.1014.

[133] S. R. Elliott, E.M. Bond, B. Dodson, G. Rusev, R. Massarczyk, S. J. Meijer, M. Stortini, and C. Wiseman. Variable energy X-ray fluorescence source. *Journal of Instrumentation*, 18(01): P01004, January 2023. doi:10.1088/1748-0221/18/01/P01004.

[134] N. Ackermann, H. Bonet, A. Bonhomme, C. Buck, K. Fülber, J. Hakenmüller, J. Hempfling, G. Heusser, M. Lindner, W. Maneschg, K. Ni, M. Rank, T. Rink, E. Sánchez García, I. Stalder, H. Strecker, R. Wink, J. Woenckhaus, et al. Direct observation of coherent elastic antineutrino–nucleus scattering. *Nature*, 643:1229–1233, July 2025. doi:10.1038/s41586-025-09322-2.

[135] S. Adamski et al. Evidence of coherent elastic neutrino-nucleus scattering with COHERENT's germanium array. *Physical Review Letters*, 134:231801, June 2025. doi:10.1103/PhysRevLett.134.231801.